

AD-A202 185

ESG1798

2

AFATL-TR-88-94

DTIC FILE COPY

An Exploratory Study of Ram Accelerator Principles

A Hertzberg
A P Bruckner
D W Bogdanoff

UNIVERSITY OF WASHINGTON
SEATTLE, WASHINGTON 98195

OCTOBER 1988

FINAL REPORT FOR PERIOD AUGUST 1984 - JANUARY 1988

APPROVED FOR PUBLIC RELEASE; DISTRIBUTION UNLIMITED

DTIC
ELECTE
NOV 10 1988

AIR FORCE ARMAMENT LABORATORY
Air Force Systems Command ■ United States Air Force ■ Eglin Air Force Base, Florida

88 11 10 011

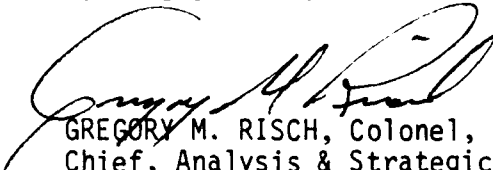
NOTICE

When Government drawings, specifications, or other data are used for any purpose other than in connection with a definitely related Government procurement operation, the United States Government thereby incurs no responsibility nor any obligation whatsoever; and the fact that the Government may have formulated, furnished, or in any way supplied the said drawings, specifications, or other data, is not to be regarded by implication or otherwise as in any manner licensing the holder or any other person or corporation, or conveying any rights or permission to manufacture, use, or sell any patented invention that may in any way be related thereto.

This report has been reviewed by the AFATL STINFO Officer, and it is releasable to the National Technical Information Service (NTIS). At NTIS, it will be available to the general public, including foreign nations.

This technical report has been reviewed and is approved for publication.

FOR THE COMMANDER



GREGORY M. RISCH, Colonel, USAF
Chief, Analysis & Strategic Defense Division

If your address has changed, if you wish to be removed from our mailing list, or if the addressee is no longer employed by your organization, please notify AFATL/SAH , Eglin AFB FL 32542-5434.

Copies of this report should not be returned unless return is required by security considerations, contractual obligations, or notice on a specific document.

UNCLASSIFIED

SECURITY CLASSIFICATION OF THIS PAGE

REPORT DOCUMENTATION PAGE				Form Approved OMB No. 0704-0188	
1a. REPORT SECURITY CLASSIFICATION Unclassified		1b. RESTRICTIVE MARKINGS			
2a. SECURITY CLASSIFICATION AUTHORITY		3. DISTRIBUTION / AVAILABILITY OF REPORT Approved for public release; distribution is unlimited.			
2b. DECLASSIFICATION / DOWNGRADING SCHEDULE		4. PERFORMING ORGANIZATION REPORT NUMBER(S) AFATL-TR-88-94			
6a. NAME OF PERFORMING ORGANIZATION Aerospace and Energetics Research Program		6b. OFFICE SYMBOL (if applicable)	7a. NAME OF MONITORING ORGANIZATION Electromagnetic Launcher Technology Branch Analysis & Strategic Defense Division		
6c. ADDRESS (City, State, and ZIP Code) University of Washington, FL-10 Seattle, WA 98195		7b. ADDRESS (City, State, and ZIP Code) Air Force Armament Laboratory Eglin Air Force Base, FL 32542-5434			
8a. NAME OF FUNDING / SPONSORING ORGANIZATION Analysis & Strategic Defense Division		8b. OFFICE SYMBOL (if applicable) AFATL/SAH	9. PROCUREMENT INSTRUMENT IDENTIFICATION NUMBER F08635-84-K-0143		
8c. ADDRESS (City, State, and ZIP Code) Electromagnetic Launcher Technology Branch Air Force Armament Laboratory Eglin Air Force Base, FL 32542-5434		10. SOURCE OF FUNDING NUMBERS			
		PROGRAM ELEMENT NO. 61601F	PROJECT NO. 2502	TASK NO. 12	WORK UNIT ACCESSION NO. 25
11. TITLE (Include Security Classification) An Exploratory Study of Ram Accelerator Principles					
12. PERSONAL AUTHOR(S) A. Hertzberg, A.P. Bruckner, D.W. Bogdanoff					
13a. TYPE OF REPORT Final		13b. TIME COVERED FROM Aug 84 to Jan 88	14. DATE OF REPORT (Year, Month, Day) October 1988		15. PAGE COUNT 128
16. SUPPLEMENTARY NOTATION Availability of this report is specified on verso of front cover.					
17. COSATI CODES			18. SUBJECT TERMS (Continue on reverse if necessary and identify by block number)		
FIELD	GROUP	SUB-GROUP	Ram Accelerators, Propulsion Techniques, Subsonic Combustion, Chemical Propulsion		
19. ABSTRACT (Continue on reverse if necessary and identify by block number)					
A new method for accelerating projectiles from velocities of 0.7 km/sec up to 12 km/sec using chemical energy is described. The concept, called the "ram accelerator," is based on gasdynamic principles similar to those of a supersonic airbreathing ramjet but operates in a different manner. The projectile resembles the center body of a ramjet and travels through a tube filled with a premixed gaseous fuel and oxidizer mixture. The tube acts as the outer cowling of the ramjet and the combustion process travels with the projectile. By tailoring the propellant mixture along the tube, a nearly constant acceleration can be achieved. In principle, the ram accelerator is scalable for projectile masses ranging from grams to thousands of kilograms and is capable of ballistic efficiencies as high as 30 percent. Two theoretical models developed for analytical studies are described, one involving a simple quasi-steady, one-dimensional approach, and the other a computational fluid dynamics approach. The experimental facility developed at the University of Washington to (over)					
20. DISTRIBUTION / AVAILABILITY OF ABSTRACT <input type="checkbox"/> UNCLASSIFIED/UNLIMITED <input checked="" type="checkbox"/> SAME AS RPT. <input type="checkbox"/> DTIC USERS			21. ABSTRACT SECURITY CLASSIFICATION Unclassified		
22a. NAME OF RESPONSIBLE INDIVIDUAL Richard H. Byers, Captain, USAF		22b. TELEPHONE (Include Area Code) (904) 883-0360		22c. OFFICE SYMBOL AFATL/SAH	

DD Form 1473, JUN 86

Previous editions are obsolete.

SECURITY CLASSIFICATION OF THIS PAGE

UNCLASSIFIED

UNCLASSIFIED

19. ABSTRACT (CONCLUDED)

investigate the concept is described and the results of proof-of-concept experiments are presented. The velocity range of 690-2400 m/sec has been explored in a 12.2 m long, 38 mm bore accelerator tube. Using methane, oxygen, and various diluents, accelerations up to 30,000 g's have been achieved with 50 gram projectiles and gas fill pressures of 25 atmospheres. Proof-of-concept has been demonstrated and agreement between theory and experiment has been found to be very good.

UNCLASSIFIED

PREFACE

This program was conducted by the Aerospace and Energetics Research Program, University of Washington, Seattle, Washington 98195, under Contract F08635-84-K-0143 with the Air Force Armament Laboratory, Eglin Air Force Base, Florida 32542-5434. Captain Richard H. Byers (AFATL/SAH) managed the program for the Armament Laboratory. The program was conducted during the period from August 1984 to January 1988.

ACKNOWLEDGMENTS

The authors are deeply indebted to their students, Carl Knowlen, Alan Kull, Ed Burnham, Kelley Ann Scott, Alfred Alvarez, Dai Murakami, Ivan Stonich, Dean Brackett, Dale Barr, Carl Engelbrecht, Keith McFall and John Zulauf, whose enthusiasm and diligence assured the success of the project. Although it is not possible to acknowledge all of the colleagues with whom they had helpful discussions, the authors are particularly indebted to Ed Kepler of the United Technologies Research Center, East Hartford, CT, for his invaluable discussions on the technology of ramjets; to Roger Strehlow of the University of Illinois, Urbana, IL, for his useful comments on the combustion and detonation aspects of this work; and, to Hal Swift, President of Physics Applications, Inc., Dayton, OH, for his useful suggestions about the mechanical and gasdynamic operating procedures employed. The authors are grateful also to the Kistler Instrument Corporation for its generous gift of pressure transducers and related instrumentation.



Accession For	
NTIS GRA&I	<input checked="" type="checkbox"/>
DTIC TAB	<input type="checkbox"/>
Unannounced	<input type="checkbox"/>
Justification	
By _____	
Distribution/	
Date/	
Author/	
Title/	
A-1	

TABLE OF CONTENTS

Section	Title	Page
I	INTRODUCTION.	1
II	RAM ACCELERATOR DRIVE MODES	6
III	ANALYSIS OF THERMALLY CHOKED SUBSONIC COMBUSTION MODE	12
	1. SIMPLIFIED 1-D ANALYSIS	12
	2. MORE DETAILED 1-D ANALYSIS.	17
IV	EXPERIMENTAL RAM ACCELERATOR FACILITY	20
	1. LIGHT GAS GUN	20
	2. RAM ACCELERATOR SECTION	22
	3. FINAL DUMP TANK	24
	4. DECELERATOR	24
	5. GAS HANDLING SYSTEM	24
	6. DATA ACQUISITION SYSTEM	25
	7. PROJECTILE CONFIGURATION.	25
	8. IGNITION SYSTEM	26
V	RESULTS OF EXPERIMENTS WITH THERMALLY CHOKED MODE	27
	1. OPERATING CONDITIONS.	27
	2. PRESSURE AND EM SIGNATURES.	27
	3. VELOCITY PROFILES	31
	4. BALLISTIC EFFICIENCY.	39
	5. TRANSITION BETWEEN MIXTURES	43
	6. THRUST PRESSURE RATIO	45
	7. VELOCITY LIMITING PHENOMENA	45
VI	DETONATION DRIVEN MODES	50
	1. SUMMARY OF 1-D DETONATION DRIVEN MODE THEORY.	50
	2. OVERDRIVEN DETONATION MODE.	52
	3. TYPE I OBLIQUE DETONATION MODE.	53
	4. TYPE II OBLIQUE DETONATION MODE	53
	5. RESULTS AND DISCUSSION OF 1-D ANALYSIS.	54
VII	CFD MODELING OF OBLIQUE DETONATION MODES.	60
	1. TYPE I OBLIQUE DETONATION MODE.	61
	2. TYPE II OBLIQUE DETONATION MODE	65
	3. STRATIFIED CHARGE MODE.	73
VIII	CONCLUSIONS	79

Section	Title	Page
REFERENCES.		80
APPENDIX		
A	ADIABATIC FLAME TEMPERATURE CALCULATIONS FOR CH ₄ -H ₂ -O ₂ MIXTURES.	83
B	DETAILED 1-D ANALYSIS OF SUBSONIC COMBUSTION AND OVERDRIVEN RAM ACCELERATOR MODES.	91
C	CFD NUMERICAL PROCEDURES FOR OBLIQUE DETONATION MODES	107
BIBLIOGRAPHY		119

LIST OF FIGURES

Figure	Title	Page
1	Schematic of Conventional Supersonic Airbreathing Ramjet. . .	3
2	Schematic of Subsonic Combustion Ram Accelerator Modes. . .	4
3	Schematic of Overdriven Detonation Ram Accelerator Mode . . .	8
4	Schematic of Oblique Detonation Ram Accelerator Modes . . .	9
5	Schematic of University of Washington Ram Accelerator Facility.	21
6	Schematic of Ram Accelerator Test Section and Associated Instrumentation	23
7	Experimental Ram Accelerator Projectile	23
8	Electromagnetic (EM) and Pressure Transducer Signals in Ram Accelerator, 1.51 m from Entrance Diaphragm	28
9	Ratio of Peak Cycle Pressure to Tube Fill Pressure as a Function of Projectile Velocity	30
10	Velocity Profiles in 4.88 m Ram Accelerator	32
11	Velocity Profile in 11 m Ram Accelerator Having Two Staged Propellant Mixtures	33
12	Velocity Profile in Three-Stage 11 m Ram Accelerator. . . .	34
13	Velocity Profile in Fourth Stage of Four-Stage 11.9 m Ram Accelerator	35
14	Pressure Signature for a Typical Unstart Condition.	38
15	Ballistic Efficiency as a Function of Velocity for Staged Propellant Mixtures Shown in Figure 12.	40
16	Ballistic Efficiency as a Function of Velocity for Fourth- Stage Propellant Mixture Shown in Figure 13	41
17	Pressure Signatures Before and After Transition from $2.5 \text{ CH}_4 + 2\text{O}_2 + 6\text{N}_2$ to $4.5 \text{ CH}_4 + 2\text{O}_2 + 2\text{He}$	44
18	Thrust Pressure Ratio as a Function of Velocity for CO_2 and N_2 Diluted Mixtures	46

Figure	Title	Page
19	Pressure Signature Showing Typical Shock Wave Fall-Off from Projectile.	48
20	Thrust Pressure Ratio as a Function of Projectile Velocity for Type I Oblique Detonation Mode.	55
21	Thrust Pressure Ratio as a Function of Projectile Velocity for the Three Detonation-Driven Modes Using the Same Propellant Mixtures Shown in Figure 20.	55
22	Ballistic Efficiency as a Function of Projectile Velocity Using the Same Propellant Mixtures and Detonation Driven Modes Shown in Figure 20.	57
23	Theoretical Velocity Profiles for the Three Detonation Driven Modes Operating for the Conditions Shown in Figures 21 and 22	57
24	Oblique Detonation Type I Mode Geometry Used in CFD Studies	62
25	Oblique Detonation Type I Thrust Pressure Ratio Versus Velocity.	64
26	Oblique Detonation Type I Ballistic Efficiency Versus Velocity.	64
27	Pressure Contours Surrounding Oblique Detonation Type I Projectile Moving at 7.0 km/sec in Mixture 1 ($8H_2 + O_2$) . .	66
28	Oblique Detonation Type II Mode Geometry Used in CFD Studies	67
29	Magnified View of Ramp in Type II Oblique Detonation Mode.	67
30	Pressure Contours Surrounding Oblique Detonation Type II Projectile with a 0.04 cm Ramp Height, Moving at 8 km/sec in Mixture 1.	70
31	Type II Oblique Detonation Thrust Pressure Ratio Versus Vehicle Velocity for Projectile Lengths and Gas Mixtures Indicated	72
32	Type II Oblique Detonation Ballistic Efficiency Versus Projectile Velocity for Projectile Lengths and Gas Mixtures as Indicated in Figure 31	72

Figure	Title	Page
33	Pressure Contours Surrounding a Projectile with a 0.035 cm Ramp Height Moving at 10 km/sec in a Stratified Charge with a H ₂ Core Surrounded by a 2H ₂ + O ₂ Gas Mixture	76
B-1	Schematic of Subsonic Combustion Ram Accelerator Modes. . .	92
B-2	Schematic of Overdriven Detonation Ram Accelerator Mode.	93
C-1	Illustration of Extrapolation, Interpolation and Cell Boundary Value Correction Techniques.	109

LIST OF TABLES

Table	Title	Page
1	Propellant Compositions and Transition Velocities in Four-Stage Ram Accelerator Configuration	36
2	Comparison of 1-D and CFD Models for the Type I Oblique Detonation Mode	58
3	Gas Mixtures Investigated	61
4	Comparison of Types I and II Oblique Detonation Mode Performance	71
5	Performance of Stratified Charge Mode	75
6	Comparison of Types I and II Oblique Detonation and Stratified Charge Modes	78
C-1	Selection of First or Higher Order Extrapolations/Interpolations Depending on β_m	111
C-2	Selection of First or Second Order Godunov Calculations Depending on β_{mg}	114

SECTION I

INTRODUCTION

The barrier to accelerating a projectile to very high velocities by chemical energy is rooted in the limitations of the driver (Reference 1). Once the projectile is accelerated to velocities beyond the initial acoustic velocity of the driver gas, the ballistic efficiency* falls off very rapidly as the driving gas expends most of its energy in accelerating itself. While several methods of achieving high acoustic velocities have been employed, such as precompression of the driver gas (two-stage gun), combustion heating, or electrical heating of a light driver gas, these methods result in relatively low ballistic efficiencies at high velocities and uneven acceleration profiles (Reference 1).

Studies carried out by the authors since mid-1983 have led to a promising new technique, called the "ram accelerator," by which relatively large masses (up to hundreds of kilograms) can, in principle, be efficiently accelerated to velocities up to 12 km/sec by utilizing chemical energy in a new manner. The basic principle involves an energy release process that travels with the projectile; unlike a rocket, however, with this new concept there is no propellant on board the projectile. The ballistic efficiency remains high up to extremely high velocities and the acceleration can be maintained at a nearly constant level. While the gasdynamic principles of the ram accelerator are similar in many respects to those of the conventional airbreathing ramjet, the device is operated in a different manner.

Supersonic ramjets with subsonic combustion operate efficiently in the Mach number range of about 2 to 5 (Reference 2). Consider a conventional ramjet with an outer cowling and an internal body comprising a forward

*Ballistic efficiency is defined here as the ratio of the rate of change of kinetic energy of the projectile to the rate of expenditure of chemical energy. This is an instantaneous efficiency which varies during the acceleration process. The overall ballistic efficiency is the ratio of the total change in kinetic energy of the projectile to the total chemical energy expended.

supersonic diffuser, a combustion section, and a convergent-divergent nozzle (Figure 1). The performance of such a configuration flying through the atmosphere can be readily calculated. The fuel, however, must be carried on board and the engine efficiency is limited by aerodynamic drag and by difficulties in obtaining high efficiency diffusers in the higher Mach number ranges. The thrust is limited by the density of the atmosphere, and the sound speed of the working gas is fixed by the temperature and composition of the atmosphere.

In the ram accelerator concept (Figure 2), the internal body is a projectile fired into a tube and the cowling is now the wall of the tube. This affords the ability to control the pressure, composition, chemical energy density, and speed of sound (and hence Mach number) of the gas entering the ramjet engine. The gaseous propellant, consisting of premixed fuel and oxidizer, such as methane and oxygen or hydrogen and oxygen, fills the tube so that no fuel or oxidizer need be carried by the projectile. Since the fuel and oxidizer are premixed, the difficulties in obtaining rapid and complete mixing which are encountered in conventional subsonic combustion and supersonic combustion ramjets are circumvented.

The concept of flying a ramjet in a tube is not in itself new. For example, Wilbur, et al., have proposed a direct space launch scheme involving electrical heating to accelerate payloads to 14-15 km/sec (References 3 and 4). However, the problems of electrical energy management and release for the required large payloads appear formidable. Slutsky and Tamagno proposed a supersonic combustion ramjet-in-tube concept in 1967 (Reference 5), and recently, A. Glasser suggested a ramjet-in-tube concept in which the projectile carries a solid fuel and the tube is filled with oxidizer (Reference 6). However, neither of these two investigations has appeared in the open literature. Insofar as the authors know, none of these concepts has been explored experimentally.

Five modes of ram accelerator operation, which span the velocity range of 0.7-12 km/sec, have been developed and studied by the authors. These concepts differ from the prior art noted above in that the projectile flies through a premixed fuel-oxidizer mixture and utilizes energy release modes and configurations not heretofore considered. These include two subsonic

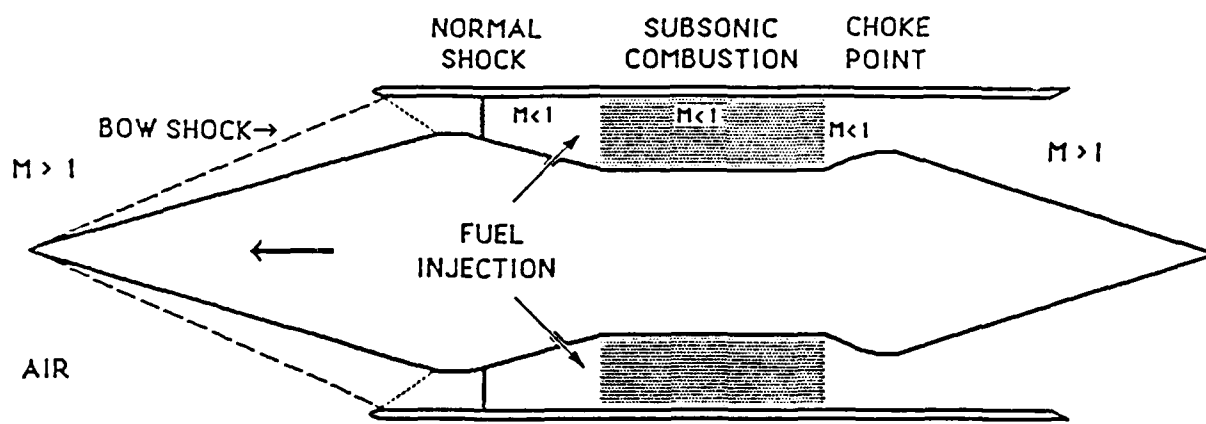
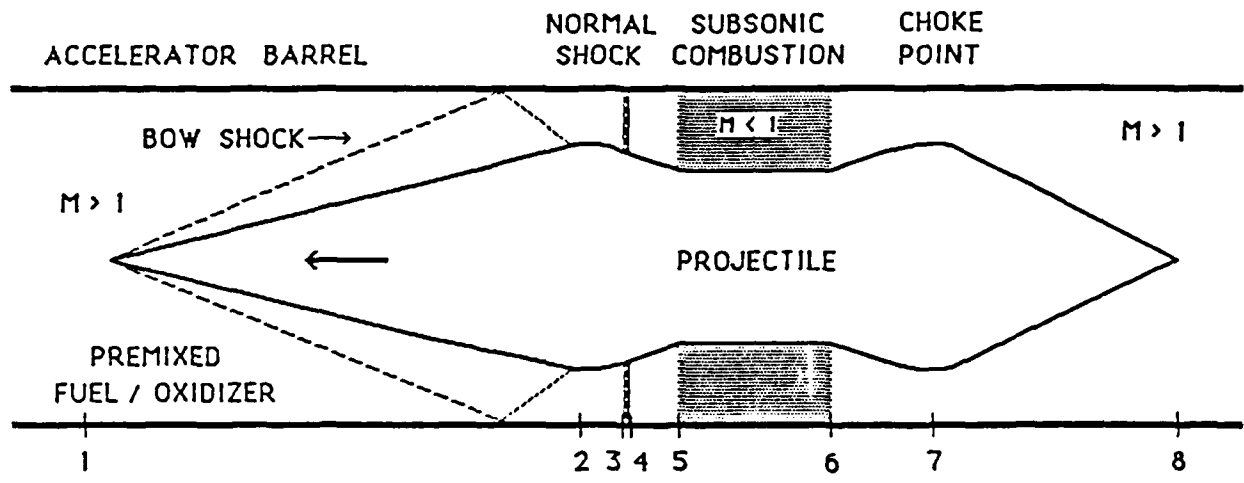
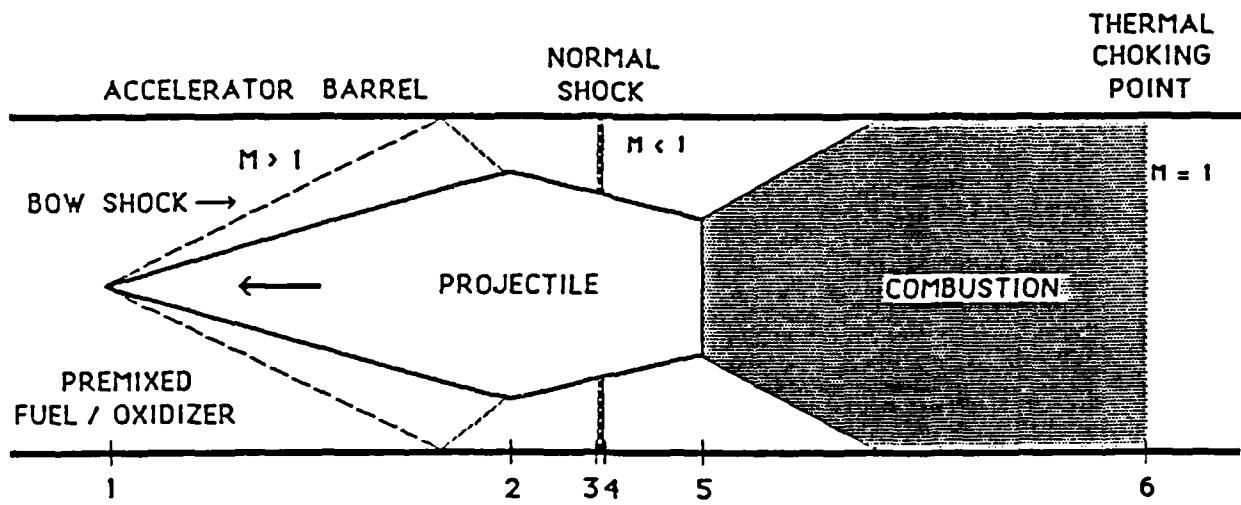


Figure 1. Schematic of a Conventional Supersonic Airbreathing Ramjet.



a) Mechanically Choked Mode



b) Thermally Choked Mode

Figure 2. Schematic of Subsonic Combustion Ram Accelerator Modes.

combustion modes (one of which involves thermally choked combustion), a normal overdriven detonation mode and two oblique detonation modes. The basic principles of all five acceleration modes are summarized in Section II of this report. Section III treats the analytical models used to date in the investigation of the thermally choked mode. Section IV describes the experimental facility constructed for proof-of-concept studies and Section V presents the results of experiments spanning the velocity range 690-2400 m/sec. The theoretical analyses of the detonation-driven modes are described in Sections VI and VII. (No experiments with these modes have yet been performed.) Finally, Section VIII is comprised of conclusions and recommendations for future work. The appendices provide additional detailed information on the analytical procedures.

SECTION II

RAM ACCELERATOR DRIVE MODES

The subsonic combustion ram accelerator drive modes are shown in Figure 2. The projectile is injected into the accelerator tube at approximately 700 m/sec by a conventional powder or gas gun. The gas mixture in the accelerator tube is chosen so that the projectile mach number is initially in the range of 2.5-3. The cone angle of the nose is such that the oblique shock system in the diffuser does not initiate combustion. A normal shock is located downstream of the projectile throat; this shock is also not strong enough to initiate combustion. In the geometry of Figure 2a the combustion zone is at the projectile waist and is fully subsonic. A convergent-divergent nozzle serves to mechanically choke the exhaust gases and maintain the normal shock on the projectile. In the thermally choked case (Figure 2b) the combustion zone is established behind the projectile and the choking of the flow by the heat release stabilizes the normal shock on the projectile. In both cases combustion is initiated by either an on-board ignitor or an external ignitor mounted on the launch tube.

As will be shown in Section III, above velocities of approximately 2.7-3 km/sec subsonic combustion can no longer maintain a sufficiently high ballistic efficiency, even with hydrogen-based propellant mixtures. To continue efficient acceleration to higher velocities three alternative concepts, which employ detonation waves to generate combustion, have been developed by the authors. These concepts are illustrated in Figures 3 and 4. In all three cases the projectile velocity must exceed the Chapman-Jouguet detonation speed of the propellant gas. A transition to one of the detonation modes can be effected by an abrupt change of propellant mixture in the accelerator tube at the appropriate location, using a thin diaphragm to separate the mixtures. If the second mixture is tailored to have a detonation speed sufficiently below the speed of the projectile, transition to one of the detonative modes occurs automatically, the specific mode depending on the projectile geometry.

Figure 3 shows the normal overdriven detonation wave mode of propulsion. The projectile Mach number is sufficiently high (typically greater than 6) that the normal shock initiates combustion, which occurs in a very thin layer immediately behind the shock. The Mach number following heat release is subsonic, consequently, the shock and reaction zone together constitute an overdriven detonation wave (Reference 7). The choking of the flow in the exhaust nozzle keeps the detonation wave overdriven and the region of increasing flow area behind the diffuser throat stabilizes the wave. The projectile has a configuration similar to that of the subsonic combustion mode projectile of Figure 2a. Consequently, a projectile of this geometry could first be accelerated by the subsonic combustion mode and then by the overdriven detonation mode. The maximum velocity capability of the overdriven detonation mode is ~5 km/sec.

Figure 4 shows two oblique detonation drive concepts. In the Type I oblique detonation concept (Figure 4a), the cone angle of the nose, the projectile velocity and the speed of sound of the mixture are tuned so that the initial conical shock does not initiate combustion, but the reflected shock does. In operation, the reflected shock becomes an oblique detonation wave, which may be either Chapman-Jouguet or overdriven. The projectile geometry is chosen so that the reflected detonation wave strikes the projectile just aft of the shoulder.

The Type II oblique detonation concept is shown in Figure 4b. In this concept, the forward cone of the projectile is chosen so the combustion is not initiated by the compression process. Instead, a small squat frustum of a cone, with a relatively blunt cone angle, is inserted into the projectile profile to initiate an oblique detonation wave. This frustum or bump could be located anywhere along the cylindrical section of the projectile. In this oblique detonation mode, as well as in the Type I mode, the flow is supersonic throughout.

In principle, the oblique detonation ram accelerator modes can attain velocities up to 15 km/sec. The propellant mixtures used at the higher velocities are $2H_2+O_2$ plus He or excess H_2 diluent. Estimates of heat transfer rates to the projectile, however, indicate that in-tube aerodynamic heating and ablation become severe at velocities exceeding 6 km/sec,

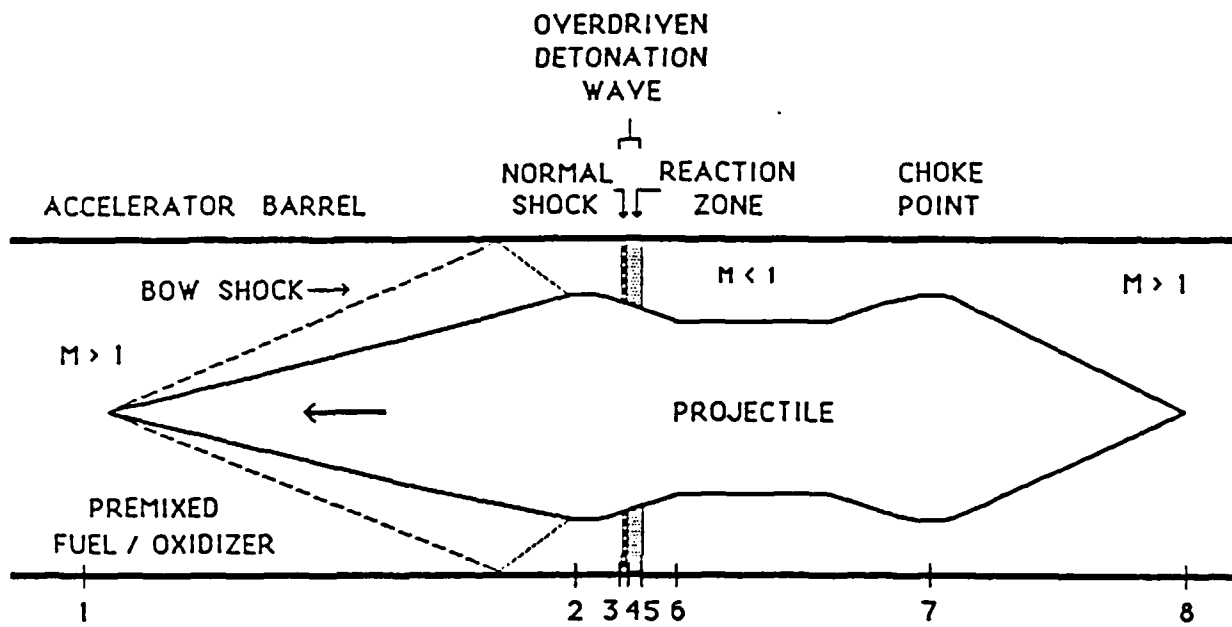
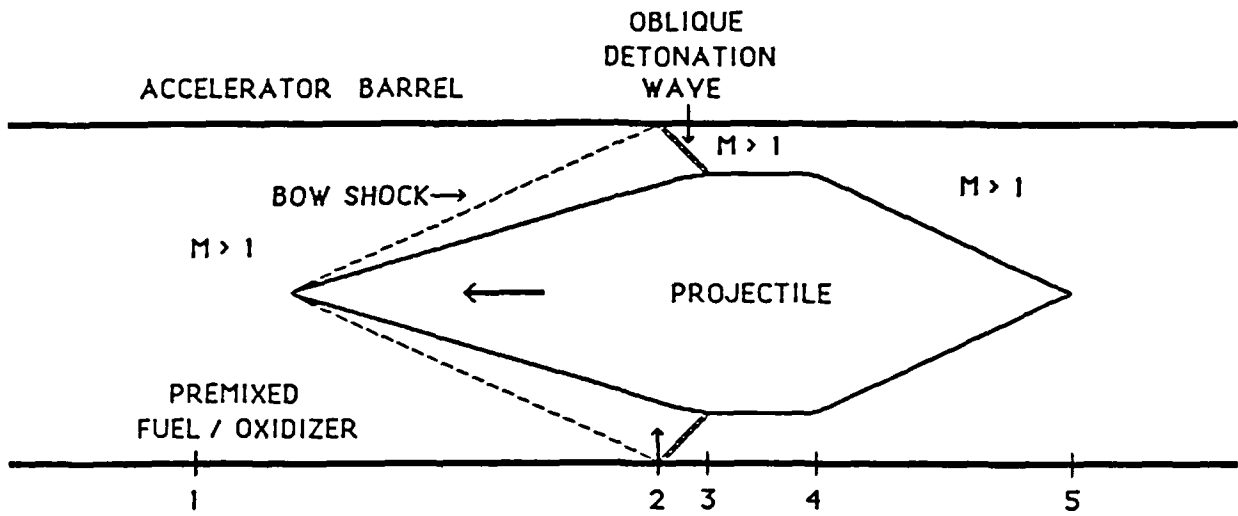
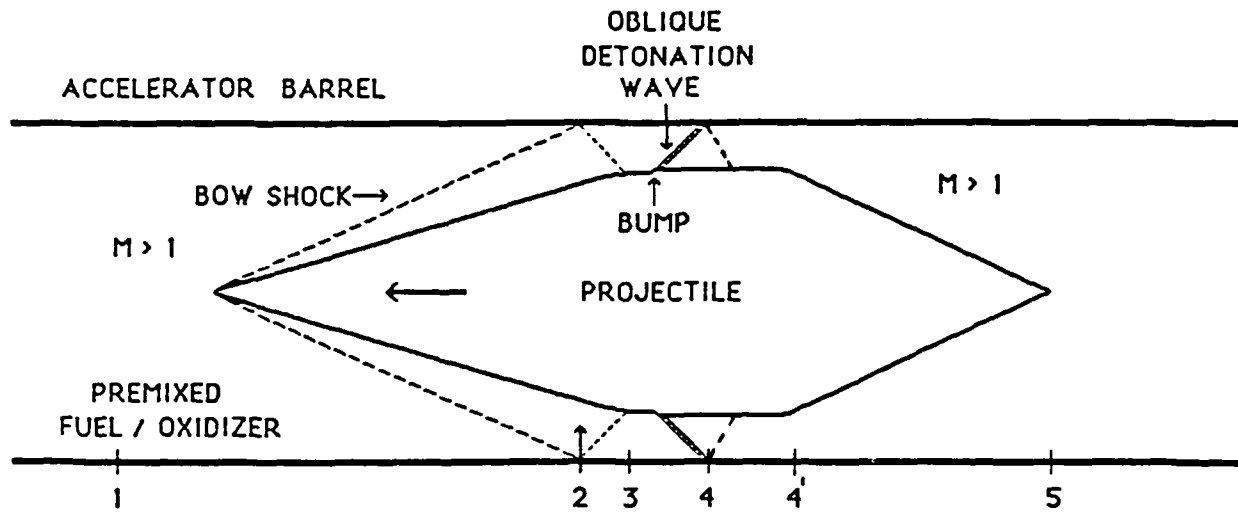


Figure 3. Schematic of Overdriven Detonation Ram Accelerator Mode.



a) Type I Oblique Detonation Mode



b) Type II Oblique Detonation Mode

Figure 4. Schematic of Oblique Detonation Ram Accelerator Modes.

depending on the specific propellant composition employed. In order to reduce the heat transfer to the projectile and extend the practical velocity limit, the authors have investigated a method of laying down a cylindrical core of pure hydrogen, surrounded by the propellant mixture (Reference 8). This approach allows operation of the ram accelerator to velocities up to ~12 km/sec.

The various modes of propulsion discussed above are scalable from fractions of a kilogram to hundreds of kilograms and can be patched together in appropriate combinations to span the entire velocity range from ~0.7 km/sec to ~12 km/sec. As noted earlier, the subsonic combustion projectile configuration of Figure 2a can also be operated in the overdriven detonation mode (Figure 3) to span the range of 0.7-5 km/sec. The thermally choked projectile configuration (Figure 2b) can be operated in the Type I or Type II oblique detonation modes (Figure 4) to reach a velocity up to 12 km/sec. Transition from the subsonic combustion modes to the detonation modes can be effected at a velocity as low as ~2 km/sec by judicious choice of a low detonation speed gas mixture (Reference 7). In each mode the heat and pressure pulses travel with the projectile, distributing the heat over the entire length of the launch tube. Consequently, the temperature rise of the tube is relatively small and very little tube wear is expected.

For the ram accelerator, specific impulse does not have its usual meaning, since no fuel or oxidizer is carried on board the projectile. Rather, the performance of the device can be characterized by two main parameters: thrust pressure ratio and ballistic efficiency. The thrust pressure ratio is the net average drive pressure on the projectile (the thrust divided by the maximum projectile cross-sectional area) divided by the maximum cycle pressure. This ratio is an important performance parameter because it provides a measure of the device's launch capability versus the maximum pressure the projectile and launch tube must survive. The thrust pressure ratios of the ram accelerator modes are in the range of ~0.15-0.7 for the subsonic combustion modes and ~0.15-0.6 for the detonation modes (Reference 7). Ballistic efficiencies of 15-30 percent are realizable with all five acceleration modes. For comparison, the overall ballistic

efficiency of a two-stage light gas gun is typically less than 10% at 3 km/sec and less than 3 percent at 8 km/sec (Reference 9).

SECTION III

ANALYSIS OF THERMALLY CHOKED SUBSONIC COMBUSTION MODE

1. SIMPLIFIED 1-D ANALYSIS

The thermally choked subsonic combustion mode can be modeled in a particularly straightforward manner which illustrates the fundamental characteristics of this mode of propulsion. This simplified approach is one-dimensional, quasi-steady and inviscid. The conservation equations are applied to the control volume between stations 1 and 6 in Figure 2b, without including any of the details of the flow, such as the oblique and normal shocks, subsonic diffusion, base recirculation zone and combustion shear layer. In addition, friction on the tube walls and projectile body is neglected. The ideal gas equation of state is used with one set of values of the molecular weight and specific heat ratio before combustion and a second set after combustion. This simplified approach offers a good overall approximation to the performance characteristics of the thermally choked mode of propulsion and is useful for evaluating the suitability of various propellant mixtures over velocity ranges of interest.

The conservation equations are applied in the frame of reference of a stationary projectile. Consequently, the tube wall moves relative to the projectile with the same velocity as the gas upstream of the projectile. The upstream boundary of the control volume (station 1) is located just forward of the projectile nose tip and the downstream boundary (station 6) coincides with the plane where thermal choking occurs. Application of the momentum and continuity equations to the control volume results in the following relation for the non-dimensional thrust on the projectile:

$$\frac{F}{p_1 A} = \frac{p_6}{p_1} (1 + \gamma_6) - (1 + \gamma_1 M_1^2) \quad (1)$$

where F is the thrust. A is the tube cross-sectional area, p_1 and p_6 are the

static pressures entering and leaving the control volume, γ_1 and γ_6 are the specific heat ratios before and after combustion, and M_1 is the Mach number of the flow entering the control volume. Note that at the thermal choking point $M_6 = 1$.

From continuity and the ideal gas law it can be shown that

$$\frac{p_6}{p_1} = M_1 \left[\left(\frac{T_6}{T_1} \right) \left(\frac{\gamma_1 m_1}{\gamma_6 m_6} \right) \right]^{1/2} \quad (2)$$

where T_1 and T_6 are the static temperatures at stations 1 and 6 and m_1 and m_6 are the respective molecular weights. Using the isentropic relations at stations 1 and 6, the temperature ratio T_6/T_1 can be expressed as follows:

$$\frac{T_6}{T_1} = \frac{T_{t6}}{T_{t1}} \left(\frac{1 + \frac{\gamma_1 - 1}{2} M_1^2}{\frac{\gamma_6 + 1}{2}} \right) \quad (3)$$

where the subscript t denotes stagnation conditions. The ratio T_{t6}/T_{t1} is obtained from application of the energy equation across the control volume:

$$\frac{T_{t6}}{T_{t1}} = \frac{C_{p1}}{C_{p6}} \left(1 + \frac{\Delta q}{C_{p1} T_{t1}} \right) \quad (4)$$

This assumes that the enthalpy, h , at either end of the control volume can be written in the form $h = C_p T$. Here C_{p1} and C_{p6} are the specific heats at constant pressure before and after combustion, respectively. The parameter Δq is the heat of reaction of the propellant gas mixture and, together with the values of γ_1 , γ_6 , C_{p1} and C_{p6} , is obtained from a separate equilibrium

combustion computation similar to that of Barrere (Reference 10) (see Appendix A).

It should be noted that the values of C_p and γ used in the present derivation should be the effective values, based on the assumption $h = C_p T$ used in Equation 4. Accordingly, $C_{p1} = h_1/T_1$, $C_{p6} = h_6/T_6$, $\gamma_1 = C_{p1}/(C_{p1}-R_1)$ and $\gamma_6 = C_{p6}/(C_{p6}-R_6)$, where R_1 and R_6 are the gas constants of the propellant mixture before and after combustion. The initial conditions for combustion are approximated as those behind a normal shock with a pressure ratio of 20. Substituting Equations 2 through 4 into Equation 1 yields

$$\frac{F}{p_1 A} = \frac{\gamma_1 M_1}{\gamma_6} \left\{ 2 \left(\frac{\gamma_6^2 - 1}{\gamma_1 - 1} \right) \left[1 + \frac{\gamma_1 - 1}{2} M_1^2 + \frac{\Delta q}{C_{p1} T_1} \right] \right\}^{1/2} - (1 + \gamma_1 M_1^2) . \quad (5)$$

It can be seen that the thrust, F , is directly proportional to the initial propellant fill pressure, p_1 . Combining Equation 5 with the equation of motion,

$$\frac{dU_1}{dx} = \frac{F}{mU_1} , \quad (6)$$

and integrating yields the velocity, U_1 , of the projectile of mass m as a function of position, x , along the launch tube.

As the projectile accelerates, M_1 increases and the thrust decreases, reaching zero at a flight Mach number given by

$$M_1 = [(\alpha + \sqrt{\alpha^2 - \beta})/\beta]^{1/2} \quad (7)$$

where

$$\alpha = \left(\frac{\gamma_1}{\gamma_6}\right)^2 \left(\frac{\gamma_6^2 - 1}{\gamma_1 - 1}\right) \left(1 + \frac{\Delta q}{c_{p1} T_1}\right) - \gamma_1$$

and $\beta = (\gamma_1/\gamma_6)^2$.

It can be readily shown that this result corresponds to the Mach number of a one-dimensional Chapman-Jouguet (C-J) detonation wave propagating in the same gas mixture (Reference 7). Thus, in the absence of friction, the limiting velocity of the thermally choked mode of propulsion is the C-J detonation velocity. In practice, velocities as high as 95% of the C-J velocity have been achieved, as discussed in Section V. This indicates that using fuel-rich hydrogen-oxygen propellant mixtures, maximum velocities in excess of 3000 m/sec may, in principle, be attainable.

The maximum thrust occurs at

$$M_1 = \left[\left(\frac{\gamma_6 - 1}{\gamma_1 - 1}\right) \left(1 + \frac{\Delta q}{c_{p1} T_1}\right) \right]^{1/2} . \quad (8)$$

Interestingly, this corresponds to the condition $U_6 = U_1$, where U_1 and U_6 are the flow velocities entering and leaving the control volume, i.e., the thrust is maximum when the flow exiting the control volume is stationary with respect to the launch tube. Substitution of Equation 8 in Equation 5 yields the following expression for the maximum thrust:

$$\left(\frac{F}{p_1 A}\right)_{\max} = \frac{\gamma_1(\gamma_6 - 1)}{\gamma_6(\gamma_1 - 1)} \left(1 + \frac{\Delta q}{c_{p1} T_1}\right) - 1 . \quad (9)$$

For the special case of constant γ and C_p , the maximum thrust is directly proportional to the heat of reaction, i.e.,

$$\left(\frac{F}{p_1 A}\right)_{\max} = \frac{\Delta q}{c_p T_1} \quad (10)$$

As noted earlier, the ballistic efficiency, η , is defined as the rate of change of projectile kinetic energy divided by the rate of heat addition to the flow, i.e.,

$$\eta = \frac{F U_1}{\dot{m} \Delta q} \quad (11)$$

where $\dot{m} = \rho_1 U_1 A$ is the mass flow rate through the control volume. Using continuity, the ideal gas law, and the definition of the speed of sound, $a_1 = \sqrt{\gamma_1 R_1 T_1}$, it can be shown that

$$\eta = \left(\frac{F}{p_1 A_1}\right) \frac{a_1^2}{\gamma_1 \Delta q} \quad (12)$$

Thus, for a given propellant mixture the ballistic efficiency is directly proportional to the non-dimensional thrust. It follows that the ballistic efficiency reaches its maximum at the maximum thrust condition and goes to zero as the projectile velocity approaches the C-J detonation velocity. It is interesting to note that for the special case of constant γ and C_p , the maximum value of the ballistic efficiency is

$$\eta_{\max} = (\gamma - 1) / \gamma \quad (13)$$

This sets an upper limit to the ballistic efficiency in the range of

~ .16-0.30 for propellant mixtures of interest, depending on the effective average value of γ .

Clearly, the key to optimum performance is to keep the projectile Mach number within a narrow range close to that corresponding to the peak thrust and efficiency. This can be accomplished by having a graded propellant mixture whose speed of sound increases towards the muzzle of the launch tube or by dividing the launch tube into several segments filled with different propellant mixtures and constraining the projectile to operate in a limited Mach number range in each segment.

The simple model described above does not predict the low speed operational limit of the device because there is no specification of the projectile diameter and hence of the diffuser area ratio. It is this ratio, the oblique shock entropy losses and the heat release, Δq , that define the minimum value of M_1 at which the device can operate.

2. MORE DETAILED 1-D ANALYSIS

The more detailed analytic approach used in the investigation of the subsonic combustion modes includes some of the major details of the flow around the projectile. This analysis is also quasi-steady, inviscid and one-dimensional, except for the oblique shock waves. The flow is considered isentropic except for the normal and oblique shocks and the combustion. Figure 2b illustrates the principal features of the model. A detailed analytical description of the model is presented in Appendix B. Here, the approach is summarized.

Although the flow field generated by the conical bow shock can be readily computed (Reference 11), the multiple shock reflections from the tube wall and projectile body in the non-uniform flow are not analytically tractable. This problem is best solved by CFD methods (see Section VI). For the purposes of the present approach the supersonic portion of the diffuser has been approximated by an equivalent 2-D wedge diffuser with one reflected shock. The validity of this simplifying assumption is borne out by the fact that the theoretical performance of the device is not dependent on the efficiency of the supersonic portion of the diffuser.

The normal shock stands behind the diffuser throat in the diverging portion of the flow at a location governed by the projectile Mach number and the heat release in the combustion zone. The shock jump conditions are treated by standard techniques (Reference 12) and the shock is allowed to move in response to changing projectile velocity. The flow between the shock and the combustion zone is assumed isentropic, i.e., it is assumed that there is full pressure recovery at the projectile base prior to combustion. It is also assumed, for simplicity, that combustion occurs in the full tube area beginning just beyond the base of the projectile. The heat release process between stations 5 and 6 is treated by a conventional constant-area heat addition analysis coupled to an equilibrium chemistry combustion routine (Appendix A). The details of the recirculation zone at the projectile base and the expanding shear layer between the combusting gases and the tube wall are not considered and the length of the combustion zone is not computed, as no kinetics are included in the model. The frictional drag on the projectile is computed separately, using the velocity field obtained from the inviscid analysis. The skin friction coefficient is assumed to be 0.003 in subsonic flow and is corrected for Mach number effects in supersonic flow (Reference 13).

In the absence of friction, both analytical approaches yield the same result, i.e., the variation of non-dimensional thrust and ballistic efficiency with Mach number is the same in both cases for the same set of operational parameters and for constant Δq . In the more detailed model the upper Mach number limit corresponds to the normal shock moving off the projectile. Since the base area of the projectile is finite, this condition occurs at a lower Mach number than the C-J detonation condition and is governed by the ratio of base area to tube cross-sectional area. In addition, the second approach predicts a minimum Mach number at which the projectile must travel. This corresponds to the condition at which the normal shock stands just at the diffuser throat. This low speed limit is a function of the ratio of the diffuser throat area to the tube cross-sectional area and Δq , the heat of combustion. For projectile geometries and propellant mixtures of interest this Mach number is in the range of approximately 2.3-2.8. For some propellant mixtures of interest, however,

Equation 8 predicts that the maximum thrust occurs at a Mach number below the minimum defined above. In those cases, therefore, the minimum starting Mach number defines the maximum attainable thrust condition.

As defined earlier, the thrust pressure ratio is the ratio of the average drive pressure on the projectile to the maximum pressure in the cycle. For the thermally choked mode the thrust pressure ratio, ϕ , is

$$\phi = \frac{F}{A_p p_5} = \left(\frac{F}{p_1 A}\right) \left(\frac{p_1}{p_5}\right) \left(\frac{A}{A_p}\right) \quad (14)$$

where A_p is the maximum projectile cross-section area and p_5 is the maximum static pressure, which occurs at station 5, the projectile base. Because p_5 is a monotonically increasing function of the projectile Mach number, the maximum thrust pressure ratio occurs at a lower Mach number than the maximum thrust; however, it goes to zero at the same Mach number as the thrust, i.e., the C-J detonation condition. A high value of ϕ is desirable because it permits a higher fill pressure (hence higher thrust and acceleration) to be used for a given launch tube wall strength.

SECTION IV

EXPERIMENTAL RAM ACCELERATOR FACILITY

The principal components of the University of Washington ram accelerator facility, illustrated in Figures 5 through 7, are the 38 mm bore single-stage light gas gun, ram accelerator section, final dump tank and projectile decelerator. Associated subsystems are the gas handling system, instrumentation, and data acquisition system. In what follows, these and related components, as well as the projectile design, are described in detail.

1. LIGHT GAS GUN

The single-stage light gas gun is of conventional design. The high pressure driver, designed for up to 400 atm load pressure, consists of a cylindrical flanged tube machined from heat-treated 4142 alloy steel and has the following principal dimensions: 10 cm inside diameter \times 20 cm outside diameter \times 1.8 m long. A double diaphragm section connects the driver section to the adjacent launch tube. The diaphragms are made from 1100-0 (dead soft) aluminum sheets of appropriate thickness coined with two knife edge scores, 90 degrees apart. The interdiaphragm space is pressurized to about two-thirds of the breaking pressure of the diaphragm. The driver is filled to about four-thirds of the breaking pressure. Thus, when the gas in the interdiaphragm space is released, both diaphragms rupture.

The launch tube section is composed of three 2.44 m long, 38 mm bore, 76 mm outside diameter tubes made of heat-treated 4150 alloy steel. Each tube section has a double O-ring seal at both ends and the tube joints are held together by threaded collars. The tubes rest on ball bearing support stands, which allow axial movement of each tube for periodic maintenance and inspection. At the end of the last launch tube, three pairs of instrumentation ports have been tapped into the sidewall. These are diametrically opposed and spaced at 15.2 cm intervals. One set of adjacent instrumentation ports is equipped with electromagnetic transducers which detect the passages of a magnetic disk on the projectile. The signal from

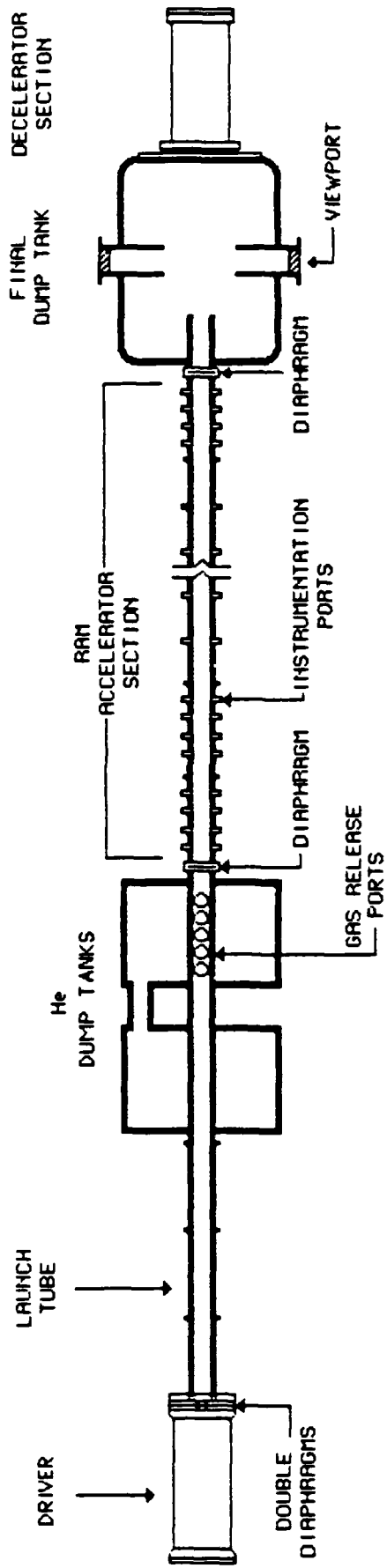


Figure 5. Schematic of University of Washington Ram Accelerator Facility.

the upstream transducer is used to trigger the data acquisition system. The signals from both transducers together provide velocity data. The unused ports are closed off with blank plugs.

The light gas gun is capable of accelerating the sabot/projectile combination (typical combined mass =60-90 gm) to speeds up to approximately 1350 m/sec. The end of the launch tube is connected to a 1.52 m long perforated wall tube, having similar internal and external diameters, that passes through an evacuated 1.07 m inside diameter \times 0.91 m long cylindrical tank which serves as a dump for the helium driver gas. This tank has O-ring seal collars on both ends to allow axial movement of the tube. A second dump tank of similar dimensions is connected to the first one by a 25 cm diameter tube to provide a larger dump volume.

2. RAM ACCELERATOR SECTION

The 12.2 m long ram accelerator section (Figure 6) consists of seven tubes made from heat-treated 4150 steel alloy. These tubes have a 38 mm inside diameter and a 100 mm outside diameter. Four of these tubes are 1.22 m long apiece and have four pairs of diametrically opposed instrumentation ports tapped at 30.5 cm intervals. The other three tubes are 2.44 m long apiece and also have four pairs of diametrically opposed instrumentation ports but located at 61 cm intervals. Two of these tubes feature dual pairs of instrumentation ports, spaced at 90° circumferentially, at the two ends. The short and long tubes are arranged in alternating fashion. A total of 60 instrumentation ports are available with which to observe the progress of the projectile. Typically, the ports are instrumented with Kistler and PCB quartz pressure transducers, custom-made electromagnetic velocity transducers, light fiber probes, and the gas lines that are used to evacuate and then fill the various segments of the ram accelerator with the desired combustible gas mixtures. Unused ports are blanked off with solid plugs. Thin mylar diaphragms close off each end of the ram accelerator and are also used to separate the segments of the tube which are filled with different propellant mixtures. The ram accelerator is designed to operate at propellant fill pressures up to 50 atm, which would

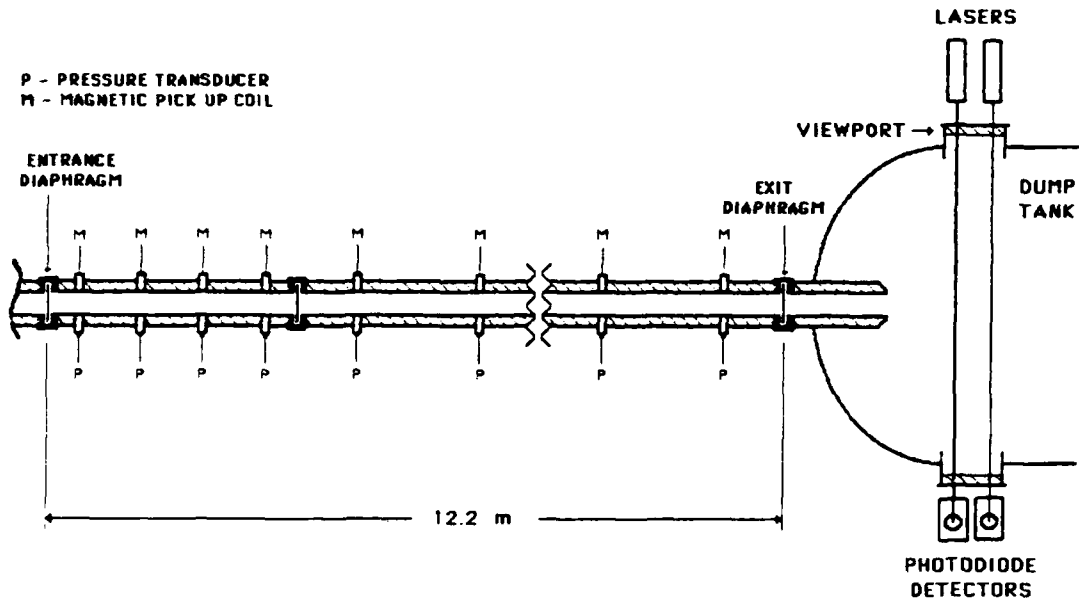


Figure 6. Schematic of Ram Accelerator Test Section and Associated Instrumentation.

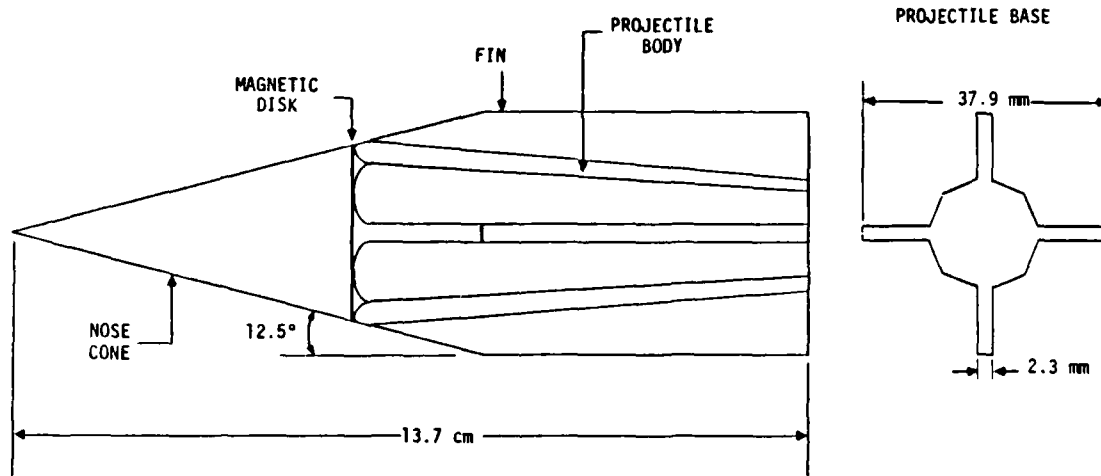


Figure 7. Experimental Ram Accelerator Projectile.

result in peak drive pressures up to 20,000 psi on the projectile. To date the maximum fill pressure used has been 25 atm.

3. FINAL DUMP TANK

When the accelerated projectile leaves the ram accelerator it travels through the final mylar diaphragm into a 0.76 m long \times 38 mm inside diameter \times 76 mm outside diameter drift tube and thence into the final evacuated dump tank, 1.22 m outside diameter \times 2.44 m long, where it flies free. A pair of diametrically opposed 25 cm diameter viewing portholes provide a means to observe the projectile in flight and do a final velocity measurement. A high speed spark shadowgraph photography system (exposure time approximately 300 ns) is available to take a photograph of the vehicle as it flies through the final dump tank. Photographs show that the magnesium projectiles used to date survive accelerations as high as 40,000 g's. A two-beam laser velocity measuring system (Figure 6), incorporated across the observation windows, permits a final measurement of the velocity of the projectile in a near-vacuum environment far from any muzzle disturbances.

4. DECELERATOR

The decelerator serves to bring the spent projectile to a stop. It consists of a 1.83 m long steel tube with 17.8 cm inside diameter and 35.6 cm outer diameter and has a 7.6 cm thick end plate. The tube is separated from the final dump tank by a thin aluminum sheet having perforations to equalize the pressure between the two volumes, and is filled with tightly packed carpet remnants and steel lathe turnings.

5. GAS HANDLING SYSTEM

Commercial bottled helium at a pressure of 160 atm provides the gun gas supply. To attain higher pressures, a diaphragm pump capable of reaching 400 atm is used. Two vacuum pumps serve to evacuate the launch tube and the three dump tanks. The fuel, oxidizer, and diluent gases are sent through filters and sonic orifices to a gas mixer (carburetor) and then on to the ram accelerator section. The gas mixer consists of a cylindrical vessel,

5.0 cm inside diameter x 75 cm long, having a multitude of offset baffles which promote turbulence and hence good mixing. The ram accelerator can be filled with up to five different gas mixtures. The desired mixture ratio in each segment is obtained by adjusting the feed pressures of the individual constituents. This mixing system has been calibrated and is regularly checked by having mixture samples analyzed by a local testing laboratory.

Two armored bunkers are used for the protection of personnel and high pressure gas cylinders. The personnel bunker houses the pressure, vacuum and gas mixing control panels, the high pressure pump, the two vacuum pumps and the data acquisition system.

6. DATA ACQUISITION SYSTEM

A 20-channel LeCroy Research Systems Corporation data acquisition system (DAS) is used. All the pressure transducer, electromagnetic transducer and light fiber signals travel through coaxial cables to LeCroy Model 8210 Quad 10-bit transient digitizers. Some of the inputs are separately multiplexed, effectively permitting up to 48 different sets of data to be recorded. The digitizers use track and hold circuits, capable of handling four analog inputs per module. The analog input signals are digitized and stored in buffer memory modules which have a capacity of 32K 12-bit words. The data are read out through the memory control circuit and each of the four channels can be separately addressed. The five modules, along with a 32-channel data logger and CAMAC to GPIB interface, are contained within a CAMAC crate which contains the power supply. The CAMAC to GPIB interface connects to an IBM PC-XT microcomputer. A LeCroy Wave-Form Catalyst software program is used to manipulate and display the data.

7. PROJECTILE AND SABOT CONFIGURATIONS

The projectile geometry currently in use in our experimental studies is illustrated in Figure 7. It is fabricated from magnesium in two pieces: the nose cone and the body with integral fins. The purpose of the fins is to center the projectile in the tube. The fins and body are integral to assure survival of accelerations exceeding 40,000 g's. The nose cone is threaded into the body. At the joint between nose and body is sandwiched a

thin annular disk of flexible magnetic material whose purpose is to interact with the electromagnetic transducers to provide velocity data which are independent of the exact instantaneous disposition of the pressure wave system on the projectile. For ease of machining, the body has an octagonal cross-section with fins at four opposed vertices. The length of the projectile is 13.7 cm and its maximum diameter is 28.9 mm which results in a diffuser area ratio of 2.37. The nose cone has a half-angle of 12.5°. Projectiles with masses in the range of 45-75 grams have been used. The launching sabot mass is 15 gm. The truncated base of the projectile acts as an effective flame holding dump combustor for the thermally choked mode of operation.

8. IGNITION SYSTEM

An effective ignition system has been developed by the authors to ignite the combustible gas behind the projectile as it enters the ram accelerator tube. This system was invented and developed at no cost to the government during the hiatus in funding, 1 November 1985-22 September 1986. Accordingly, the ignition technology is proprietary to the University of Washington and full disclosure will not be made until final patent action.

SECTION V

RESULTS OF EXPERIMENTS WITH THERMALLY CHOKED MODE

1. OPERATING CONDITIONS

Experiments to date with the thermally choked mode have been carried out using methane and oxygen as the fuel and oxidizer, and carbon dioxide, nitrogen, helium and excess methane as the diluents. The mixture used in the lowest velocity range (690-1260 m/sec) has been $\text{CH}_4 + 2\text{O}_2 + 6\text{CO}_2$. To explore the velocity range between ~1000 m/sec and ~1500 m/sec a mixture of $2.5\text{CH}_4 + 2\text{O}_2 + 5.6\text{N}_2$ has been used. Velocities in the range of 1500-1900 m/sec have been attained in a mixture of $4.5\text{CH}_4 + 2\text{O}_2 + 2\text{He}$. A mixture of $3.4\text{CH}_4 + 2\text{O}_2 + 6.5\text{He}$ has been used in the range of 1700-2100 m/sec and to achieve the highest in-tube velocity observed (2357 m/sec) a mixture of $2.8\text{CH}_4 + 2\text{O}_2 + 11\text{He}$ has been used. Other mixtures have also been investigated. The use of the diluents serves two purposes: They tailor the speed of sound of the various mixtures so that the projectile Mach number is constrained to the range of ~2.5-4.5 over the entire velocity range investigated and they reduce the possibility of the combustion wave developing spontaneously into a detonation. To attain velocities in excess of 1600 m/sec the propellant mixtures have been staged, i.e., the ram accelerator tube has been divided into two or more sections containing different propellant mixtures. Propellant fill pressures of 3 to 25 atm absolute and injection velocities in the range of 690-1240 m/sec have been investigated in more than 400 test firings since October 1985.

2. PRESSURE AND ELECTROMAGNETIC SIGNATURES

A pressure transducer output obtained at a distance of 1.51 m from the entrance diaphragm for a test run in $2.5\text{CH}_4 + 2\text{O}_2 + 6\text{N}_2$ at 20 atm is shown in Figure 8. The projectile velocity is ~1300 m/sec. Time is measured from the instant of DAS triggering and pressure is displayed in atmospheres. The first pressure pulse is generated by the oblique shock system in the projectile's diffuser section. There then follow a series of pulses which

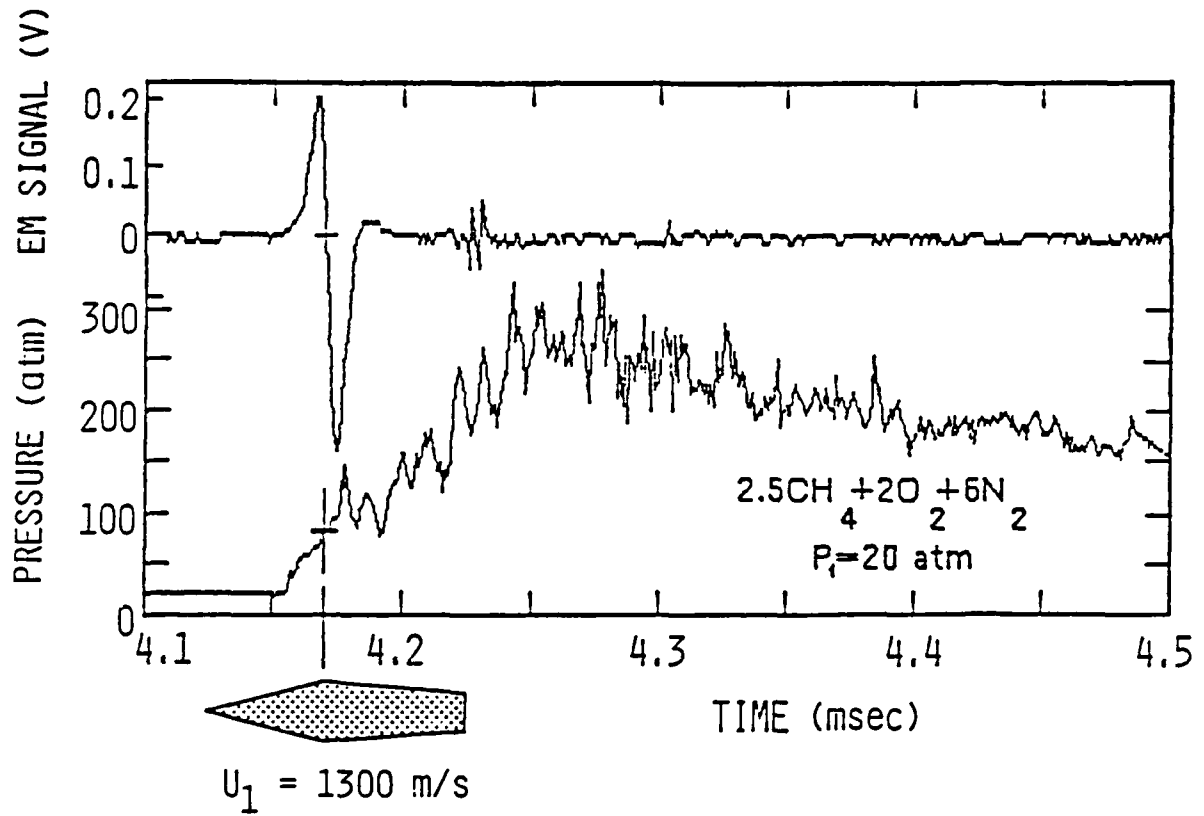


Figure 8. Electromagnetic (EM) and Pressure Transducer Signals in Ram Accelerator, 1.51 m from Entrance Diaphragm.

increase the pressure to a peak of ~ 280 atm, after which the pressure decays. The increase in pressure after the initial oblique shocks represents the normal shock, which appears to consist of a complex system of oblique and normal shocks similar to that observed in supersonic flows in long ducts (Reference 12). The decay in pressure following the peak is due to the heat addition choking the flow and the subsequent expansion of the combustion products into the tube behind the choking point. The pressure signatures and preliminary light emission data indicate that the combustion zone begins about 3-5 tube diameters behind the projectile and extends about 15-20 tube diameters downstream. Actual values depend on the propellant mixture, initial fill pressure, and projectile velocity.

The upper trace in Figure 8 displays the output of an electromagnetic transducer located at the same axial station as the pressure transducer. The zero crossing point of the electromagnetic signal identifies the time of arrival of the annular magnetic disk mounted at the projectile throat. This locates the shock system on the projectile relative to the throat. A profile of the projectile scaled to the local velocity is shown under the pressure trace in Figure 8 to illustrate this point. It can be seen that in this case the pressure reaches its maximum somewhat behind the projectile, however, it is likely that this higher pressure is communicated to the projectile through the subsonic wake region behind its base.

Pressure signatures obtained with other propellant mixtures are generally similar to that of Figure 8, except for the overall pressure ratio. Figure 9 shows plots of theoretical and experimental pressure ratios as functions of velocity for two of the propellant mixtures studied to date. The representative error bar on the leftmost data point reflects the noisy nature of the pressure signals. This noise is due to complex wave interactions and transducer resonances. Over the velocity ranges achieved by the experiments the quasi-steady one-dimensional model predicts pressure ratios which increase with velocity, whereas, the experimental pressure ratios fluctuate about approximately constant mean values for each propellant mixture. This difference in behavior is believed to be due to the normal shock consisting of a complex system of fluctuating waves rather than the single steady shock wave assumed in the theoretical model.

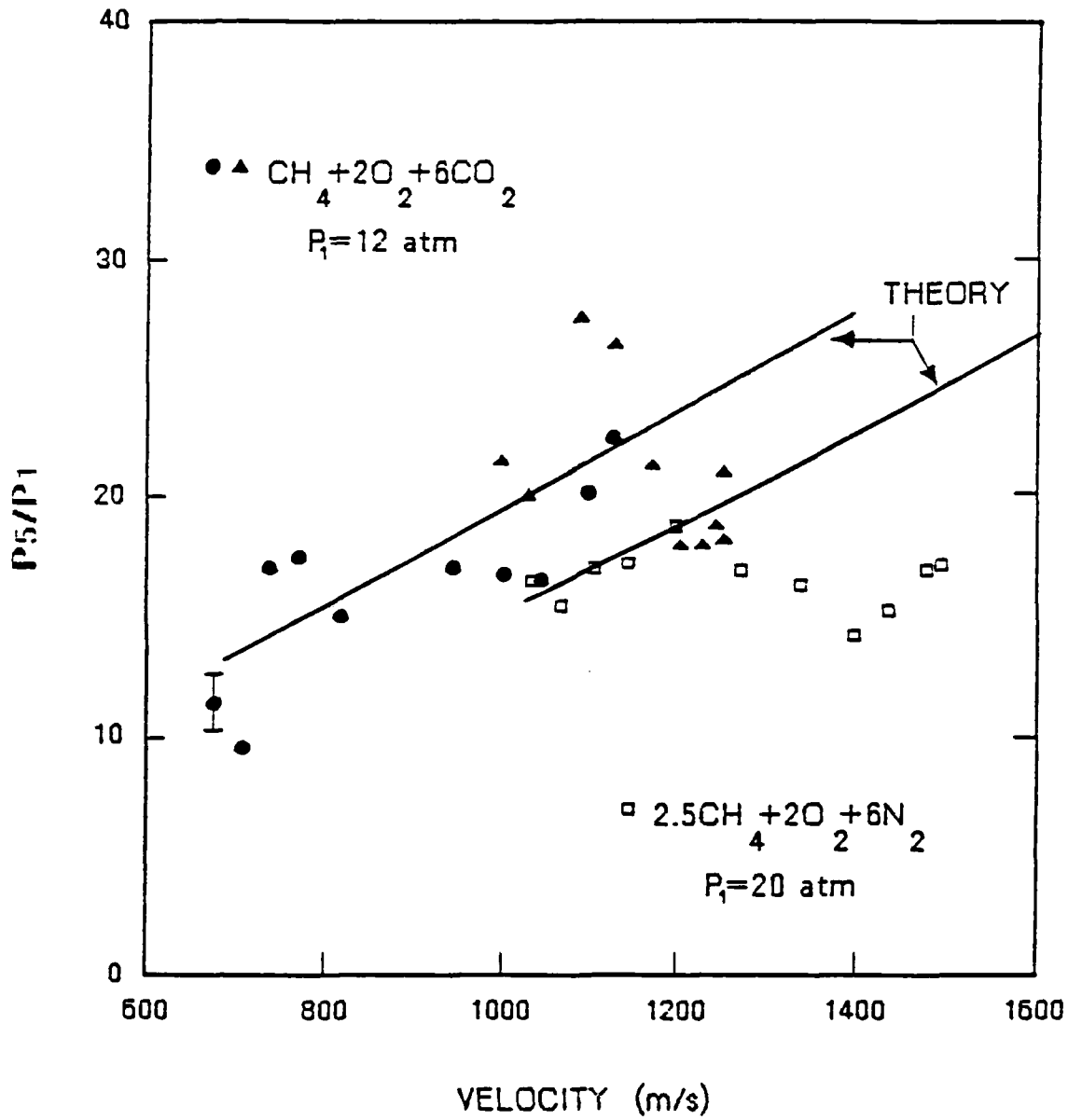


Figure 9. Ratio of Peak Cycle Pressure to Tube Fill Pressure as a Function of Projectile Velocity. (Upper curve corresponds to $\text{CH}_4 + \text{O}_2 + 6\text{CO}_2$ and lower curve to $2.54\text{CH}_4 + 2\text{O}_2 + 6\text{N}_2$.)

3. VELOCITY PROFILES

The velocity of the projectile can be deduced from the distance-time history of either the bow shock pressure signature or of the electric pulses induced in the electromagnetic transducers by the on-board magnet. The x-t plots obtained are curve fit with fourth or fifth order polynomials and velocities are obtained by differentiation. Results from various experiments performed using different propellants and fill pressures are shown in Figures 10 through 13. In Figures 10 and 11, the open squares are the experimental data obtained from the pressure signatures and the curves represent the velocity profiles predicted by the quasi-steady one-dimensional model, with aerodynamic friction included. Figure 10 also displays some independent velocity measurements obtained with the electromagnetic transducers and the dump tank laser. Note that the data of Figure 10 were obtained with a shorter accelerator tube, 4.88 m long, containing only one mixture at a time, and a projectile having a mass of 75 gm. The gas mixtures used are identified in the figure. The results with CO₂ diluent were obtained at two different pressures, 12 atm and 20 atm. The observed pressure scaling agrees well with theory.

Figure 11 shows a projectile velocity of ~1900 m/sec and a peak acceleration of ~20,000 g's, obtained in 11 m of the ram accelerator tube using a two-stage mixture arrangement and a 60 gm projectile. In this case, the first 3.66 m of the tube were filled with a 2.5CH₄ + 20₂ + 6N₂ mixture at 20 atm and the remaining 7.34 m were filled with a 4.5CH₄ + 20₂ + 2He mixture, also at 20 atm. The initial velocity was 1200 m/sec and the transition between the two mixtures occurred at 1450 m/sec. The abrupt change in slope of the theoretical curve at the transition point is due to the discontinuity in the Mach number and gas properties. The experimental data also display a change in slope here, but the effect is more subtle.

In Figures 12 and 13 the experimental data points represent data obtained from the electromagnetic transducers. The solid curves again represent the velocity profiles predicted by the quasi-steady 1-D model. Figure 12 shows the results of a three-stage shot, with a projectile mass of 57 gm and a gas fill pressure of 21 atm. The projectile entered the ram accelerator tube at 1150 m/sec. The three gas mixtures used are identified

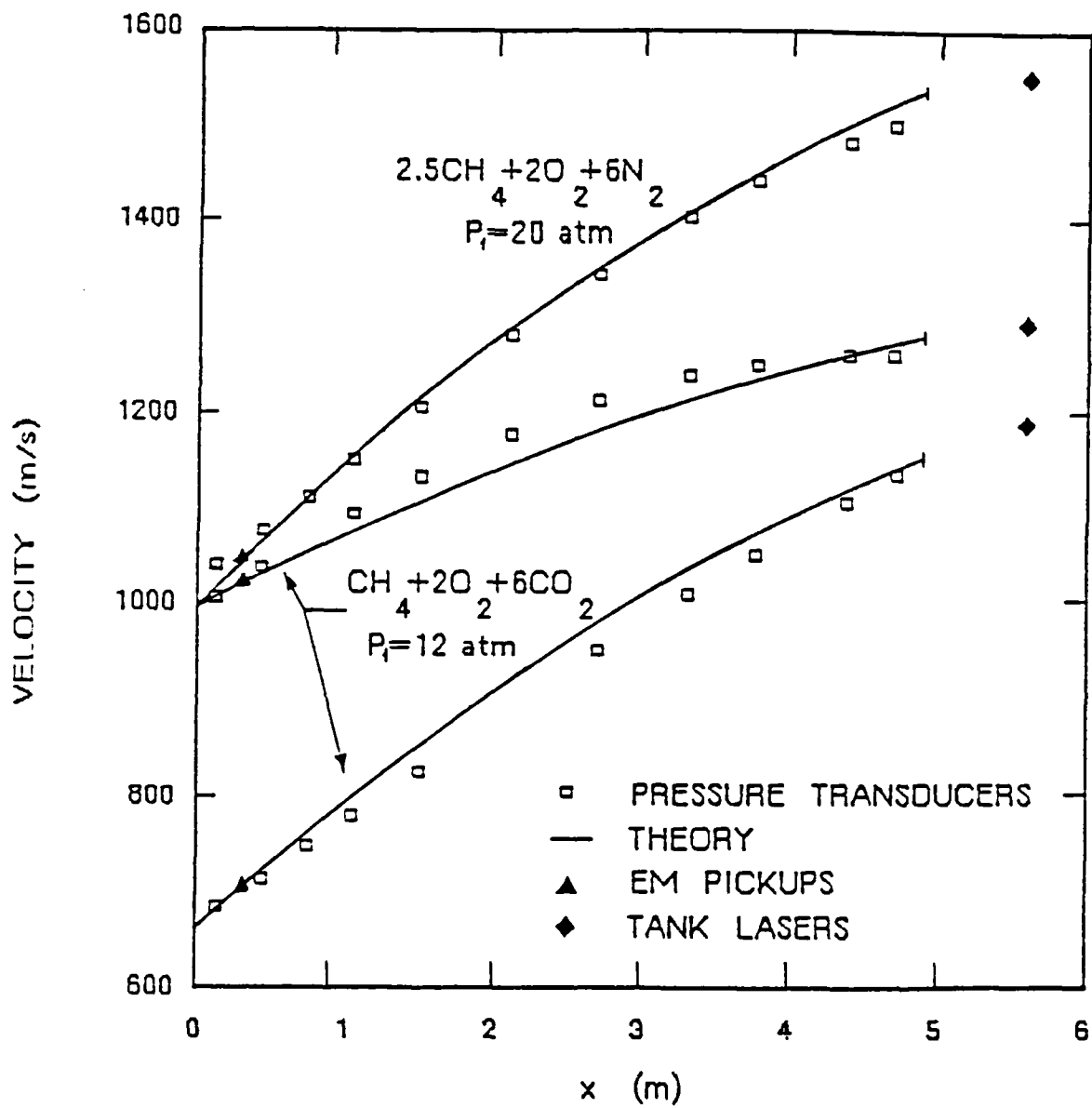


Figure 10. Velocity Profiles in 4.88 m Ram Accelerator. (Projectile mass = 75 gm.)

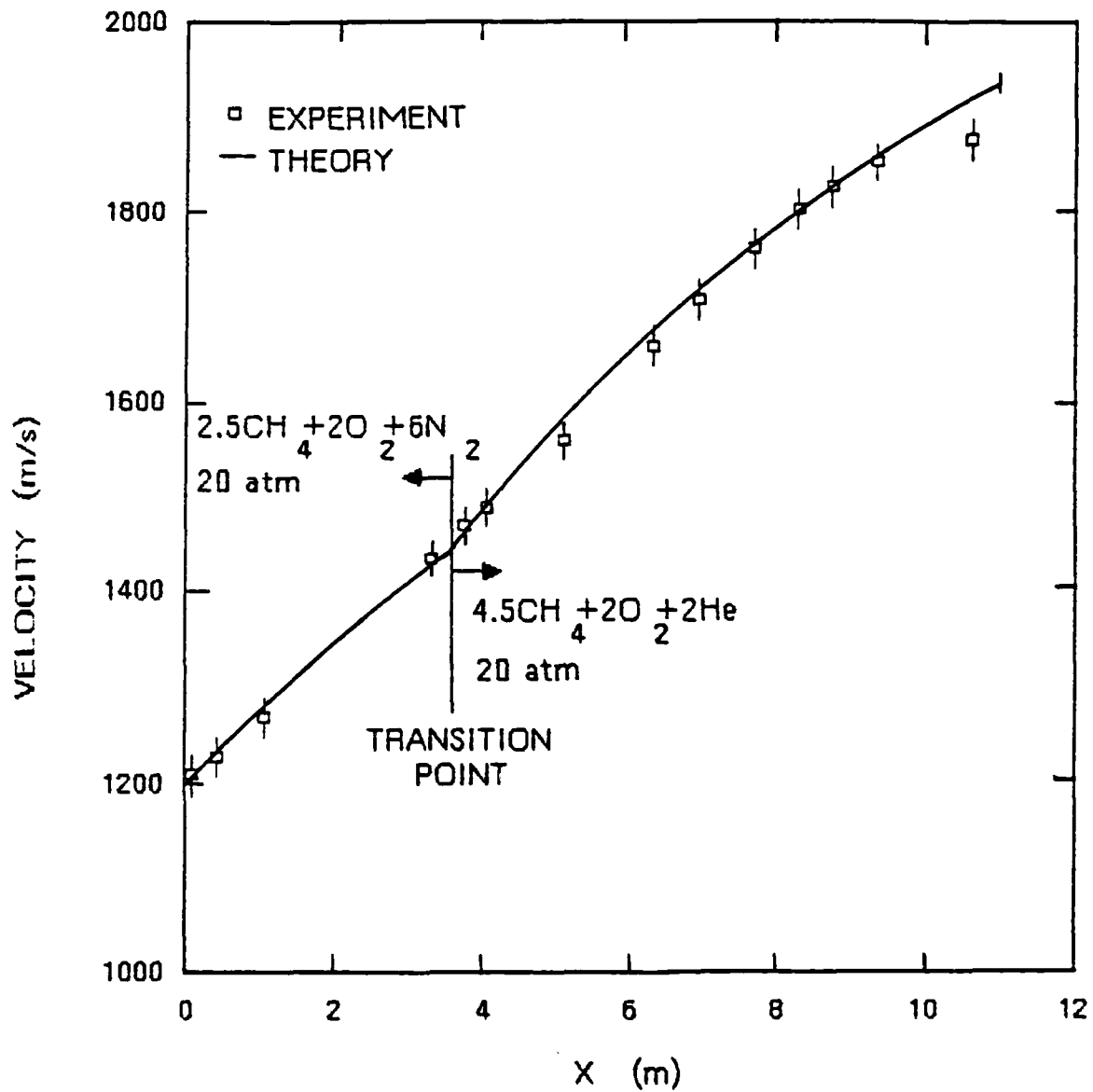


Figure 11. Velocity Profile in 11 m Ram Accelerator Having Two Staged Propellant Mixtures. (Projectile mass = 60 gm.)

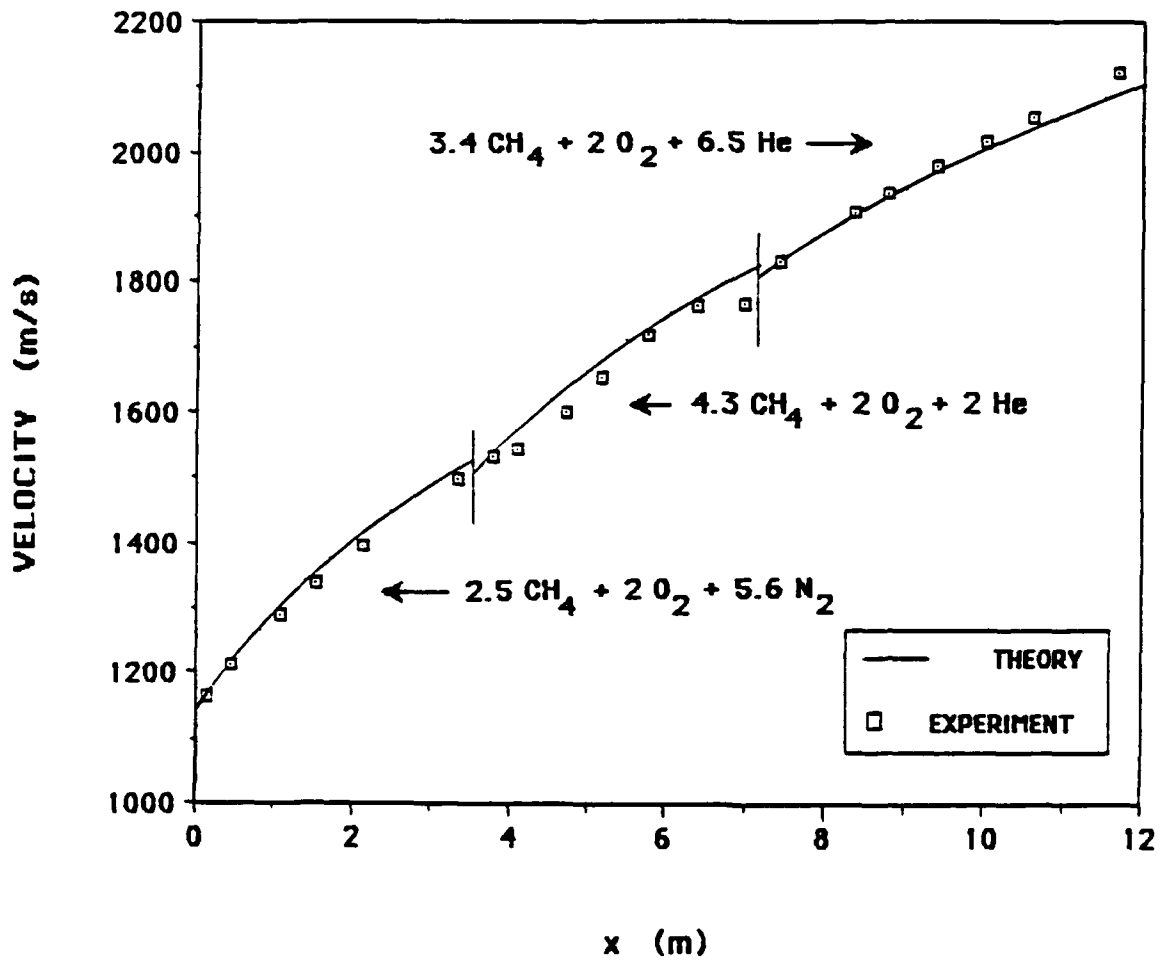


Figure 12. Velocity Profile in Three-Stage 11 m Ram Accelerator. (Initial velocity = 1150 m/s. Projectile mass = 57gm. Theory is normalized to first experimental point in each stage.)

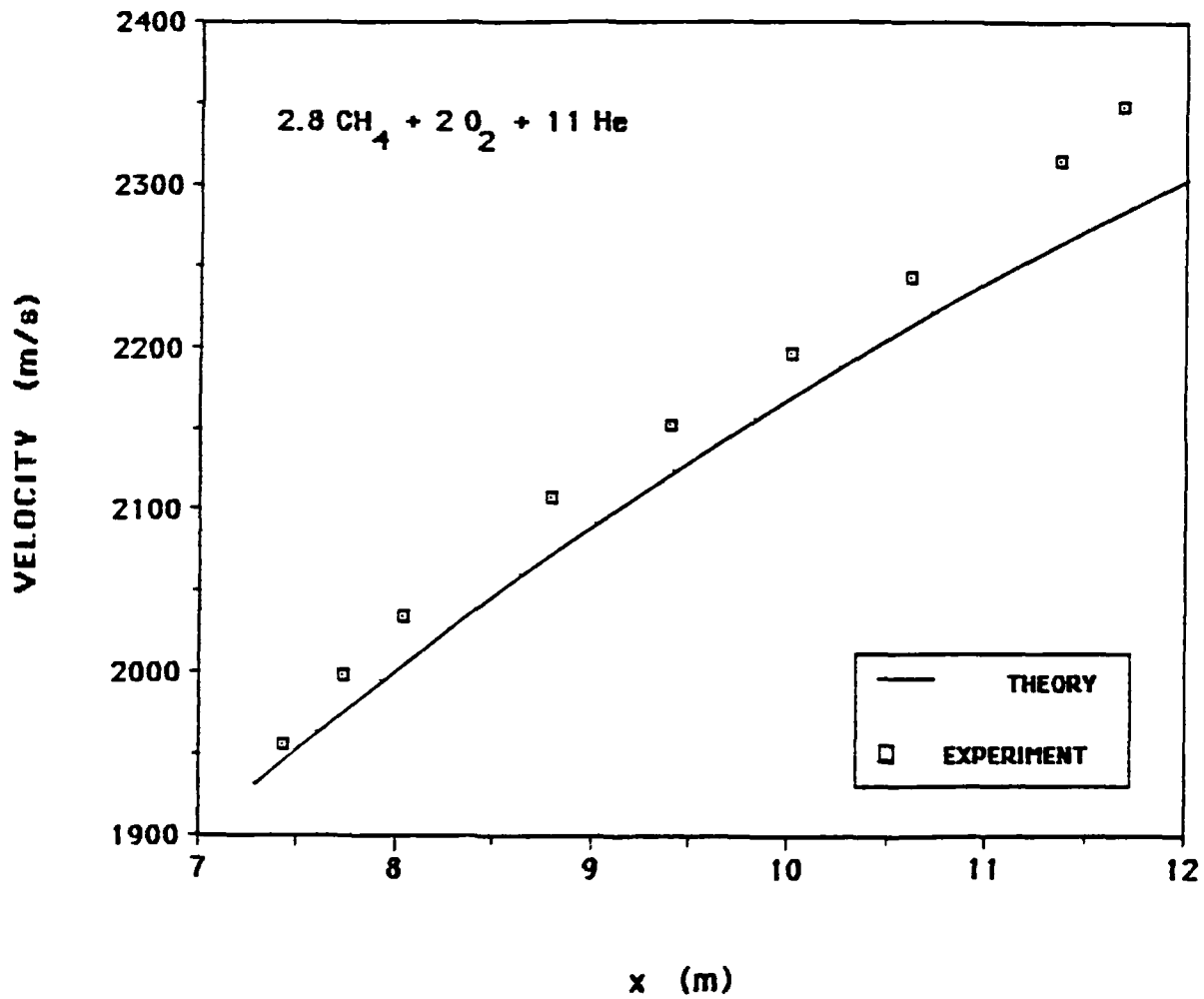


Figure 13. Velocity Profile in Fourth Stage of Four-Stage 11.9 m Ram Accelerator. (Stage entrance velocity = 1980 m/s. Projectile mass = 47gm.)

in the figure. Each of the three stages was 3.66 m long. A peak in-tube velocity of 2130 m/sec was obtained with this configuration. The average acceleration for this 11 m run was ~ 15,000 g's, with a peak value of 30,000 g's. The theoretical curves are normalized to the experimental data at the beginning of each different propellant section of the tube. Since the experimental data diverge somewhat from theory, the experimental and theoretical velocities at the end of each section do not necessarily coincide. This explains the small discontinuities in the theoretical curves in Figure 12. Note, however, that the performance of the projectile predicted by the theoretical model is in close agreement with the experiment throughout the operating range shown.

In Figure 13, the velocity profile is shown in the fourth stage of an experiment with a 47 gm projectile in which the ram accelerator tube was partitioned into four stages, each at 23 atm fill pressure. The stages, their respective lengths, propellant mixtures and transition velocities, are identified in the table below:

TABLE 1. PROPELLANT COMPOSITIONS AND TRANSITION VELOCITIES
IN FOUR-STAGE RAM ACCELERATOR CONFIGURATION

Stage	Length (m)	Propellant	V_{in} (m/sec)	V_{out} (m/sec)
1	1.22	2.6CH ₄ +2O ₂ +5.7N ₂	1235	1386
2	3.66	4.3CH ₄ +2O ₂ +2He	1386	1762
3	2.44	3.4CH ₄ +2O ₂ +6.5He	1762	1990
4	4.57	2.8CH ₄ +2O ₂ +11He	1990	2357

A maximum in-tube velocity of 2357 m/sec and a peak acceleration of 30,000 g's were observed in the fourth segment of this four-stage configuration. The experimental data lie above the theoretical curve with a maximum difference in velocity of less than 4% at the end of the run. This divergency is believed to be due to uncertainties in the experimental

variables and transient behavior associated with unsteady flow effects not included in the analytical model.

It has been observed that additional acceleration occurs in the short evacuated drift tube which follows the ram accelerator. This is shown by the solid, diamond-shaped points plotted to the right of the curves in Figure 10, which were obtained using the shorter accelerator tube. These correspond to the projectile velocity at the end of the drift tube, as measured by the two-beam laser system. The velocity increment ranges from ~20 m/sec to ~60 m/sec, depending on the fill pressure and the velocity range. This acceleration is due to the net forward thrust generated by the high pressure gas which follows the projectile as it exits the ram accelerator tube. Separate investigations of this phenomenon have shown that the bulk of the additional impulse is imparted to the projectile within about 20 tube diameters of the exit diaphragm.

The minimum entrance velocity required with the CO₂ diluted mixture is ~690 m/sec. Below that velocity an unstart condition results, i.e., the shock system is disorged by the projectile, because the diffuser area ratio is too large for the corresponding Mach number and Δq . The mixture using N₂ and excess CH₄ as diluents requires a minimum entrance velocity of ~900 m/sec. Minimum starting velocities for the helium-diluted mixtures are 1300, 1650 and 1900 m/sec, respectively, for dilution by 2 He, 6.5 He and 11 He. When an unstart condition occurs the flow chokes at the throat and the projectile suddenly begins to act like a piston which drives a normal shock and a high pressure slug of gas ahead of itself. This results in rapid deceleration. Figure 14 shows the pressure trace and simultaneous electromagnetic transducer signal for a typical unstart condition. An outline of the projectile is shown in the figure for reference. In this particular case the unstart resulted in a 20 atm mixture of 2.5CH₄ + 20₂ + 5.2N₂ + 2He. The normal shock is propagating ahead of the projectile at a velocity of ~1330 m/sec, and the projectile is moving at ~1000 m/sec. Depending on the particular conditions leading to the unstart, and the nature of the propellant, the normal shock ahead of the projectile can develop into a C-J detonation wave.

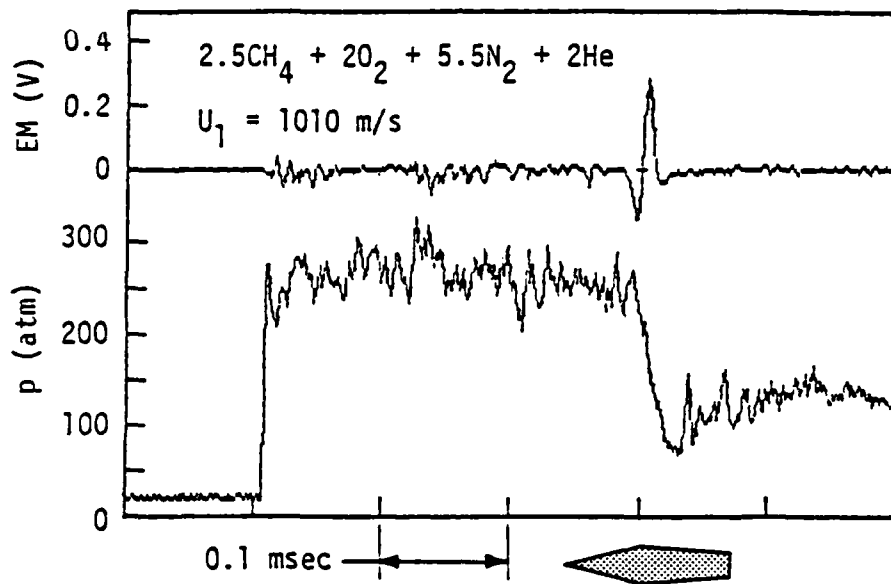


Figure 14. Pressure Signature for a Typical Unstart Condition.
 ($p_1 = 20 \text{ atm.}$)

4. BALLISTIC EFFICIENCY

Figures 15 and 16 show plots of the ballistic efficiency as a function of projectile velocity for several of the propellant mixtures discussed here. The solid/dashed curves represent the theory and the plotted points represent the results for the experiments shown in Figures 12 and 13. The change from solid to dashed line on the theoretical curves marks the point where the 1-D theory predicts that the single normal shock will fall off the rear of the projectile. The dashed part of the curve corresponds to the expected performance of a projectile whose rear body tapers to a point. On such a geometry the normal shock would, in principle, stay on the projectile up to the C-J detonation speed, as discussed earlier. Since the determination of the ballistic efficiency (Equation 6) requires the second derivative of the projectile's x-t history, small errors in time measurements and imperfections in the x-t curve fit to the data are amplified, giving rise to relatively large possible errors. Typical error bars are shown on the leftmost data points of Figures 15 and 16.

The experimentally determined ballistic efficiencies do not exactly follow the theoretical curves, however their magnitudes are generally in agreement over the velocity ranges investigated. Ignition delays, starting transients and/or transition transients are believed to account for some of the observed discrepancies. Such unsteady phenomena are not included in the quasi-steady theoretical model. The adjustments to sudden changes in the flow conditions occur over finite time intervals, whereas the quasi-steady model, in effect, assumes instantaneous response.

In Figure 15 the first and third mixtures exhibit similar variations in ballistic efficiency with increasing velocity. In both cases the experimental data initially show a decrease in efficiency with increasing velocity, as predicted by theory. For the third mixture, the initial correlation with theory is particularly good. It should be noted that in both cases a finite ballistic efficiency is observed at velocities well in excess of the points where theory predicts a single normal shock will move off the rear of the projectile. In the case of the third mixture all the experimental data correspond to velocities above this shock "fall-off" point. This behavior tends to support the earlier hypothesis that the normal shock on the

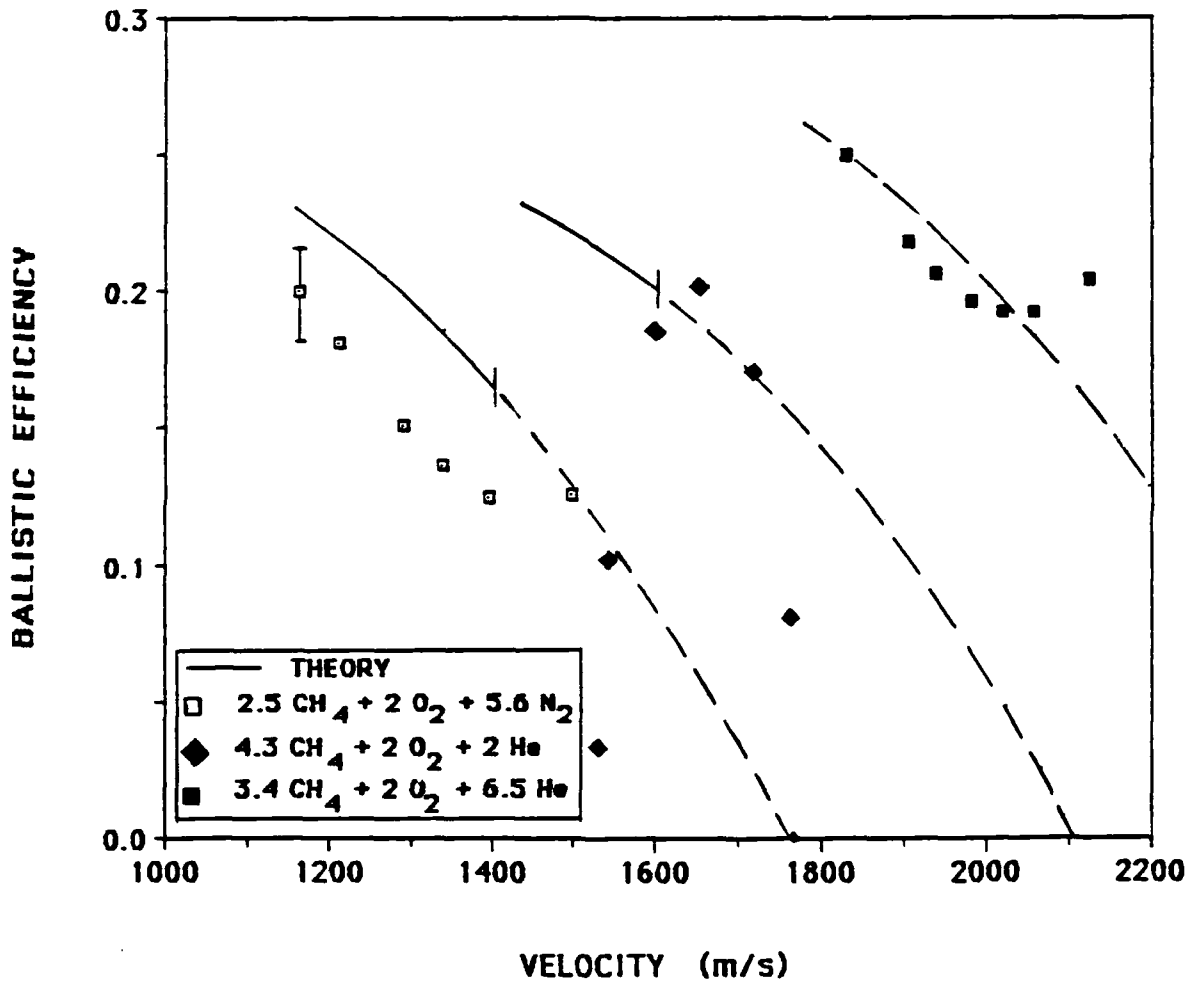


Figure 15. Ballistic Efficiency as a Function of Velocity for Staged Propellant Mixtures Shown in Figure 12.

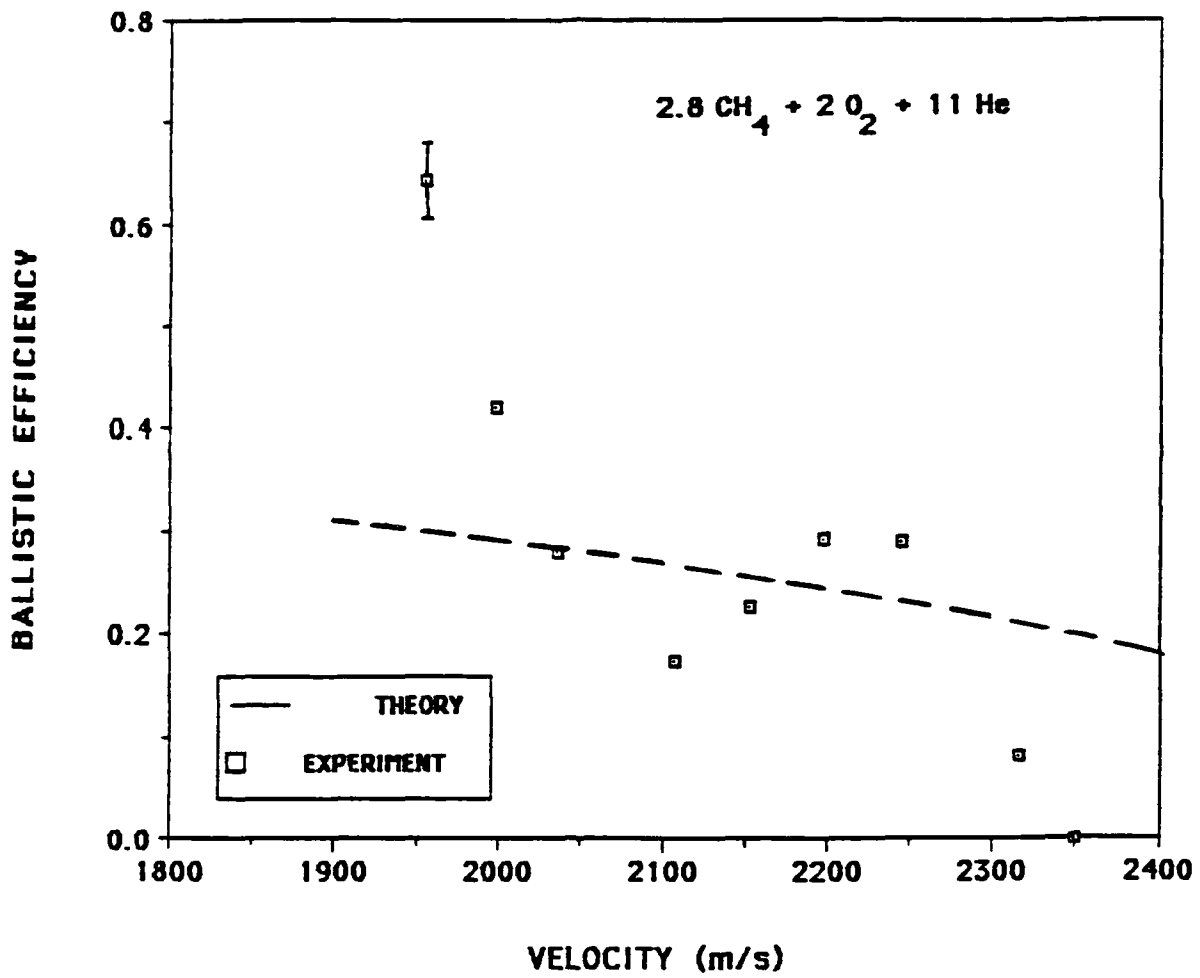


Figure 16. Ballistic Efficiency as a Function of Velocity for Fourth-Stage Propellant Mixture Shown in Figure 13.

projectile actually consists of a complex system of normal and oblique shocks. Such a wave system would stay attached to the projectile at velocities beyond that at which a single normal shock would fall off.

The experimental data for the first and third mixtures in Figure 15 show an upturn as the projectile velocity continues to increase, indicating an increase in thrust. Based on examination of the relevant pressure signatures, it appears that this increase may be a result of the normal shock system moving forward on the projectile. This is a recurring phenomenon that is often seen in the mixtures tested when the projectile is allowed to drive up to its limiting Mach number. This anomalous behavior (i.e., in the context of the quasi-steady model) is believed to be a consequence of unsteady flow effects. One possibility is that a fraction of the available chemical energy is being released in the reduced flow area around the projectile due to either combustion creeping up the boundary layer on the projectile or shock ignition of the flow itself. This phenomenon is currently under investigation.

The second mixture in Figure 15 exhibits behavior that is very different from those of the first and third mixtures. In this case the ballistic efficiency starts off very low, rapidly increases with velocity, and then just as rapidly decays to zero. The initial increase is thought to be a result of a transient induced by the transition from the first mixture. It is believed that the normal shock system fell back to the rear of the projectile and then rapidly moved forward to its "equilibrium" position. The maximum ballistic efficiency corresponds to the point of maximum forward excursion of the shock system on the projectile. The decrease in ballistic efficiency with further increases in velocity is indicative of the shock system moving backwards relative to the projectile.

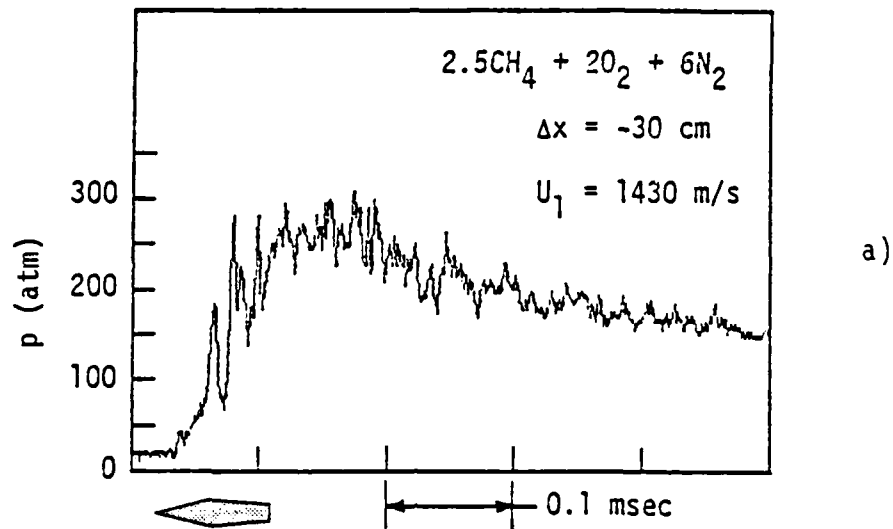
The behavior of the fourth-stage mixture (Figure 16) exhibits characteristics associated with both types of behavior observed in Figure 9. The observed ballistic efficiency is initially about a factor of two greater than that predicted by the quasi-steady analysis. This may indicate that, upon transition from the previous mixture, the normal shock system snapped forward on the projectile, ahead of the expected location. The rapid decrease in ballistic efficiency as the projectile velocity increases may be

a result of the transient readjustment of the shock position on the projectile in response to the flow conditions over the projectile. The subsequent upturn and then downturn in ballistic efficiency with further increases in velocity possibly indicate a back and forth oscillation of the normal shock system on the projectile. Increases in ballistic efficiency tend to correlate with forward excursions of the wave system, and vice-versa. The exact disposition of the wave system on the projectile is difficult to determine because the high speed of the projectile, coupled with the high acoustic speed and relatively low heat capacity of this mixture, results in abrupt rise-times in the pressures, which are too fast for the piezoelectric transducers to follow. The causes of the non-steady behavior may be rooted in phenomena similar to those discussed with respect to Figure 9 or in combustion instabilities. Further research into these effects is clearly required.

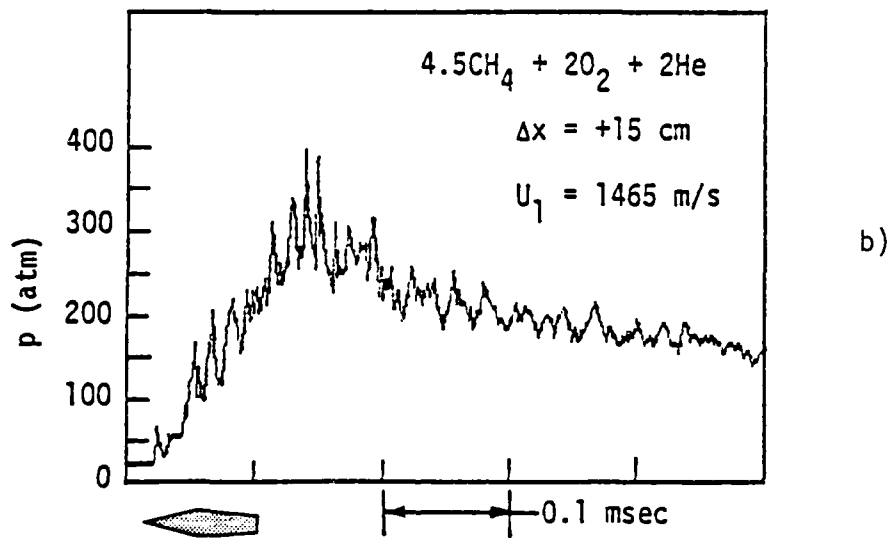
5. TRANSITION BETWEEN MIXTURES

When staged mixtures are used, the transition to a faster mixture, i.e., a mixture whose speed of sound is significantly higher than the previous mixture, involves three key factors. These are the position of the shock on the vehicle at transition, the Mach number in the new mixture, and the heat of combustion of the new mixture. The shock structure observed on the projectile is believed to be a complex wave system consisting of normal and oblique shocks. If this system falls off the projectile prior to the transition point, the wave system in the new mixture does not always re-stabilize on the projectile and may initiate a detonation wave that overtakes the projectile, causing its diffuser to unstart and the thrust to become negative. In a similar manner, if the lead normal shock is too near the throat at the point of transition, it often sweeps upstream of the throat and again unstarts the diffuser. Thus, for a successful transition it has been found that the shock system must be firmly on the projectile, preferably halfway between the throat and the base.

Figure 17 shows two pressure traces obtained in a successful transition between $2.5\text{CH}_4 + 2\text{O}_2 + 6\text{N}_2$ and $4.5\text{CH}_4 + 2\text{O}_2 + 2\text{He}$ at 20 atm. The pressure transducers were respectively located 30 cm ahead of and 15 cm beyond the



a) Before Transition



b) After Transition

Figure 17. Pressure Signatures Before and After Transition from $2.5\text{CH}_4 + 2\text{O}_2 + 6\text{N}_2$ to $4.5\text{CH}_4 + 2\text{O}_2 + 2\text{He}$. ($p_1 = 20 \text{ atm}$. Δx refers to locations of pressure transducers with respect to diaphragm which separates the mixtures.)

mylar diaphragm which separated the mixtures. Note that in both cases the normal shock system is firmly on the projectile. In the faster mixture (He diluted) the driving wave system is farther up on the projectile, as would be expected from the lower Mach number in that mixture. Slight differences in the shapes of the pressure traces are attributable to the sudden change in Mach number experienced by the flow and the different physical properties of the two gas mixtures. Optimum performance would, of course, be obtained using a graded propellant mixture in the launch tube. In this manner the Mach number could be kept approximately constant at a value corresponding to the highest possible ballistic efficiency.

6. THRUST PRESSURE RATIO

The thrust pressure ratio ϕ , plotted for two different propellant mixtures in Figure 18, is computed from Equation 14 using the thrust and peak pressure data. The experimentally determined values of ϕ thus have relatively large uncertainty and significant scatter due to the inherent uncertainty in the values of F noted earlier and the difficulty in accurately determining the peaks of the pressure traces. The difficulty in obtaining accurate pressure data stems from the relatively noisy pressure signatures (see Figure 8). This noise is a result of complex wave interactions and transducer and tube wall resonances. Nevertheless, the trend of the experimental data is clear: the thrust pressure ratio has approximately the expected magnitude at a given velocity and decreases with increasing velocity. At the high velocity end for each propellant mixture the experimental thrust pressure ratio decreases rapidly as a result of the normal shock system falling completely off the rear of the projectile. This result is consistent with the rapid decrease in ballistic efficiency typically observed at similar velocities in these mixtures.

7. VELOCITY LIMITING PHENOMENA

In experiments to date two distinct mechanisms have been observed which have limited the maximum velocity. One of these mechanisms involves the backward motion of the normal shock system relative to the projectile to the extent that the shock system "falls off" the rear of the projectile and the

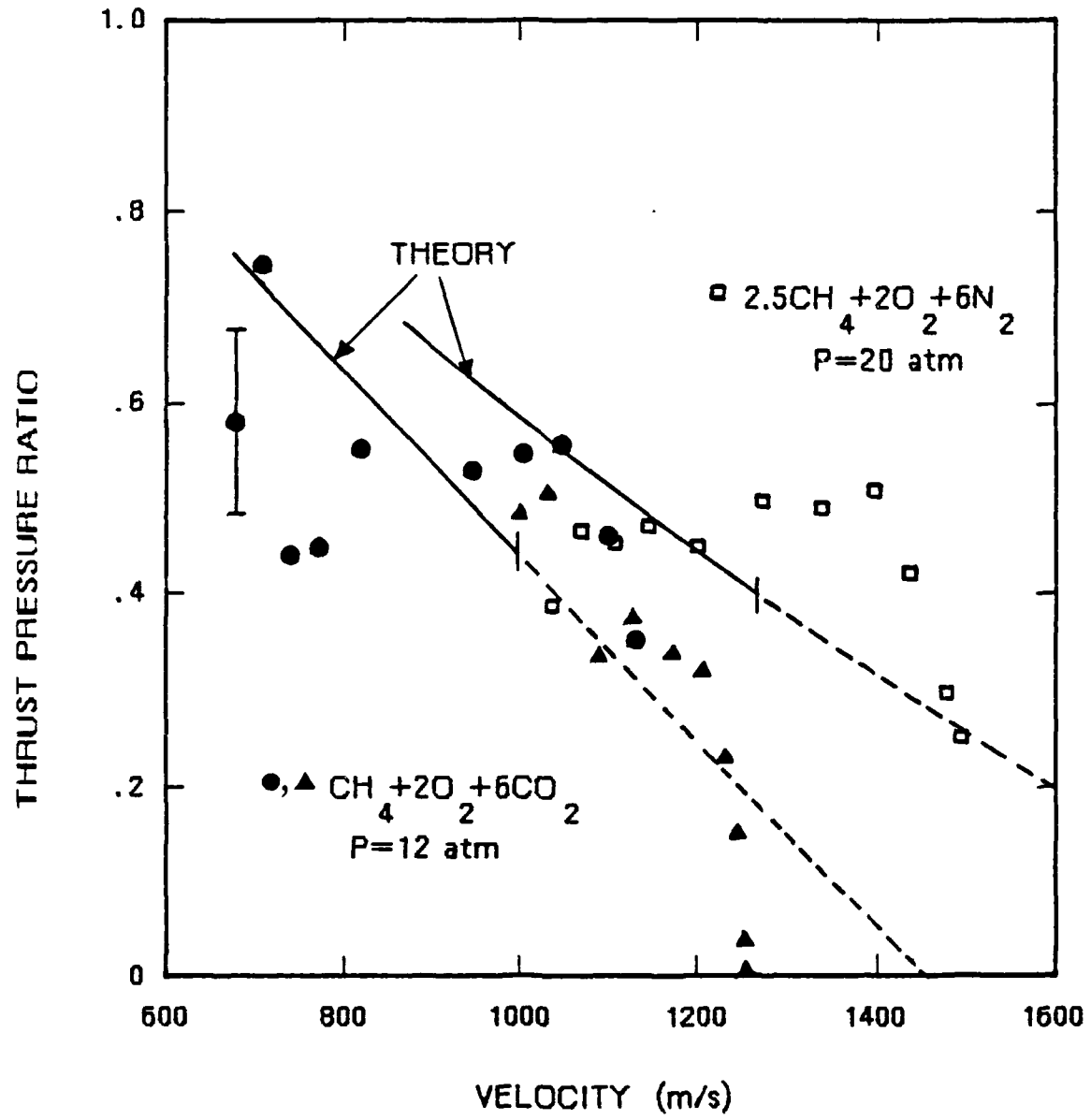


Figure 18. Thrust Pressure Ratio as a Function of Velocity for CO_2 and N_2 Diluted Mixtures.

thrust drops to zero. Figure 19 shows a pressure trace corresponding to the wave system having just fallen off the rear of the projectile. The flow around the projectile is fully supersonic. Typically, the "lost" wave system behind the projectile develops into a detonation wave within ~20 tube diameters of the location where the wave system first falls off the projectile. This detonation then overtakes the projectile, resulting in an unstart condition. The movement of the driving wave system off the projectile as the velocity increases is a gradual process and, as noted above, the thrust and ballistic efficiency remain finite at velocities significantly higher than predicted by the simple quasi-steady analytic model which assumes a single normal shock on the projectile. This effect may be seen in the second mixture in Figure 15 ($4.3\text{CH}_4 + 2\text{O}_2 + 2\text{He}$). The theory predicts that a single normal shock will fall off the rear of the projectile at ~1600 m/sec, whereas the highest velocity prior to transition to the next mixture is ~1770 m/sec. The ideal theoretical limit discussed earlier, i.e., the C-J detonation speed, for this mixture is ~2100 m/sec. Thus, the maximum projectile velocity observed in this case lies between the two limits obtained from the theoretical model.

A rapid forward sweep of the shock system on the projectile, resulting in choking at the throat and a subsequent unstart, is the other velocity limiting mechanism that has been observed. The third-stage mixture in Figure 15 exhibited this particular behavior. The pronounced upturn in the ballistic efficiency is indicative of the forward motion of the shock system. This behavior may be a result of either shock ignition of the gases on the back half of the projectile or of combustion rapidly creeping up a separated boundary layer on the projectile. Typically, the two velocity-limiting mechanisms are observed to occur in the Mach number range of about 4.0 to 4.5, depending on the particular propellant mixture.

Ideally, optimum performance for a projectile having a given throat to tube diameter ratio could be attained using a smoothly graded propellant mixture in the accelerator tube. In this manner the Mach number could be kept constant at a value corresponding to the highest ballistic efficiency and thrust possible for the given configuration. For a prescribed fill

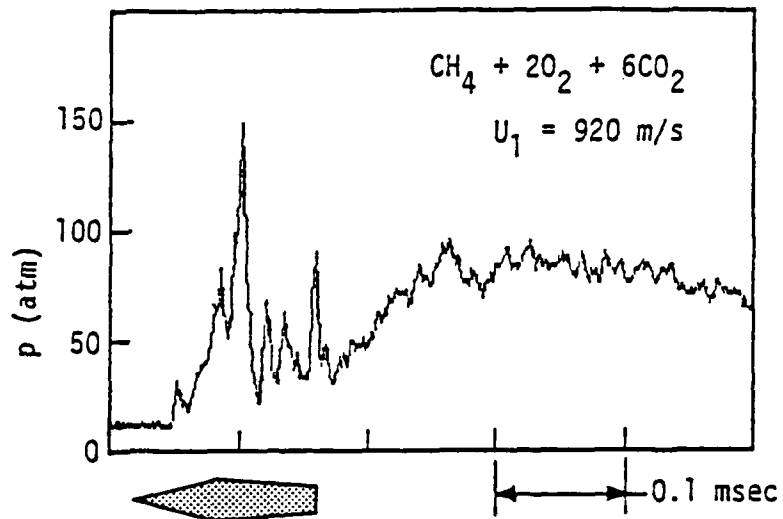


Figure 19. Pressure Signature Showing Typical Shock Wave Fall-off from Projectile. ($p_1 = 20 \text{ atm.}$)

pressure and projectile exit velocity, this approach would result in the shortest possible accelerator tube.

The maximum velocity experimentally attained within the mixtures investigated to date for the nominal projectile geometry is typically about 85% of the C-J velocity (Reference 14). Enhanced performance at near-detonation velocities has been observed for projectiles with a nose half-angle of 10° and a body length extended by 12.7 mm, but nominal throat and base area ratios. For example, the upper velocity limit in the $3.4 \text{ CH}_4 + 20_2 + 6.5 \text{ He}$ mixture for the standard projectile has experimentally been determined to be ~ 2100 m/sec, with a scatter of ± 50 m/sec. The longer projectiles with smaller nose half-angles have repeatedly attained velocities above 2200 m/sec in this mixture; in one case a velocity of 2310 m/sec, or 95% of the C-J detonation velocity, was reached. The observed increases in maximum velocity with the modified projectile geometry are assumed to be due to more efficient supersonic compression, the longer body on which the normal shock system can stabilize, and the increased separation distance between the normal shock system and the recirculation zone at the base of the projectile. Other factors may be the enhanced projectile stability derived from greater fin length and the reduced divergence angle of the flow behind the throat. Where the flow is subsonic with respect to the projectile the lower divergence angle reduces the adverse pressure gradient, thus reducing the tendency of the boundary layer to separate. Investigations into vehicle geometry effects are currently being pursued.

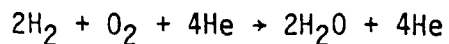
SECTION VI

DETONATION DRIVEN MODES

1. SUMMARY OF 1-D DETONATION DRIVEN MODE THEORY

In this section, the preliminary one-dimensional methods for calculating the performance of the detonation driven ram accelerator modes are described. Oblique shocks are calculated by applying the standard equations of fluid dynamics (continuity equation, momentum equations in two dimensions and energy equation) across the shocks. Oblique detonation waves are computed in a similar manner with a heat addition term included in the energy equation. Flows in the diffuser between the throat and the normal shock are treated isentropically for the overdriven detonation mode. All nozzle flows are treated isentropically. The conditions at the end of the cylindrical section of the projectile for the two oblique detonation modes are made by applying the continuity, momentum and energy equations between this station and the station just downstream of the detonation wave. The calculations for the flow around the projectile are done using an ideal gas equation of state with one set of values of molecular weight and specific heat ratio before combustion and a second set after combustion.

The chemical reactions considered for the oblique detonation modes are relatively simple, for example,



or



Such species as OH, H, CO, etc. are neglected because the qualitative performance of the oblique detonation modes can be sufficiently illustrated without the dissociation effects. The overdriven detonation mode utilizes a more detailed chemical equilibrium computation to account for the

dissociation losses of the high temperature reaction products. Values of specific heat ratio are calculated from differences of JANAF enthalpy data (Reference 15) over estimated cycle temperature ranges and the amount of heat release is determined from the heats of reaction data listed in the JANAF tables. For all three modes, the temperature after compression, but before combustion is limited to a maximum of 900°K. Cycle solutions with higher post-compression temperatures are presumed to be at risk for combustion in the compression process and are therefore rejected as practical cycle solutions. In addition, for the type I oblique detonation mode, valid solutions are required to have temperatures behind the reflected shock (without combustion) exceeding 1100°K so that initiation of the detonation is assured. The actual limiting temperatures are undoubtedly somewhat different than those given above. This does not affect the validity of the detonation driven mode concepts but the operating velocity limits would be somewhat shifted.

The thrust on the projectile for all the detonation driven modes is calculated from the difference in the momentum flux at the front and rear of the projectile. The velocity profile of the in-tube flight of the projectile is determined by numerically integrating the equation of motion (Equation 6). From the thrust, the rate of work done on the projectile can be calculated, and hence η and ϕ obtained.

The results for the overdriven detonation mode include the frictional losses on the supersonic portions of the projectile by assuming values for the skin friction coefficients and correcting them for the local flow Mach numbers and static pressures. The results of the oblique detonation driven modes presented here are without allowance for frictional losses. For the type I oblique detonation mode, some estimates of frictional losses have been made. A somewhat conservative theory was developed using Reynolds' relation between friction and heat transfer, van Driest's (Reference 16) predictions of skin friction coefficients without wall mass transfer and Jeromin's (Reference 17) correlations of experimentally observed reductions of skin friction via wall blowing and application of a heat balance relation at the projectile wall. If ablation or transpiration cooling is neglected for a $2\text{H}_2 + \text{O}_2 + 4\text{He}$ propellant gas, friction is estimated to reduce ϕ and η

by about 25% at 7 km/sec and by about 65% at 11 km/sec. Since the stagnation temperatures are well above 4000°K in the 6-12 km/sec range, ablation will in fact occur or transpiration cooling must be used. Allowing for ablation or transpiration, the performance reductions are somewhat smaller, 20% at 7 km/sec and 45% at 11 km/sec. Performance reductions due to friction of roughly the same magnitude would also be expected for the type II oblique detonation; however, friction calculations have not yet been made for this mode. Frictional losses could be greatly reduced if a pure hydrogen core could be laid down in the tube, surrounded by combustible propellant gas. This concept is discussed later in this section and in Section VII.

2. OVERDRIVEN DETONATION MODE

The projectile shown in Figure 3 is traveling at an in-tube Mach number that is sufficiently high (typically $M_1 \geq 6$) for the normal shock to initiate combustion, which occurs in a very thin layer immediately behind the shock (station 4). The calculations from station 1 to station 2 are done using two-dimensional wedge flow with an incident and a single reflected shock. From station 2 to station 3 the flow is taken to be isentropic. A normal shock analysis is done between station 3 and station 4. From station 4 to station 5 the flow is assumed to adiabatically react in a constant area duct. Finally, calculations at stations 6,7 and 8 are done assuming isentropic flow from station 5 to station 8. The position of the overdriven detonation wave is adjusted iteratively until the Mach number at the rear nozzle throat is unity.

For optimum thrust and efficiency the flow Mach number immediately following the overdriven detonation wave (station 5) should be close to 1, i.e., nearly choked. However, the choking condition, $M_5 = 1$, corresponds to a C-J detonation wave, which is unstable in either a diverging or converging duct. Consequently, the operating parameters are chosen such that M_5 at no time exceeds a value of ~ 0.8 . It should be noted that an overdriven detonation wave is stable in a diverging duct and behaves as an ideal "flame holder" with nearly instantaneous heat release.

3. TYPE I OBLIQUE DETONATION MODE

In the type I oblique detonation mode shown in Figure 4a, the transitions from station 1 to station 2 and from station 2 to station 3 are treated as planar oblique shock waves and detonation waves, respectively, as described earlier. The flow at station 4 is determined by applying the continuity, momentum and energy equations between stations 3 and 4. The nozzle flow from stations 4 and 5 is treated isentropically. Finally, the maximum cycle pressure is calculated just aft of the point where the detonation wave impacts the projectile by calculating conditions after a regular shock reflection or a normal overdriven detonation wave, as appropriate.

4. TYPE II OBLIQUE DETONATION MODE

In the type II oblique detonation mode shown in Figure 4b, the transitions from station 1 to station 2 and from station 2 to station 3 are treated as planar oblique shock waves. From station 3 to station 4 the flow is calculated as an oblique detonation wave. The oblique detonation is assumed to be set off on the projectile body by a small concentric bump or bumps, as described in Section II. Downstream of the detonation wave, the flows are treated as for type I oblique detonation mode. The maximum cycle pressure is calculated essentially as for the type I mode except the maximum pressure occurs at the tube wall, instead of on the projectile.

In principle, the oblique detonation ram accelerator modes can attain velocities up to 12 km/sec using $2\text{H}_2 + \text{O}_2$ mixtures with He or excess H_2 as diluents. However, estimates of heat transfer rates to projectile indicate that in-tube aerodynamic heating and ablation become severe at velocities exceeding ~6 km/sec, the exact velocity depending on the specific propellant composition employed. In order to reduce heat transfer to the projectile and extend the practical velocity limit, the authors have investigated methods of laying down a cylindrical core of pure hydrogen surrounded by the propellant mixture. The kinetic energy density of the gas at 12 km/sec corresponds to the stagnation enthalpy of pure H_2 at 4200°K. JANAF data show this temperature is approximately the point where the sublimation pressure of C_3 (the first species of polycarbon molecules to ablate away

from graphite surfaces) is one atmosphere. This indicates that a graphite walled projectile may be able to traverse the velocity range of 6-12 km/sec in an H_2 core of gas without ablating prohibitively. More energetic combustible gas mixtures such as stoichiometric hydrogen and oxygen can be used outside the hydrogen core because here the energy absorbing diluents are not needed to reduce the flight Mach number and the thermal loading on the projectile. The use of a hydrogen core will also reduce the frictional drag on the projectile. In the type II oblique detonation mode the drag at the initiating bump is reduced by using a hydrogen core because the initial detonation pressure rise occurs away from the projectile and the bump region experiences only the lower pressure jump of the initiating conical shock. However, the lower projectile Mach number in the hydrogen core may require a larger initiating bump or bumps to generate an oblique shock wave strong enough to initiate a detonation in the outer core of gas.

5. RESULTS AND DISCUSSION OF 1-D ANALYSIS

In this section, we discuss the performance of the three detonation driven modes, referring mainly to three gas propellant mixtures. These mixtures are, in order of increasing operating velocity, $2H_2 + O_2 + 2N_2$, $2H_2 + O_2$ and $8H_2 + O_2$. Figure 20 shows curves of thrust pressure ratio versus velocity for the type I oblique detonation mode. These curves are for a representative but non-optimized projectile having a 10° wedge half angle. Each curve has a solid central section and dashed sections extending to higher and lower velocities. Only the solid sections are currently considered to be viable candidates for practical operation. For the low velocity dashed sections, the temperature behind the reflected shock (without combustion) is less than $1100^\circ K$ and reliable detonation is assumed not to be assured. For the high velocity dashed sections, the temperature behind the initial shock is above $900^\circ K$, and such solutions are considered to be at risk for detonation on the initial shock.

Transition between gas mixtures is necessary when one is outside the acceptable temperature limits, as discussed above for the type I oblique detonation mode. For the remaining detonation driven modes, there is assumed to be only the upper temperature limit, i.e., the temperature at the

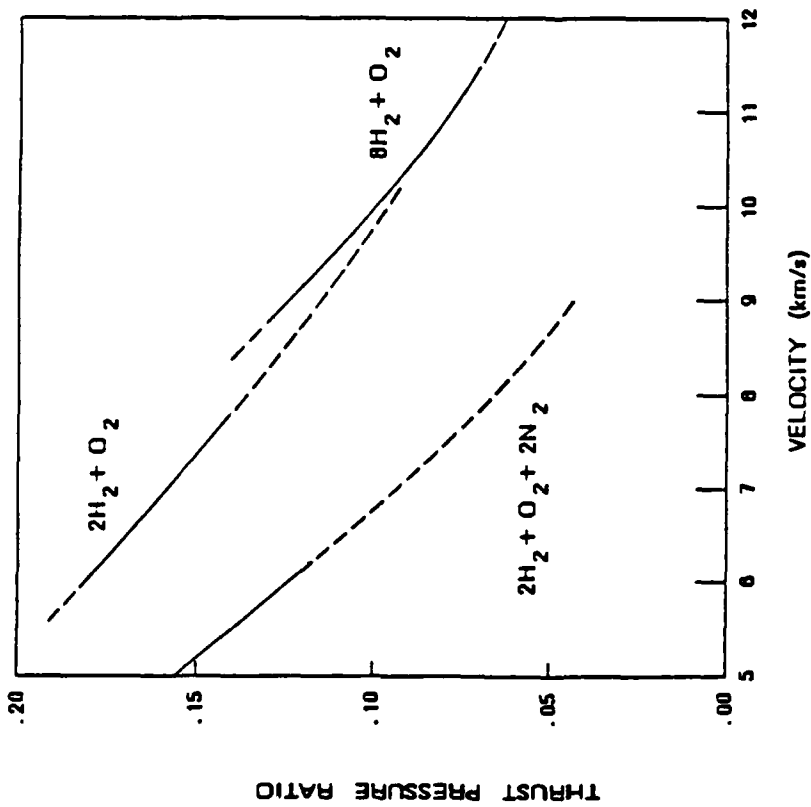


Figure 20. Thrust Pressure Ratio as a Function of Projectile Velocity for Type I Oblique Detonation Mode. (Solid and dashed lines are explained in text.)

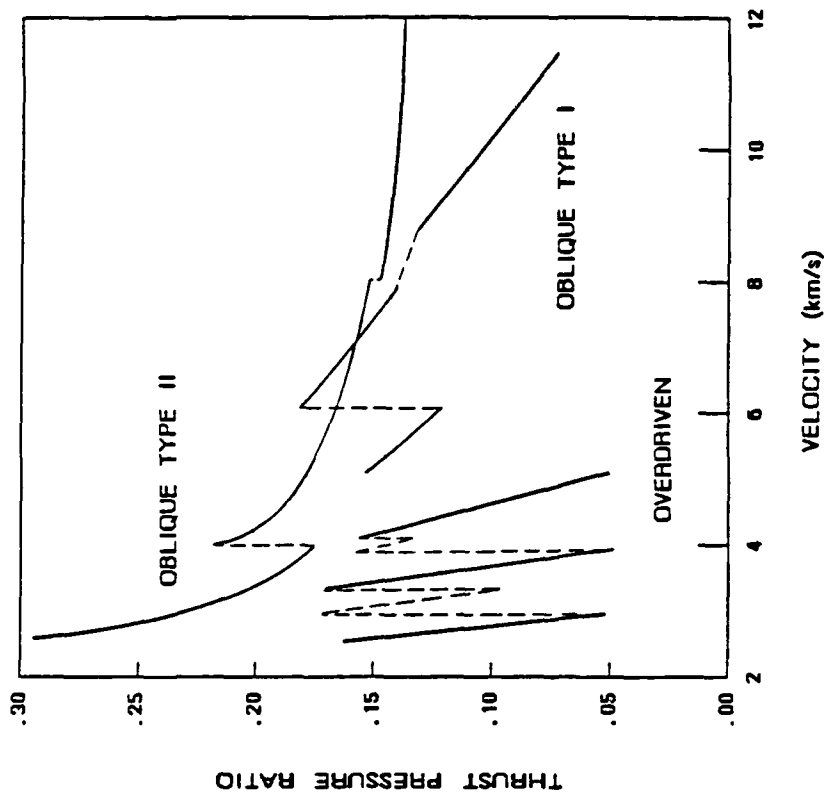


Figure 21. Thrust Pressure Ratio as a Function of Projectile Velocity for the Three Detonation Driven Modes Using the Same Propellant Mixtures Shown in Figure 20. (Solid and dashed lines are explained in text.)

end of the compression process is not permitted to become high enough to place the modes at risk for combustion at this point. Even if temperature limitations are not exceeded, it is desirable to transition between mixtures if one wishes to maximize the overall average thrust pressure ratio or ballistic efficiency.

Figure 21 shows the thrust pressure ratios for all three detonation driven modes. Again, the curves are for representative, but not optimized, projectile geometries. Transitions between gases have been made when temperature limitations have been exceeded and to maximize the thrust pressure ratio. Figure 22 shows the corresponding ballistic efficiency data. For each mode, the solid sections of the curves are for the three propellant gases mentioned earlier, in order of increasing velocity. For the type II oblique detonation mode, it is not necessary to introduce any additional propellant gases to cover the full velocity range. For the type I oblique detonation mode, it is necessary to introduce one additional propellant gas (shown dashed) at ~ 8.5 km/sec to bridge the gap between $2\text{H}_2 + \text{O}_2$ and $8\text{H}_2 + \text{O}_2$. For the overdriven detonation mode, it is necessary to introduce two additional propellant gases at ~ 3.2 and ~ 4.2 km/sec to keep the thrust pressure ratio above 0.05. This illustrates a disadvantage of the overdriven detonation mode, i.e., a considerably larger number of propellant gases is required to span a given velocity range, if the thrust pressure ratio is to be kept reasonably high.

The overdriven detonation mode is limited to velocities below 5 km/sec. The type II oblique detonation mode has a considerably lower low speed velocity limit (2.6 km/sec) than the type I oblique detonation mode (5.0 km/sec) for the N_2 diluted mixture shown. The type II mode, therefore, has a considerably wider overall velocity range. The thrust pressure ratios of the type II oblique detonation mode are higher than those of the type I oblique detonation in all parts of their common velocity range, except for a small region in the range 6-7 km/sec. The thrust pressure ratio of the type II oblique detonation mode is considerably higher than those of the overdriven detonation mode in their common velocity range (~ 0.20 versus 0.10-0.12). The efficiencies of the overdriven detonation and type II oblique detonation modes are mostly in the range 0.10-0.15. The efficiency

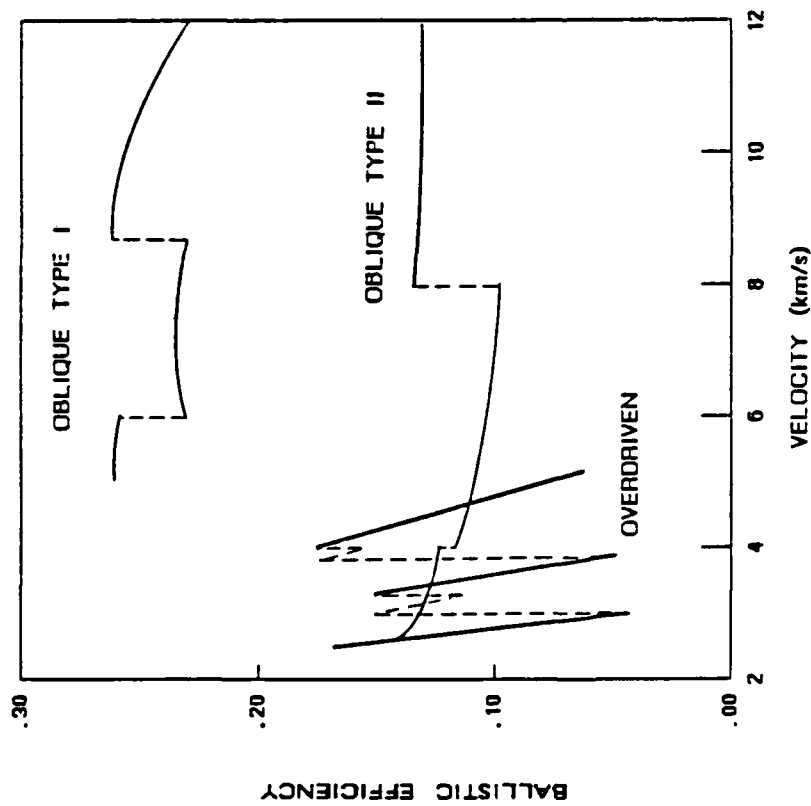


Figure 22. Ballistic Efficiency as a Function of Projectile Velocity Using the Same Propellant Mixtures and Detonation Driven Modes shown in Figure 21.

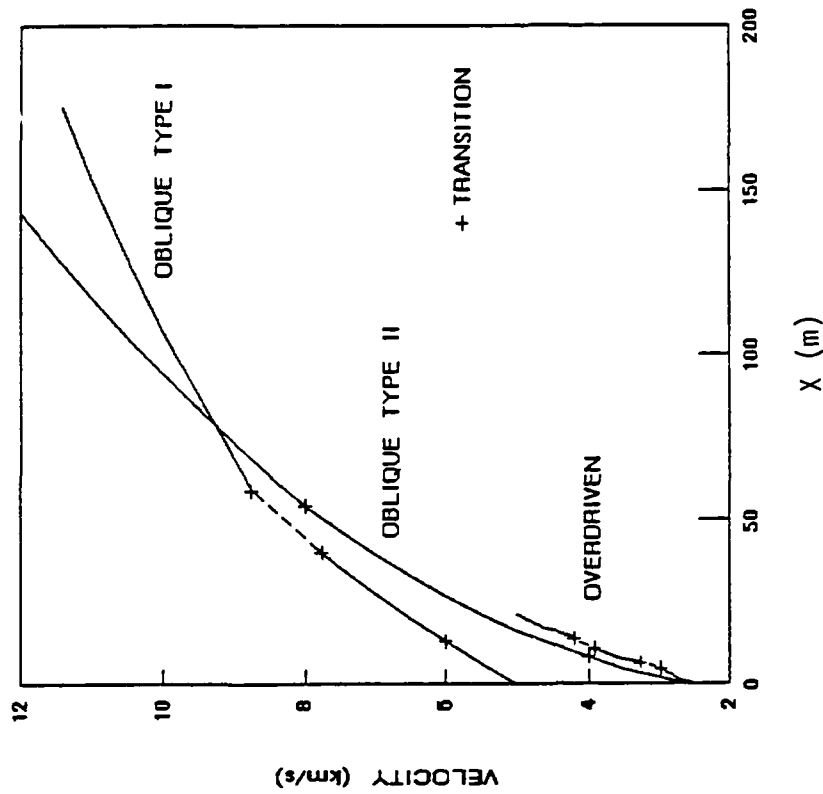


Figure 23. Theoretical Velocity Profiles for the Three Detonation Driven Modes Operating for the Conditions Shown in Figures 21 and 22. (The projectile mass is 1 kg, projectile diameter is 7.7 cm and the maximum cycle pressure is 7000 atm. Crosses indicate transition points and dashed lines represent velocity profiles of the additional propellant mixtures required to fill in the velocity ranges of the overdriven and Type I oblique detonation modes.)

of the type I oblique detonation mode is considerably higher, about 0.25. This higher efficiency is, however, obtained at a cost of somewhat lower thrust pressure ratio (compared to the type II oblique detonation mode), as discussed above.

The performance predictions for the type I oblique detonation mode using the present model have been compared with those obtained using an inviscid axisymmetric, non-steady, non-ideal gas CFD (computational fluid dynamics) code (see Section VII). There are some differences between the models (Table 2) such that exact correspondence between the results is not expected. Despite these modeling differences, the agreement between the present model and the CFD results is fairly good. For example, for the three propellant gases $2H_2 + O_2 + 2N_2$, $2H_2 + O_2$ and $8H_2 + O_2$, the present model predicts maximum thrust pressure ratios of 0.16, 0.18, and 0.13, respectively. The corresponding CFD results are 0.10, 0.18 and 0.12. The present model predicts peak ballistic efficiencies of 0.26, 0.23 and 0.26 for the three propellant gases in order; the CFD predicted values are 0.18, 0.21 and 0.26. The CFD results predict a somewhat lower and wider operating velocity range than the present model. For example for $2H_2 + O_2$, the present model predicts an operating velocity range of 6 to 8 km/sec, while

TABLE 2. COMPARISON OF 1-D AND CFD MODELS FOR THE TYPE I OBLIQUE DETONATION MODE

<u>Present Model</u>	<u>CFD Model</u>
2D planar flow	Axisymmetric flow
Constant γ and m before and after combustion	Enthalpies from JANAF table data
Detonation must occur on second shock, no Mach reflected detonations can be modeled	Detonation can occur on second or third shock, Mach reflected detonations are modeled as required
No expansion fan pressure drops modeled in nozzle	Expansion fan pressure drops properly modeled in nozzle
Detonation wave hits projectile exactly on shoulder	Detonation wave can hit projectile anywhere, as the flow determines

the CFD results predict an operating range of 4 to 7 km/sec. The lower low speed operating limit for the CFD results is largely due to the fact that the CFD code can model detonation on the third or fourth reflection of the initial shock and Mach reflected detonations, and the present model cannot.

Figure 23 shows velocity-distance curves for the three different detonation driven modes for a one kilogram projectile with a diameter of 7.7 cm. The inner diameters of the ram accelerator tubes were 10 cm, 8.4 cm and 12.2 cm for the overdriven, type I oblique and type II oblique detonation driven modes, respectively. The maximum cycle pressure has been taken to be 7000 atm for all cases which in turn limits the tube fill pressures in the series of segments of the ram accelerator to 73 atm, 64 atm and 85 atm for the overdriven detonation case. The type I oblique detonation mode requires a sequence of tube fill pressures of 76 atm, 52 atm and 79 atm. The type II oblique detonation mode requires a sequence of tube fill pressures of 97 atm, 67 atm and 138 atm. The crosses designate transitions between the propellant gases indicated in Figures 21 and 22. Dashed lines represent operation in gases other than the three main propellant gases, as required to bridge the operating velocity gaps discussed earlier. The type II oblique detonation mode requires less distance than the type I oblique detonation mode to achieve the same velocity change. This is because the higher thrust pressure ratio for the former mode allows higher tube fill pressures to be used for greater thrust.

The detonation driven modes can span the velocity range from ~2 to ~12 km/sec. To reach the low speed limit of ~2 km/sec, special mixtures using, for example, CO₂ as diluent would be required. Such mixtures were not included in Figures 21 through 23 in the interest of brevity and clarity. Operation in the higher velocity range of 6-12 km/sec will likely require the use of ablative or transpiration cooling of the vehicle or the use of a hydrogen core in the tube, as discussed earlier.

SECTION VII

CFD MODELING OF OBLIQUE DETONATION MODES

The computational method used in the CFD modeling of the oblique detonation modes is described briefly below. Additional details are given in Appendix C and Reference 18. The code is two-dimensional, axisymmetric and can be divided in the radial direction into multiple zones containing different media. The gridding can slide in the radial direction to preserve the integrity of the media of the zones. The governing equations are the two-dimensional Euler equations, written in conservation form. The code uses the finite volume technique; the state variables are calculated at the center of each computational cell.

The fluxes at the cell boundaries are calculated from values of the primitive variables on the two sides of the boundary. The cell boundary values are obtained by third order extrapolation and/or interpolation from the cell center values. Limiting techniques are applied to maintain the stability and accuracy of the solutions. With primitive variables on both sides of the cell boundary determined, the fluxes are calculated using first and second order Godunov procedures. To advance the code in time, an explicit MacCormack predictor-corrector differencing scheme (Reference 19) is employed which is second-order accurate in time.

A gas equation of state is used which is perfect volumetrically and takes $e = \int C_v dT$ from the JANAF tables (Reference 15), where e denotes internal energy, C_v denotes specific heat at constant volume and T denotes temperature. Combustion is modeled with a single global Arrhenius expression for reactants \rightarrow products. The products include all major mass fraction species with fixed mass fractions determined from separate equilibrium combustion calculations.

All results presented in the following section are obtained from converged, steady-state solutions. It is recognized that in applications, the projectile will be accelerating, and thus true operational solutions would not be exactly steady-state. However, our solutions typically converge in the time it would take the projectile to move two or three projectile

lengths. In typical operational scenarios, the e-folding length for the projectile velocity is 100 to 1000 projectile lengths. Hence, in the time it takes the solution to converge, the projectile velocity would typically change on the order of 1%. Therefore, the results presented here should be very close approximations to results including representative operational accelerations. Solutions including acceleration, if carried out over significant velocity changes, would take 10 or more times the computational times required for the steady-state solutions presented here, and hence have not been done to date.

1. TYPE I OBLIQUE DETONATION MODE

In the type I detonation mode the projectile is injected into a tube section at a speed higher than the detonation speed of the surrounding gas mixture. Flow parameters are chosen so that the first or second reflection of the conical nose shock initiates combustion (Figure 24). A detonation wave develops at the reflected shock front where combustion occurs in a thin layer. The heated gas expands through the nozzle formed by the projectile rear and tube wall, producing thrust.

The following gas mixtures, at an initial temperature of 300° Kelvin and pressure of 100 atmospheres, were investigated:

TABLE 3. GAS MIXTURES INVESTIGATED

<u>Mixture Number</u>	<u>Mixture Composition</u>
1	$8\text{H}_2 + \text{O}_2$
2	$2\text{H}_2 + \text{O}_2 + 3.48\text{CO}_2$
3	$2\text{H}_2 + \text{O}_2 + 2\text{N}_2$
4	$2\text{H}_2 + \text{O}_2 + 6\text{N}_2$
5	$2\text{H}_2 + \text{O}_2$

The projectile shape studied consisted of a conical nose section, a cylindrical center section and a conical tail section (Figure 24). The

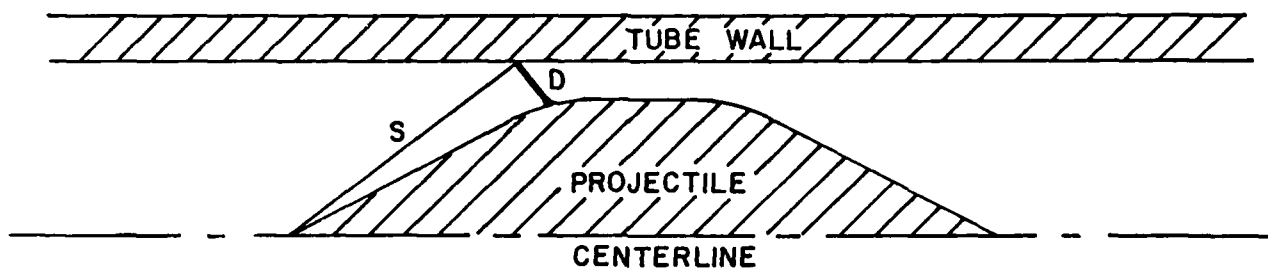


Figure 24. Oblique Detonation Type I Geometry Used in CFD Studies. (S denotes nose cone shock wave and D denotes oblique detonation wave.)

transitions from nose to center section and from center section to tail were faired with parabolic curves. Performance surveys were conducted to optimize the projectile-to-tube wall radius ratio, using a fixed tube radius of 1.5 centimeters and nose and tail half angles of 14° . The tube radius was somewhat arbitrarily chosen, but is reasonable for a laboratory device. In the surveys, the projectile length was held constant at 14.7 cm; as the maximum projectile radius is varied, the length of the center section also varies, since the nose and tail angles are kept constant. These surveys were done at a projectile velocity of 7.0 km/sec in mixture 1, based on the previous one-dimensional calculations of oblique detonation mode performance. The optimal ratio of tube radius to projectile radius was determined to be 1.16 cm. This optimum was selected to maximize the thrust pressure ratio.

The velocity operating envelope was then determined by varying the velocity of the projectile. For the coarse grid 54 by 4 cells were used and for the fine grid 162 by 12 cells were used. Most survey cases were run for 300 time steps on the coarse grid and an additional 200 time steps on the refined grid. Each case required about 30 hours of CPU time on a DEC MicroVAX II computer.

The projectile velocity was reduced until no combustion occurred due to insufficient heating of the mixture through the shock waves. The lower operating limit for mixture 1 was 6.25 km/sec. A case at 5.5 km/sec resulted in no combustion and negative thrust. At 6.25 km/sec, combustion stabilized at the second reflection of the initial conical shock wave, degrading performance. The upper velocity limit for mixture 1 was 9.0 km/sec. At 10.0 km/sec the leading shock wave strength was sufficient to initiate combustion prematurely, subjecting the projectile nose to high pressure and resulting in negative thrust.

Similar surveys were done for the other four gas mixtures. Figure 25 shows curves of thrust pressure ratio versus projectile velocity for all five gas mixtures. Figure 26 shows the corresponding efficiency curves. For mixture 1 it is evident that the optimal operating velocity is near 7.0 km/sec, having a thrust pressure ratio of 0.12 and an efficiency of 0.26. Three important results can be obtained from Figures 25 and 26.

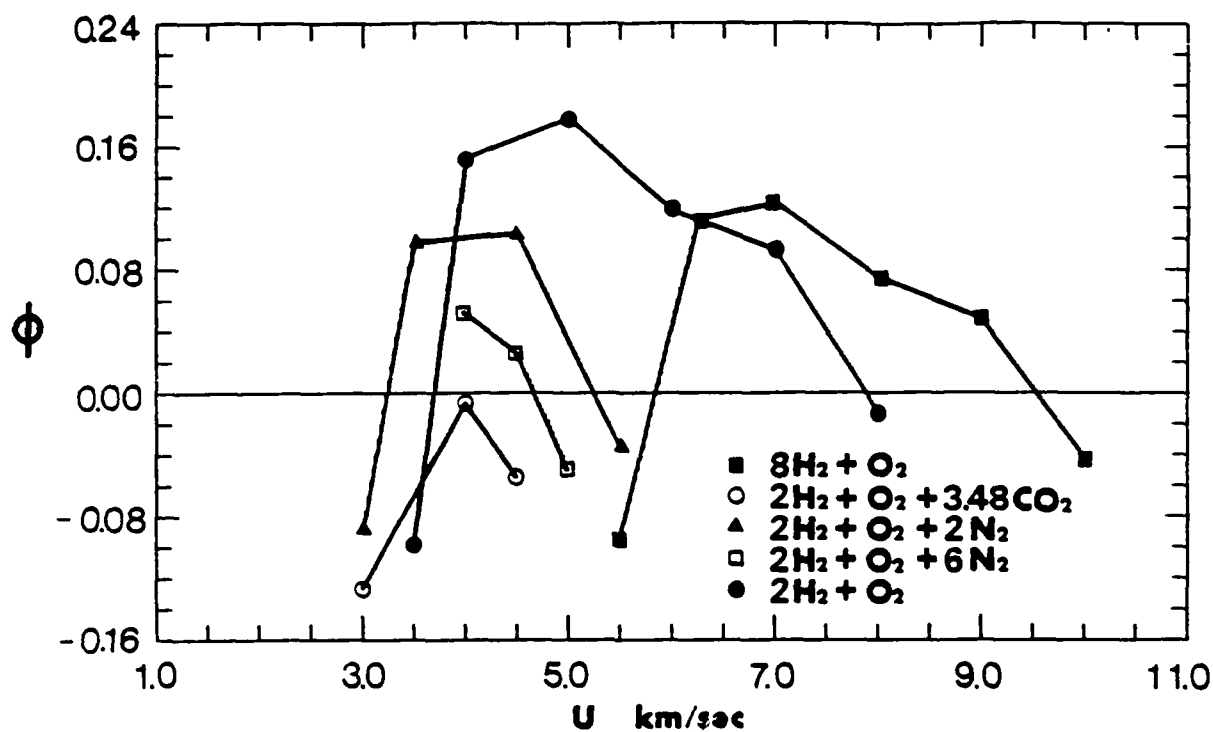


Figure 25. Oblique Detonation Type I Thrust Pressure Ratio Versus Velocity.

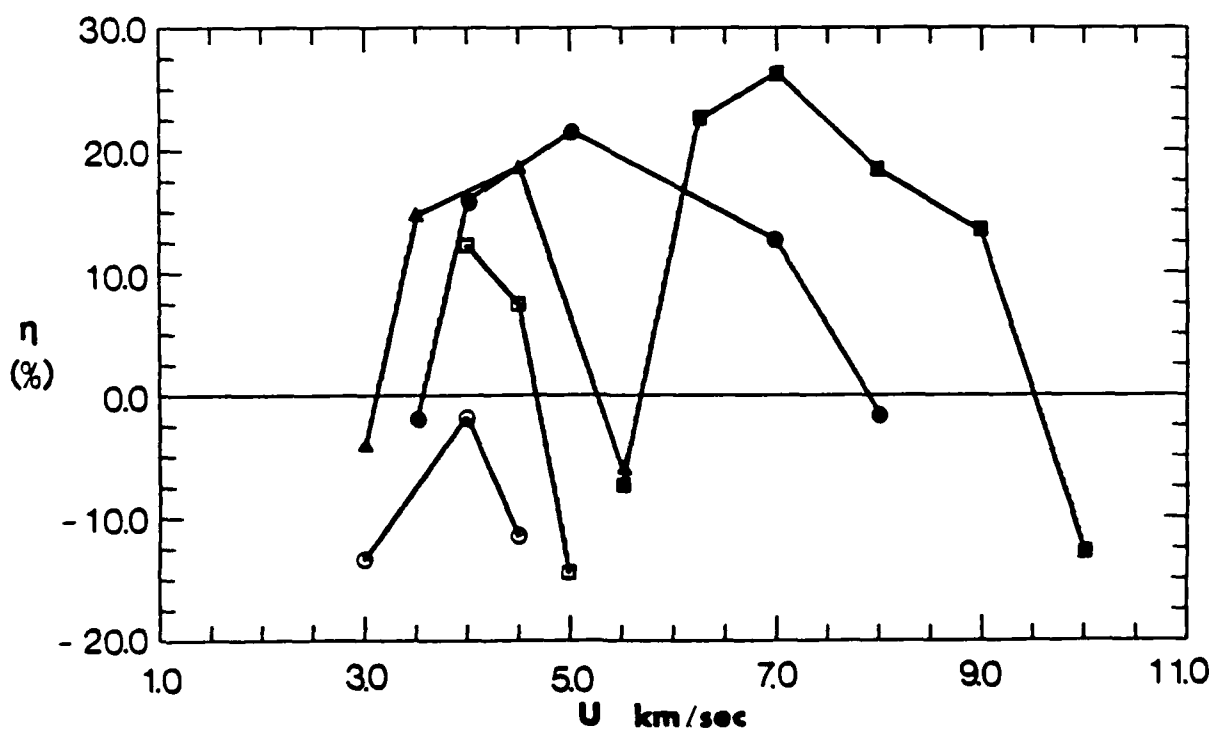


Figure 26. Oblique Detonation Type I Ballistic Efficiency Versus Velocity. (Gas mixtures are same as in Figure 25.)

First, the velocity range of operation of a projectile can be extended by changing the molecular weight of the diluent gas. The operating range of the projectile can be increased from 6.25-9.0 km/sec to 3.5-9.0 km/sec by using nitrogen as a diluent at the lower velocities. Second, if there is too much diluent (e.g., mixture 4), the mixture becomes very weak and low thrust pressure ratios and efficiencies are obtained. The minimum amount of diluent should therefore be used, consistent with the desired velocity range. Third, lower specific heat ratio diluents (e.g., mixture 2), produce lower or negative thrust pressure ratios and efficiencies. The present CFD results bear out the one-dimensional computational studies described in Section VI of this report.

Graphical code results were generated using a standard contour plotting package. Figure 27 illustrates the pressure contours around the projectile moving at 7.0 km/sec in mixture 1. Note that only the outer one-third of the flow field is shown. The nose of the projectile is therefore well to the left of the $x = 0$ point. Going from left to right in the flow field, we see the nose cone shock, the reflected oblique detonation wave impinging on the projectile at the forward projectile shoulder, a series of reflections of shocks and expansions waves of decreasing strength over the center section of the projectile and finally, the expansion wave system over the tail of the projectile.

2. TYPE II OBLIQUE DETONATION MODE

In the type II oblique detonation mode combustion is initiated in a different manner. Whereas careful flow parameter "tuning" is necessary for successful ignition in the type I mode, the onset of combustion is "forced" in the type II mode by the insertion of a steeply sloped ramp in the projectile profile at the location where ignition is desired (Figures 28 and 29). The resulting sharp compression of the combustible gas produces a detonation wave which is stationary with respect to the projectile. The ramp may be split into discrete bumps spaced azimuthally around the projectile body to reduce the drag penalty on the forward slopes of the bumps. Since our code is axisymmetric, the ramp has to be axisymmetric extending completely around the projectile. The drag on the forward facing

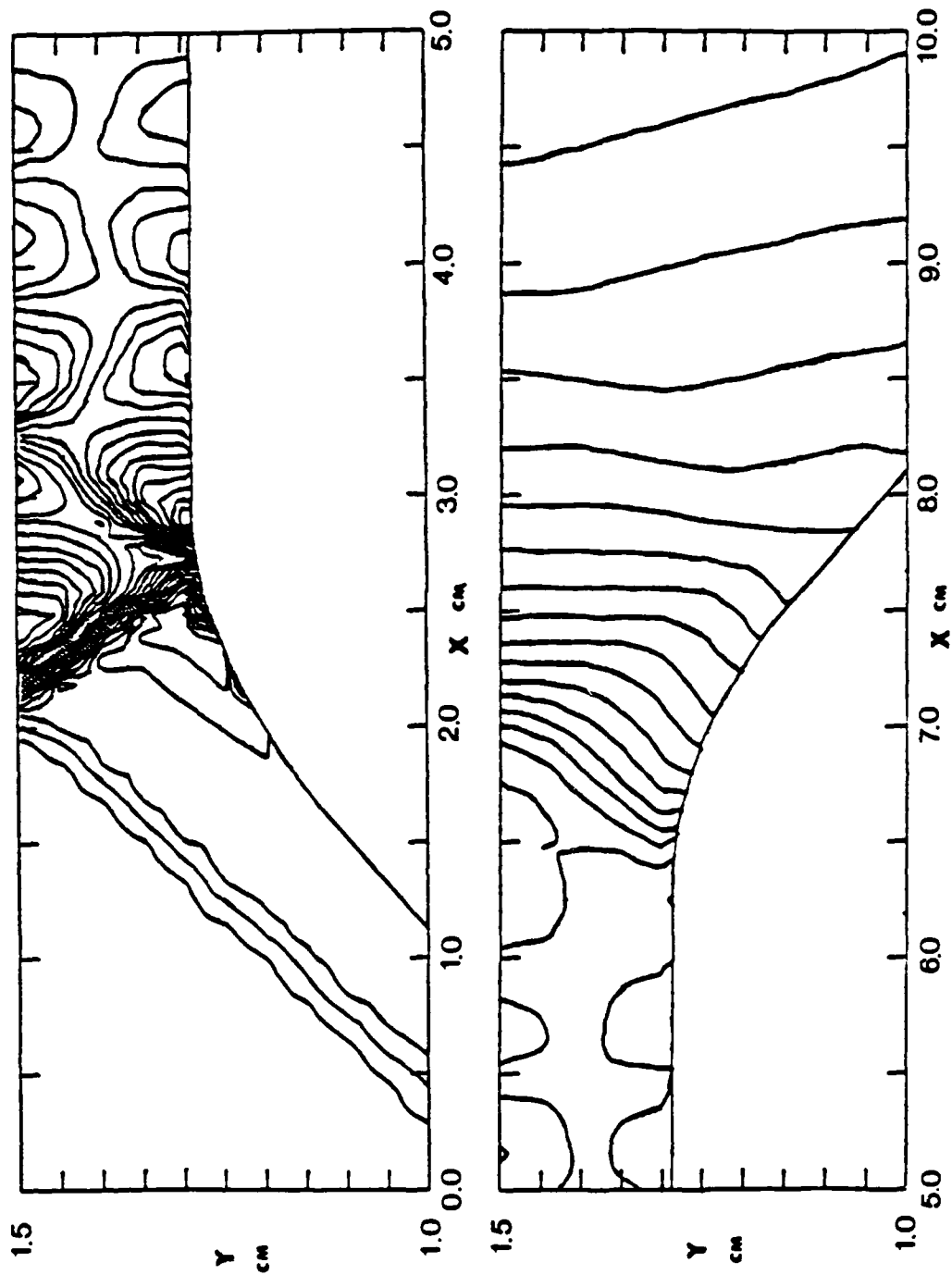


Figure 27. Pressure Contours Surrounding Oblique Detonation Type I Projectile Moving at 7.0 km/s in Mixture 1 ($8H_2 + O_2$). (The maximum pressure contour is 5.6×10^9 dyne/cm². The Y-scale is exaggerated 3.51 times.)

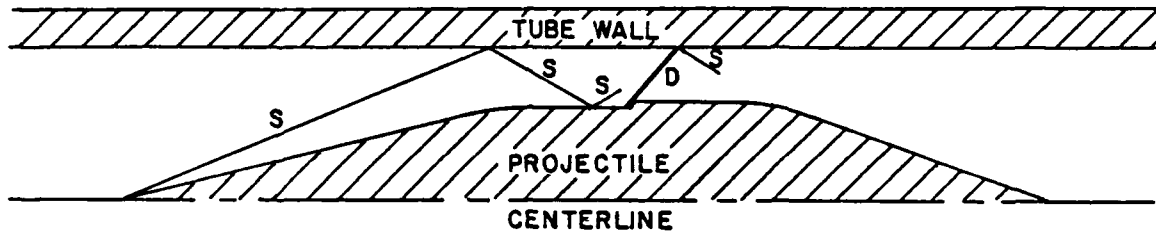


Figure 28. Oblique Detonation Type II Mode Geometry Used in CFD Studies

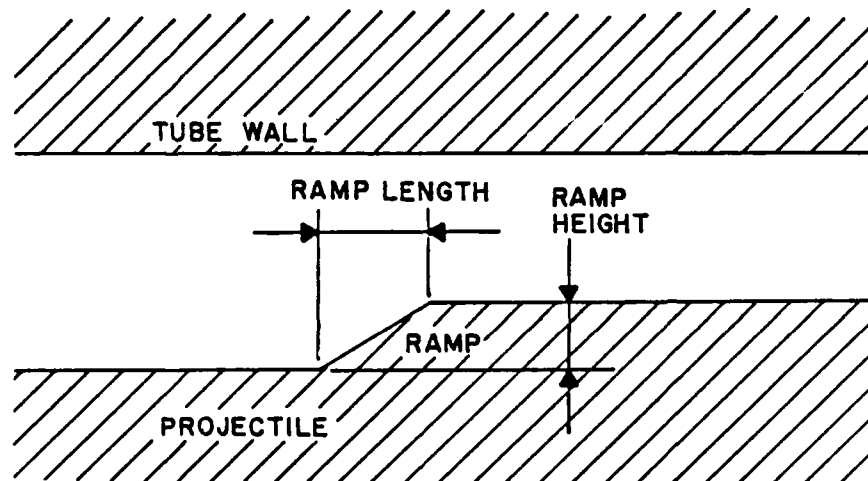


Figure 29. Magnified View of Ramp in Type II Oblique Detonation Mode. (Ramp length and height are shown. The ramp size is exaggerated when compared to the projectile-tube wall spacing.)

surfaces of the ramp will degrade the performance more than if discrete bumps were used. Therefore, we calculated two sets of thrust pressure ratio and cycle efficiency values for each case studied. One set includes the effect of the additional drag on the initiation ramp while the other ignores it. Thus, the values for the corresponding discrete bump configuration are bracketed. Also, for the type II oblique detonation mode calculations, thrust pressure ratios were calculated based on the maximum pressure exerted on the projectile, excluding tube wall pressures. Maintaining projectile integrity under sustained high pressure loading is necessary, of course. Although the tube wall may experience higher pressures, even in excess of its yield stress, the duration of the loading can be made short enough that the material does not deform sufficiently to yield. Using the barrel in this mode permits higher operating pressures, proportionately reducing the barrel length required to achieve a given velocity.

Most type II test cases were run for 300 time steps on a coarse grid and required an additional 500 time steps on the refined grid to reach solution convergence. About 75 hours of CPU time on a DEC MicroVAX II computer were required to complete each of these cases.

As in the type I oblique detonation studies, we ran type II projectile geometry optimization tests at 7.0 km/sec in mixture 1. Because nose shock strength was no longer critical in the ignition process, a more slender nose cone half angle of 7° was chosen to extend the high speed predetonation velocity limit beyond that of the type I mode. A rear cone angle of 10° was chosen to limit the flow expansion rate. If the rear cone angle is too large, the expansion wave system on the rear of the projectile can cause the pressures on the rear cone to drop so low that the thrust is severely degraded. Also, if the angles are larger still, code failure can occur when densities and internal energies attempt to go to zero in the expansion wave system.

It was found that with a ramp length of 0.135 cm, a ramp height of 0.04 cm (Figure 29) was the minimum necessary to initiate combustion reliably at this velocity. The maximum tube-to-projectile radius ratio for the optimized projectile (with respect to thrust pressure ratio and efficiency) was 1.5 for the type II mode versus 1.16 for the type I mode.

The smaller value was chosen because higher thrust pressure ratios were obtained while maintaining satisfactory cycle efficiency. Performance parameters proved to be very sensitive to projectile length and ramp placement. If the ramp is considerably upstream of the point where the reflection of the nose cone shock intersects the projectile surface, the gas impinging on the ramp is relatively expanded and cool, and ignition is very difficult. On the other hand, by placing the ramp somewhat downstream of the point where the reflection of the nose shock intersects the projectile surface, the gas impinging on the ramp is relatively compressed and hot, making ignition much easier.

In the region downstream of the detonation wave, the location of the reflected wave pattern relative to the projectile surface proved to be very important. Thrust is only developed when high pressures occur on the tail of the projectile. Highest thrusts are obtained when a reflection of the oblique detonation wave impinges on the projectile in the neighborhood of, but somewhat downstream of, the rear shoulder of the projectile. Large differential thrust elements are then produced on the upstream part of the tail which, of course, carries the majority of the possible thrust producing area. If the wave system is disposed with respect to the projectile so that this critical part of the projectile tail is in a relatively low pressure, expansion region, the projectile performance is much poorer. The exact disposition of the wave system varies, of course, with projectile velocity, but, as will be shown, a properly designed projectile does have a substantial range of operating velocities in a given gas mixture.

Figure 30 illustrates the pressure wave pattern surrounding a 22.5 cm projectile traveling at 8.0 km/sec in mixture 1. In Figure 30 we can see the nose cone shock, followed by the expansion wave emanating from the front shoulder of the projectile. The nose cone shock reflects from the tube wall and impinges on the projectile somewhat upstream of the ramp. The ramp initiates the oblique detonation wave, which then reflects as a shock from the tube wall and impinges on the projectile near the rear shoulder. The expansion flow over the projectile tail is complicated by two further reflections of the oblique detonation wave shocks and the expansion wave

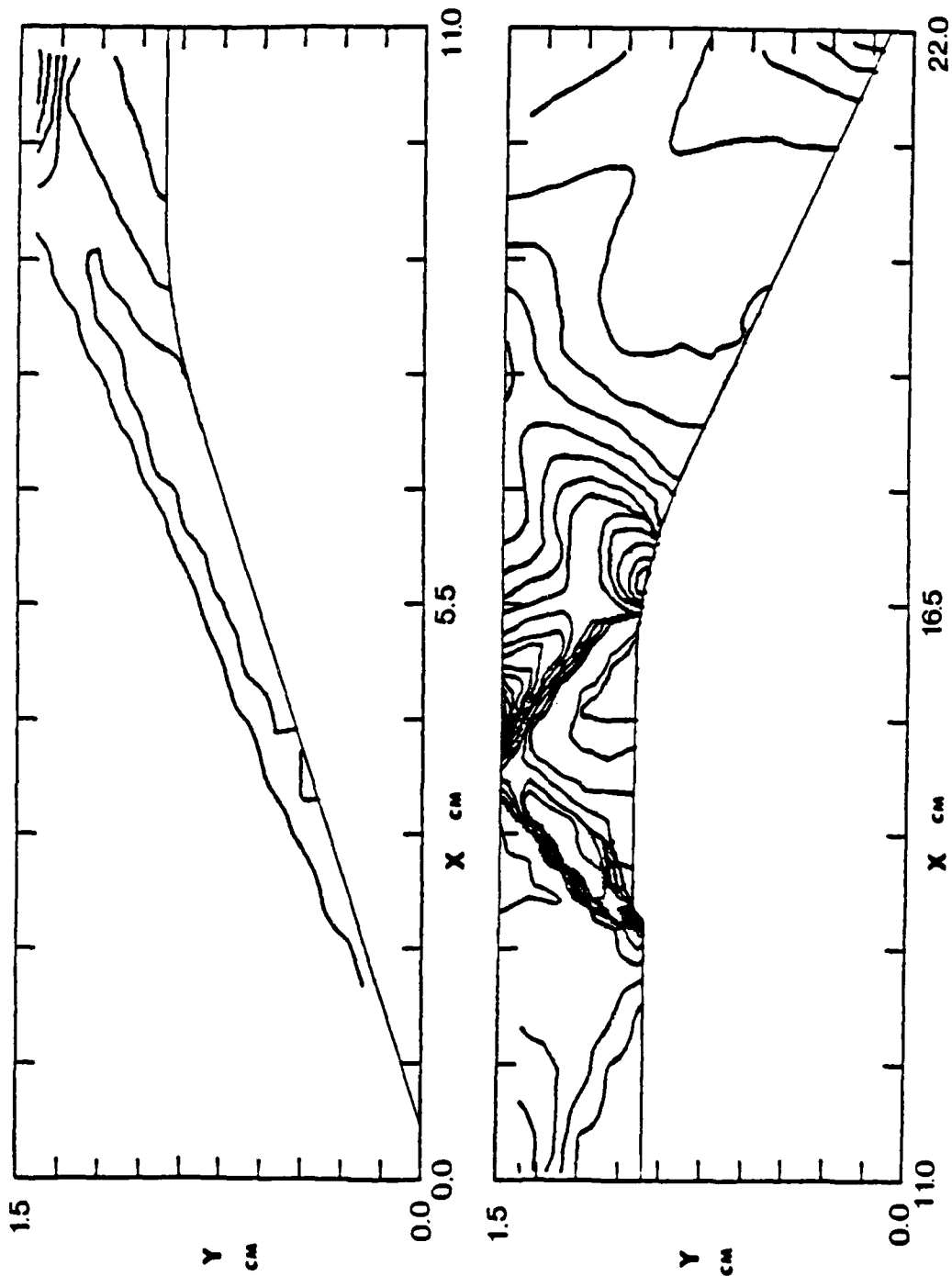


Figure 30. Pressure Contours Surrounding Oblique Detonation Type II Projectile with a 0.04 cm Ramp Height Moving at 8.0 km/sec in Mixture 1. (Contours range from 1.0×10^8 to 3.0×10^9 dyne/cm² with an interval of 1.0×10^8 dyne/cm². The Y-scale is exaggerated 2.57 times.)

system emanating from the rear shoulder. There is some recompression near the rear tip of the projectile.

Projectile lengths of 20.0, 22.0, and 22.5 cm were studied. The only difference between these three projectiles was the length of the cylindrical section downstream of the ramp. Type II oblique detonation thrust pressure ratio and efficiency results are shown in Figures 31 and 32, respectively. At 7.0 km/sec in mixture 1, the 20.0 cm projectile exhibited the highest thrust pressure ratio of 0.301. The 22.5 cm projectile achieved a maximum thrust pressure ratio of 0.279 at 9.0 km/sec in mixture 1. These values do not include the drag produced by the ramp and the thrust pressure ratios are based on the maximum pressure experienced by the projectile itself. Table 3 compares these results with those from the type I oblique detonation study using mixture 1. Thrust pressure ratio (ϕ) and cycle efficiency (η) values are also given which are calculated using 25% of the ramp drag to simulate a projectile with discrete bumps occupying 25% of the 2π azimuthal ramp angle.

TABLE 4. COMPARISON OF TYPES I AND II OBLIQUE DETONATION MODE PERFORMANCE

MODE	VELOCITY (km/sec)	LENGTH (cm)	(Ramp Drag Ignored)		(25% Ramp Drag)	
			ϕ	η	ϕ	η
Type II	7.0	20.0	0.301	0.192	0.281	0.180
Type II	9.0	22.5	0.279	0.181	0.259	0.168
Type I	7.0	14.7	0.123	0.264	---	---
Type I	9.0	14.7	0.048	0.134	---	---

Using the values from Table 4 including 25% ramp drag, we see that ϕ values for the type II mode (0.26-0.28) are much greater than those for the type I mode (0.05-0.12) for the velocity range studied here. The efficiency of the type I mode is greater than that of the type II mode at 7 km/sec but less at 9 km/sec. Our opinion is that, overall, the type II mode is superior, ϕ being greater for this mode by a factor of ~2.3-5.0, while η is comparable or, at worst, less by a factor of ~1.5.

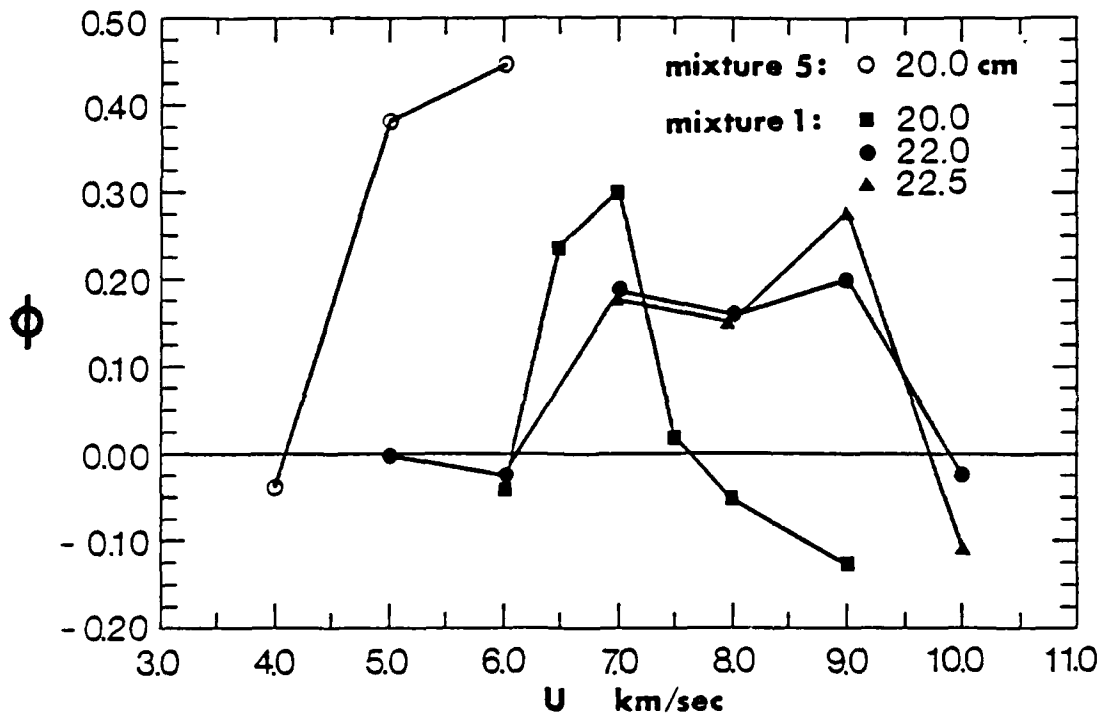


Figure 31. Type II Oblique Detonation Thrust Pressure Ratio Versus Vehicle Velocity for Projectile Lengths and Gas Mixtures Indicated.

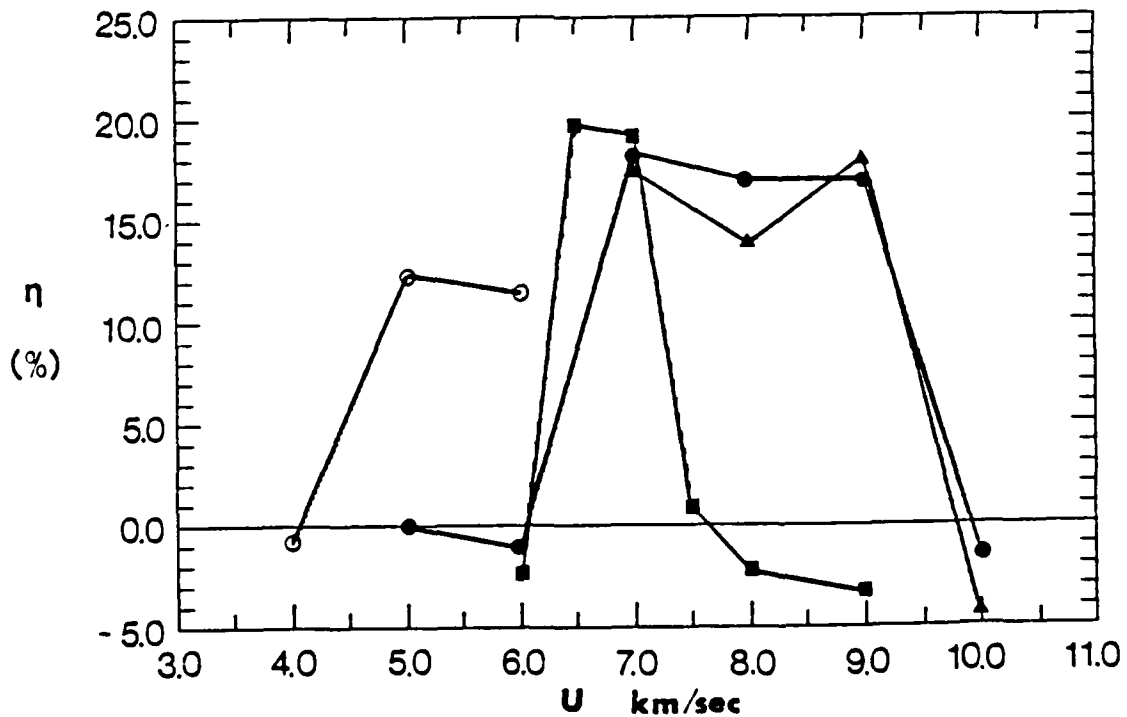


Figure 32. Type II Oblique Detonation Ballistic Efficiency Versus Projectile Velocity for Projectile Lengths and Gas Mixtures as Indicated in Figure 31.

A velocity survey revealed that the longer projectiles operated over a wider velocity range in the same mixture. The highest successful velocity was 7.5 km/sec for the 20.0 cm projectile and 9.0 km/sec for both the 22.0 and 22.5 cm projectiles. For the type II mode, high velocity failure occurs when the detonation and its reflected wave system become stretched out toward the projectile rear to the point that the critical thrust producing area of the upstream part of the projectile tail is mainly subject to relatively low pressures. The net thrust then becomes negative. The high velocity failure mechanism for the type II mode is thus quite different than that for the type I mode, where the high velocity failure mechanism is predetonation on the initial nose shock. The combustible gas mixture can be varied as necessary along the tube length to control the flight Mach number and retain a near optimal thrust producing flow pattern.

3. STRATIFIED CHARGE MODE

At velocities above about 6.0 km/sec, ablation problems must be addressed. One proposed method to reduce the stagnation temperatures experienced by the projectile body is to fly it through a pure hydrogen gas core surrounded by a combustible gas mixture. The relatively cool hydrogen would provide an effective thermal shield between the hot combustion products and the projectile surface, greatly reducing ablative mass loss. This technique would also greatly reduce the frictional drag on the projectile.

The multiple material zone capability of the code can be used to model such a scenario. We have made case studies of an oblique detonation type II projectile flying through such a stratified gas. The gas was stratified as follows. A 1.5 cm radius tube contained pure hydrogen gas from the center to half tube radius; the remainder of the tube was filled with a stoichiometric hydrogen-oxygen mixture. The computational model contained six cells in the radial direction in each of the two gas zones. The inter-zone boundary is impermeable, but movable.

A projectile having a 7° nose cone half angle and a 1.0 cm radius upstream of the ramp moving at 10.0 km/sec through a 100 atm stratified mixture was taken as a benchmark case. As for the oblique detonation type II

mode, the initiation ramp was located somewhat downstream of the location where the reflection of the nose cone shock intersects the projectile surface. For a ramp length of 0.135 cm, a survey was conducted to determine the minimum ramp height necessary to initiate combustion in the outer gas zone. A ramp height of 0.035 cm was found to be the smallest necessary to promptly initiate combustion throughout the outer combustible gas zone. A 0.030 cm ramp height also propagated a shock wave of sufficient strength to ignite the outer mixture. However, the point of complete combustion was downstream of the ramp location by about 3.0 cm, requiring a longer projectile for only a moderate decrease in ramp drag. (The ramp drag for ramp heights of 0.030 cm and 0.035 cm were 0.320 and 0.444, respectively, times that for a 0.050 cm ramp height.) Therefore, the 0.035 cm ramp height was chosen for further study. The ramp drag for the 0.035 cm ramp height case was 0.235 times the projectile thrust for this case, ignoring ramp drag.

Since ignition does not occur on the ramp itself in the stratified charge mode, but rather in the outer gas zone, the shock wave produced by the ramp (or bumps in the three-dimensional case) must retain sufficient strength through the core gas zone. Therefore, discrete bumps would likely have to cover more projectile circumference than in the single gas zone oblique detonation type II mode. A figure of 50% circumferential coverage was arbitrarily chosen for the stratified charge mode performance parameter calculations. A 25% circumferential (azimuthal) coverage had been used for the single gas oblique detonation type II mode calculations. Tail cone half angles of 10° and 5° were investigated. Both produced positive thrust, but the more gradual expansion of the 5° case resulted in a higher efficiency and thrust pressure ratio than was achieved by the 10° degree tail, as shown in Table 5. For tail angles of 10° and 5° , the projectile lengths were 28.5 cm and 33.6 cm, respectively.

TABLE 5. PERFORMANCE OF STRATIFIED CHARGE MODE

RAMP HEIGHT (cm)	TAIL HALF ANGLE (deg)	(Ramp Drag Ignored)		(50% Ramp Drag)	
		ϕ	η	ϕ	η
0.050	10	0.134	0.076	0.088	0.050
0.050	5	0.191	0.108	0.145	0.082
0.035	5	0.283	0.100	0.250	0.088

Figure 33 illustrates the pressure field produced by a projectile with a 0.035 cm ramp height and a 5° tail half angle operating at 10.0 km/sec in the stratified charge mode. In Figure 33, we can see the nose cone shock, followed by the expansion wave emanating from the front shoulder of the projectile. The nose cone shock reflects from the tube wall and intersects the projectile surface somewhat upstream of the initiation ramp. The initiation ramp propagates a shock wave out towards the detonable gas mixture, which detonates, propagating detonation/shock waves both outwards towards the tube wall and inwards towards the projectile. The reflection of the detonation wave from the tube wall then impinges on the projectile in the neighborhood of the rear shoulder, essentially cancelling the expansion wave system which normally would emanate from this shoulder. Thus the pressure is kept reasonably high on the critical thrust producing area of the forward part of the projectile tail, and good performance is obtained. Note that the hydrogen core is very much volumetrically compressed following the initiation of the detonation wave.

Since the computational model is inviscid and has a zone boundary at the gas interface, turbulent mixing at the interface shear layer is not modeled. A large amount of turbulent mixing could cause the protection of the projectile by the hydrogen core to be compromised. A detailed analysis of this problem is beyond the current level of our computational research program. The following rough assessment is offered, however. Because of the hypersonic nature of the flow, the shear layer velocity ratios (λ) are very near unity. From our CFD results, (λ) averages ~ 0.97 and ~ 0.95

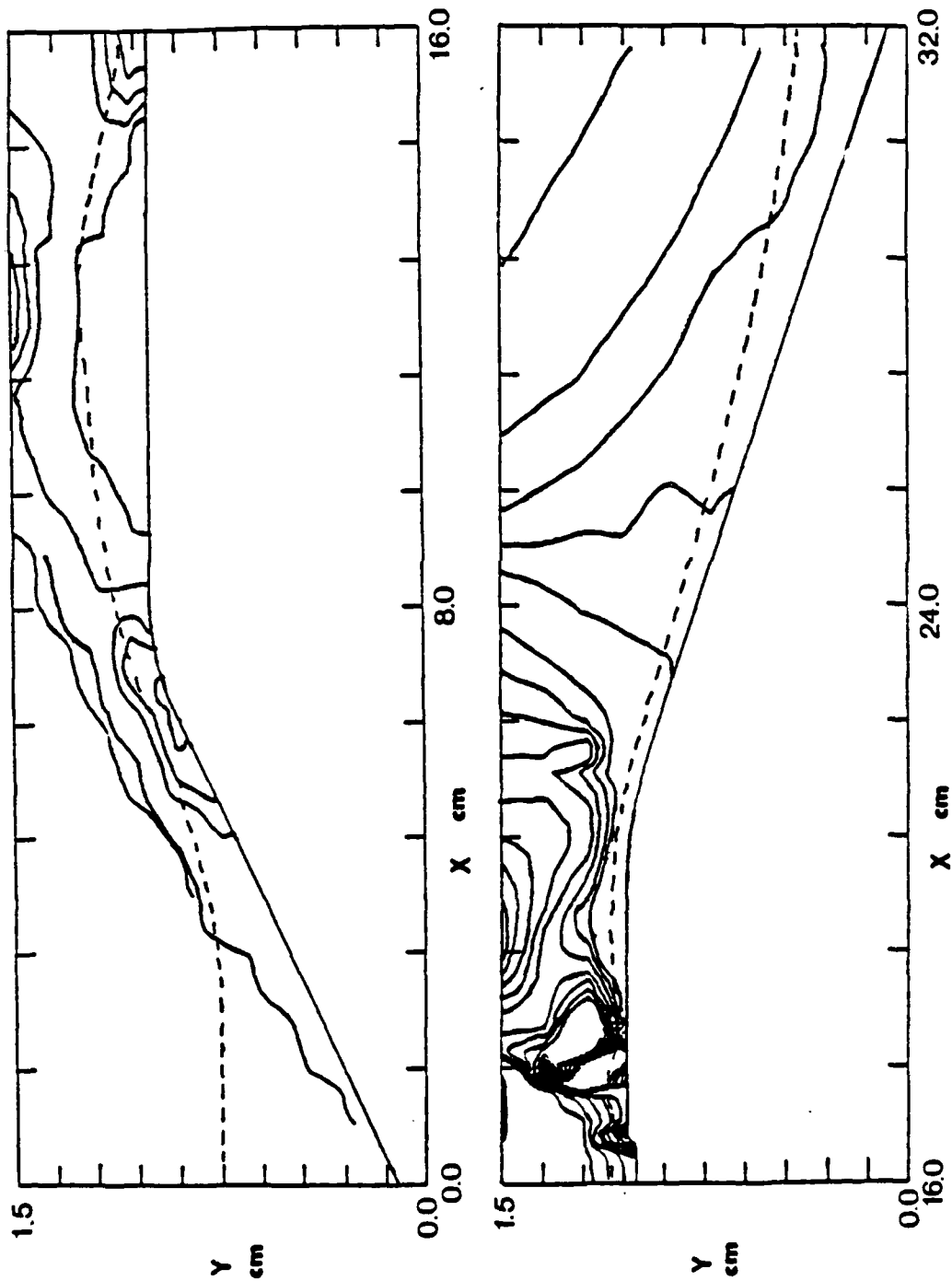


Figure 33. Pressure Contours Surrounding a Projectile with a 0.035 cm Ramp Height Moving at 10.0 km/sec in a Stratified Charge with a H_2 core surrounded by a $2H_2 + O_2$ Gas Mixture. (The maximum pressure contour is 2.6×10^9 dyne/cm² with an interval of 1.0×10^8 dyne/cm². The Y-scale is exaggerated 3.93 times. The gas interface is shown dashed.)

upstream and downstream of the initiation bump, respectively. In Reference 20 the spreading rate of a low speed, constant density shear layer is given as $\delta/x = 0.35$, where δ is the visual shear layer thickness and x is the distance from the shear layer origin. Reference 20 also presents experimental data from a number of authors showing that δ/x depends on λ as $\delta/x = \text{constant} \cdot (1 - \lambda)/(1 + \lambda)$. Here, we make no attempt to allow for density ratio or compressibility effects on the shear layer. We use $\delta = 0.35x(1 - \lambda)/(1 + \lambda)$ to estimate our shear layer thickness, taking the values of λ (0.95 - 0.97) obtained from our CFD code.

The shear layer is conservatively assumed to start at the tip of the nose of the projectile. In this way, we estimate that, over the tail of the projectile, $\delta/2$ will be 0.06 - 0.10 cm, which is about the same size as the H_2 layer thickness at these locations. Our rough estimate, then, is that the H_2 layer protection of the projectile may be just beginning to be compromised over the tail of the projectile. For the calculations presented here, the radius of the H_2 core is half the tube radius. By making the radius of the core somewhat larger than this, the protective layer of H_2 over the projectile could be made substantially thicker, at the cost of some reduction in the amount of chemical energy available in the tube. Especially if such an increase in the size of the H_2 core can be made (and still yield acceptable projectile performance), our rough shear layer spreading rate estimates suggest that thermal protection of the projectile, using a H_2 core, may be feasible. Clearly, considerable further work is necessary to assess the severity of the problem of the spreading of the shear layer by turbulent mixing.

Substantial reduction of stagnation temperature at the projectile surface is afforded by the stratified charge mode. At 10.0 km/sec, the peak stagnation temperature at the surface of a projectile having a 0.035 cm ramp is 3310° Kelvin compared to ~8000° Kelvin estimated for the same projectile at the same velocity in a uniform $8H_2 + O_2$ mixture. (The latter temperature was estimated from code output parameters and assumes an average specific heat value estimated from the JANAF tables (Reference 15).) The problem of projectile ablation is, therefore, greatly reduced by employing the stratified charge configuration.

Table 6 compares the highest operating velocity cases for the types I and II oblique detonation modes and the stratified charge mode. Only the stratified charge mode operated successfully at 10.0 km/sec. The thrust pressure ratio, ϕ , for the stratified charge mode at 10.0 km/sec is somewhat greater than ϕ for the type II oblique detonation mode at 9.0 km/sec, and much greater than ϕ for the type I oblique detonation mode at 9.0 km/sec. There is a penalty for the use of the stratified charge with respect to efficiency, however. Referring to Table 6, the stratified charge case has an efficiency of 0.088 at 10 km/sec versus efficiencies of 0.134 and 0.168 at 9 km/sec for the type I and type II oblique detonation modes, respectively. It may be possible to raise the efficiency of the stratified charge mode somewhat (perhaps to as high as 0.15-0.17) by increasing the maximum radius of the projectile. This increase in η would probably be accompanied by a decrease in ϕ .

TABLE 6. COMPARISON OF TYPES I AND II OBLIQUE DETONATION AND STRATIFIED CHARGE MODES

MODE	VELOCITY (km/sec)	RAMP HEIGHT (cm)	(Ramp Drag Ignored)		(Partial Ramp Drag)	
			ϕ	η	ϕ	η
Type I Oblique Detonation	9.0	(no ramp)	0.048	0.134	---	---
Type II Oblique Detonation	9.0	0.040	0.279	0.181	(25% ramp drag) 0.259	0.168
Stratified Charge	10.0	0.035	0.283	0.100	(50% ramp drag) 0.250	0.088

SECTION VIII

CONCLUSIONS

The ram accelerator concept is a promising method for efficiently accelerating projectiles from velocities of ~ 0.7 km/sec to as high as ~ 12 km/sec, using chemical energy. Several different modes of ram accelerator propulsion have been presented which have, in principle, overlapping limits of operation that span this velocity range. These include two subsonic combustion modes and three detonation modes. The theoretical performance and the operational velocity limits of these modes have been discussed.

Experimental investigations in a 38 mm bore, 12.2 m long ram accelerator facility, using methane-based propellant mixtures at fill pressures up to 25 atm and projectile masses of 45-75 gm, have established proof-of-principle of the subsonic combustion thermally choked ram accelerator mode over the velocity range of 690-2400 m/sec. Staged propellant operation in up to four successive mixtures and stable transition between different mixtures have been confirmed. Operational limits in several propellant mixtures have been determined and the performance of the ram accelerator has been demonstrated to scale with propellant fill pressure and projectile mass as predicted by theory. The effects of projectile geometry on the upper velocity limits of a given mixture have been explored. It has been found that more slender nose cones and longer bodies result in higher velocities. For all propellants investigated velocity increments and ballistic efficiencies have been obtained which agree very well with theoretical predictions.

Velocities up to 3.5 km/sec should be attainable with the thermally choked mode by using hydrogen-based propellant mixtures. To achieve velocities above 3.5 km/sec the detonation driven modes must be used. Experiments to establish the proof of principle of those modes need to be carried out to exploit the full potential of the ram accelerator concept.

REFERENCES

1. A.E. Seigel, "Theory of High-Muzzle-Velocity Guns," Interior Ballistics of Guns, H. Krier, and M. Summerfield, eds., Progress in Astronautics and Aeronautics, Vol. 66, American Institute of Aeronautics and Astronautics, New York, 1979, pp. 135-175.
2. G.L. Dugger, ed., Ramjets, AIAA Selected Reprint Series, American Institute of Aeronautics and Astronautics, New York, Vol. VI, 1969.
3. P.J. Wilbur, C.E. Mitchell, and B.D. Shaw, "The Electrothermal Ramjet," J. Spacecraft and Rockets, Vol. 20, Nov.-Dec. 1983, pp. 603-610.
4. B.D. Shaw, C.E. Mitchell, and P.J. Wilbur, "The Annular Flow, Electrothermal Plug Ramjet," J. Propulsion and Power, Vol. 1, Nov.-Dec. 1985, pp. 417-425.
5. S. Slutsky, and J. Tamagno, General Applied Science Laboratories, Inc., Westbury, NY, 1967. Private communication by C.E. Kepler, United Technologies Research Center, East Hartford, CT, 1985.
6. A. Glasser, Drexel University, Philadelphia, PA, private communication, 1984.
7. R.A. Strehlow, Fundamentals of Combustion, R.E. Krieger Co., Malabar, FL, 1983, Ch. 9.
8. C. Knowlen, D.W. Bogdanoff, A.P. Bruckner, and A. Hertzberg, "Performance Capabilities of the Ram Accelerator," AIAA Paper 87-2152, AIAA/ASEE/ASME/SAE 23rd Joint Propulsion Conference, San Diego, CA, June 29-July 2, 1987.

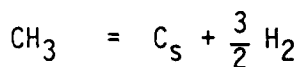
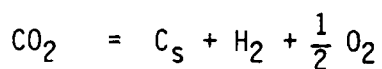
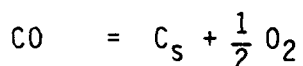
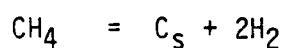
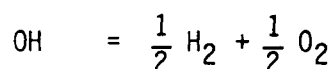
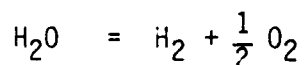
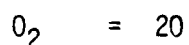
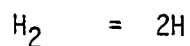
9. H.F. Swift, Physics Applications, Inc., Dayton, OH, private communication, 1986.
10. M. Barrere, et al., Rocket Propulsion, Elsevier Publishing Co., Amsterdam, 1960, pp. 142-149.
11. G.I. Taylor, and J.W. Macoll, "The Air Pressure on a Cone Moving at High Speeds," Proc. Roy. Soc. (London) A, Vol. 139 (1933), pp. 278-311.
12. A.H. Shapiro, The Dynamics and Thermodynamics of Compressible Fluid Flows, Vol. I, Ronald Press, NY, 1953, Chs. 4, 5 and 7, 1953.
13. H. Schlichting, Boundary Layer Theory, 7th ed., McGraw-Hill, NY, 1979, pp. 715-718.
14. A.P. Bruckner, D.W. Bogdanoff, C. Knowlen and A. Hertzberg, "Investigation of Gasdynamic Phenomena Associated with the Ram Accelerator Concept," AIAA Paper 87-1327, AIAA 19th Fluid Dynamics, Plasma Dynamics and Lasers Conference, Honolulu, HI, June 8-10, 1987.
15. D.R. Stull and M. Prophet, project directors, JANAF Thermochemical Tables, U.S. Government Printing Office, June 1971, p. 4.
16. E.R. van Driest, "Turbulent Boundary Layer in Compressible Fluids," Journal of the Aeronautical Sciences, Vol. 18, March 1951, pp. 145-160, 216.
17. L.O.F. Jeromin, "The Status of Research in Turbulent Boundary Layers with Fluid Injection," Progress in Aeronautical Sciences, Vol. 10, 1970, pp. 65-190.
18. D.W. Bogdanoff and D.C. Brackett, "A Godunov CFD Method for Extreme Flow Velocities and any Equation of State," AIAA Journal, in press.

19. R.W. MacCormack, "Current Status of Numerical Solutions of the Navier-Stokes Equations," Paper AIAA 85-0032, AIAA 23rd Aerospace Sciences Meeting, Reno, NE, Jan. 14-17, 1985.
20. G.R. Brown and A. Roshko, "On Density Effects and Large Structure in Turbulent Mixing Layers," Journal of Fluid Mechanics, Vol. 64, Part 4, July 1974, pp. 775-816.

APPENDIX A

ADIABATIC FLAME TEMPERATURE CALCULATIONS FOR CH₄-H₂-O₂ MIXTURES

The adiabatic flame temperature and equilibrium compositions after constant pressure combustion of H₂-O₂ and CH₄-O₂ gas mixtures are determined from a computer program using an abridged table of JANAF thermochemical data. The following equilibria and species are considered for these systems (Reference A-1):



where D signifies nonreacting diluents, such as Ar, He and N₂, and subscript s indicates the solid phase. Any other equilibria can be obtained by simple arithmetic manipulations of the above. The enthalpy per unit mass (h) of the mixture at any temperature is the sum of each species' specific enthalpy (h_j) weighted by its fraction of total density as shown below (Reference A-2):

$$h = \sum_{j=1}^N h_j(T) \frac{\rho_j}{\rho} \quad (\text{A-1})$$

$$\rho = \sum_{j=1}^N \rho_j \quad (\text{A-2})$$

where the total number of species considered is N and the subscript j denotes property of specie j .

The computer program uses two main subroutines: the first computes equilibrium partial pressures, $P_j = f(T,P)$ atm, and the second computes mixture specific enthalpy, $h = h(T,P_j)$ J/kg. The inputs required are the initial temperature T_0 , initial pressure P_0 , and the fuel and diluent to oxidizer ratios $[H_2]/[O_2]$, $[CH_4]/[O_2]$ and $[D]/[O_2]$ where $[] \equiv$ number of moles of each species considered. The output consists of: T_f , $P_{H_2} \dots P_D$, Q , a_e , and any other state variable of interest. Here T_f is the final temperature, a_e is the equilibrium speed of sound, Q is the heat released (J/kg) and P_j is the partial pressure of specie j .

The combusted mixture is assumed to behave as an ideal gas having its total enthalpy h_0 and total pressure P_0 conserved (Reference A-1). The final composition is determined by advancing the temperature and recomputing the equilibria until the enthalpy of the final mixture is equal to the initial enthalpy h_0 . The details of this iteration procedure are as follows: Temperature is advanced for each step 'i' and equilibrium P_{j_i} and h_i are computed. The enthalpy difference (Δ_i) for each step and the preceding difference (Δ_{i-1}) are multiplied and checked to see if the differences are of the same sign. Temperature is advanced until this ceases to be true. The initial temperature guess has $T_1 < T_0$, which makes $h_1 < h_0$, normally. Thus the final temperature will be bounded when the step enthalpy first becomes greater than h_0 .

After upper and lower temperature bounds (T_h and T_l) are found, the step increment is halved and added to each temperature iteration T_i until $h_i > h_0$. While $h_i > h_0$ the step is halved and added to the last temperature value corresponding to $h_i < h_0$. The final temperature after the step

increment is halved 10 times has a maximum error of $\epsilon = \delta/2^{10}$ (e.g., for $\delta = 1000^\circ\text{K}$; $\epsilon = .98^\circ\text{K}$).

At the end of this iteration loop the equilibrium partial pressures and flame temperature are known. From this information all thermodynamic variables can be computed. The final temperature has a maximum possible error of less than 0.1% within the context of the ideal gas assumption and the accuracy of the JANAF thermochemical data. The details of the data interpolations and equilibria subroutine are described in the next sections.

1. THERMOCHEMICAL DATA REPRESENTATION

The temperature variations of the enthalpy and equilibrium constants for each specie are determined from interpolations of a table of JANAF data (Reference A-3). The enthalpies are linearly interpolated between data points at every 200°K . The equilibrium constants are exponentially interpolated between data points at 100° , 200° , 500° , 1000° , 2000° , 3000° , 4000° , 5000° and 6000°K . These interpolations reproduce the JANAF tables between the data points to within .05%.

2. EQUILIBRIA SUBROUTINE

The equilibria subroutine computes mole fractions P_j/P_0 of the mixture at any given temperature. The partial pressures are related to the equilibrium constants, K_{pi} , by the "law of mass action" as follows (Reference A-2):

$$\begin{aligned}
 K_{p1} &= P_{\text{H}}/P_{\text{H}_2}^{\frac{1}{2}} \\
 K_{p2} &= P_{\text{O}}/P_{\text{O}_2}^{\frac{1}{2}} \\
 K_{p3} &= P_{\text{H}_2\text{O}}/P_{\text{H}_2} P_{\text{O}_2}^{\frac{1}{2}} \\
 K_{p4} &= P_{\text{OH}}/P_{\text{H}_2}^{\frac{1}{2}} P_{\text{O}_2}^{\frac{1}{2}} \\
 K_{p5} &= P_{\text{CH}_4}/P_{\text{H}_2}^2
 \end{aligned}
 \tag{A-3}$$

$$K_{p6} = P_{CO}/P_{O_2}^{\frac{1}{2}}$$

$$K_{p7} = P_{CO_2}/P_{O_2}$$

$$K_{p8} = P_{COH_2}/P_{H_2}P_{O_2}^{\frac{1}{2}}$$

$$K_{p9} = P_{CH_3}/P_{H_2}^{\frac{3}{2}}$$

where P_j is the partial pressure of specie j . There are 12 unknown partial pressures and the mole fraction of solid carbon* to be determined. Nine equations are provided by the K_{pi} expressions. Conservation of atoms prescribes the mole ratios of initial atoms (O/H, C/H and D/H) to be constant, which gives three more equations, as follows:

$$\frac{n_O}{n_H} = \frac{P_{H_2O} + P_{OH} + 2P_{O_2} + P_O + 2P_{CO_2} + P_{COH_2}}{2P_{H_2} + 2P_{H_2O} + P_{OH} + P_H + 4P_{CH_4} + 2P_{COH_2} + 3P_{CH_3}} \equiv E \quad (A-4)$$

$$\frac{n_C}{n_H} = \frac{P_{CH_4} + P_{CO} + P_{CO_2} + P_{COH_2} + P_{CH_3} + n_{C_S} \hat{R}T}{2P_{H_2} + 2P_{H_2O} + P_{OH} + P_H + 4P_{CH_4} + 2P_{COH_2} + 3P_{CH_3}} \equiv F \quad (A-5)$$

$$\frac{n_D}{n_H} = \frac{P_D}{2P_{H_2} + 2P_{H_2O} + P_{OH} + P_H + 4P_{CH_4} + 2P_{COH_2} + 3P_{CH_3}} \equiv G \quad (A-6)$$

where the n_j are the number of atoms (or molecules) of specie j .

*The mole fraction of solid carbon does not contribute to the total pressure and $[C_S]$ is determined from the expression for the carbon atom conservation like the other mole fractions are determined.

The 13th equation for the thirteen unknowns is provided by the assumption that the sum of the partial pressures is equal to the initial total pressure P_0 :

$$P_0 = \sum_{j=1}^{12} P_j \quad . \quad (A-7)$$

The partial pressures in the conservation equations are put in terms of P_{O_2} , P_{H_2} and P_D . The diluent partial pressure, P_D , is eliminated from the total pressure relation, which leaves the two following implicit equations with $u = P_{O_2} \bar{Z}$ and $v = P_{H_2} \bar{Z}$:

$$\begin{aligned} X(u,v) = & K_3 v^2 u + K_4 v u + 2u^2 + K_2 u + K_6 u + 2K_7 u^2 + K_8 v^2 u \\ & - E[2v^2 + 2K_3 v^2 u + K_4 v u + K_1 v + 4K_5 v^4 + 2K_8 v^2 u + 3K_9 v^2] = 0 \quad (A-8) \end{aligned}$$

$$\begin{aligned} Y(u,v) = & u^2 + v^2 + K_1 v + K_2 u + K_3 v^2 u + K_5 v^4 + K_6 u + K_7 u^2 \\ & + K_8 v^2 u + K_9 v^3 + G[2v^2 + 2K_3 v^2 u + K_4 v u + K_1 v + 4K_5 v^4 \\ & + 2K_8 v^2 u + 3K_9 v^3] - P_0 = 0 \quad . \quad (A-9) \end{aligned}$$

These two equations are solved using the Newton-Raphson technique (Reference A-4). An initial guess based on a fraction of the maximum partial pressures possible of O_2 and H_2 is iterated upon until the functions X and Y are sufficiently close to zero. The equilibrium partial pressures can then be computed from their O_2 and H_2 relationships.

3. SUMMARY OF THERMODYNAMIC EQUATIONS

$$h(T) = \sum_{j=1}^{13} h_j(T) \frac{P_j}{P_0} \quad (J/Kg)$$

$$C_p = h(T+1) - h(T) \quad (J/Kg^{\circ}K)$$

$$\begin{aligned}
MW &= \sum_{j=1}^{12} MW \frac{P_j}{P_0} && (\text{Kg/mole}) \\
R &= \hat{R}/MW && (\text{J/kg}^\circ\text{K}) \\
\gamma &= C_p/(C_p-R) && (\text{A-10}) \\
a_e &= (\gamma RT)^{1/2} && (\text{m/sec}) \\
HF &= \sum_{j=1}^{13} HF_j \frac{\rho_j}{\rho} && (\text{J/kg}) \\
Q &= HF_0 - HF_f && (\text{J/kg}) \\
P_j &= p_j R_j T && (\text{atm}) \\
P_0 &= \sum_{j=1}^{12} P_j && (\text{atm})
\end{aligned}$$

where C_p is the specific heat at constant pressure, \hat{R} is the universal gas constant, MW is the molecular weight, HF is the mixture enthalpy of formation per unit mass at 0 degree Kelvin, and all other variables and symbols have been previously identified.

REFERENCES

- A-1. S.S. Penner, Chemistry Problems in Jet Propulsion, Pergamon Press, New York, 1957.
- A-2. W.G. Vincenti and C.H. Kruger, Introduction to Physical Gas Dynamics, Wiley, New York, 1965.
- A-3. D.R. Stull and H. Prophet, eds., JANAF Thermochemical Tables, 2nd Ed. NSRDS-NBS 37, National Bureau of Standards, 1971.
- A-4. A. Ralston, A First Course in Numerical Analysis, McGraw-Hill, New York, 1965.

APPENDIX B

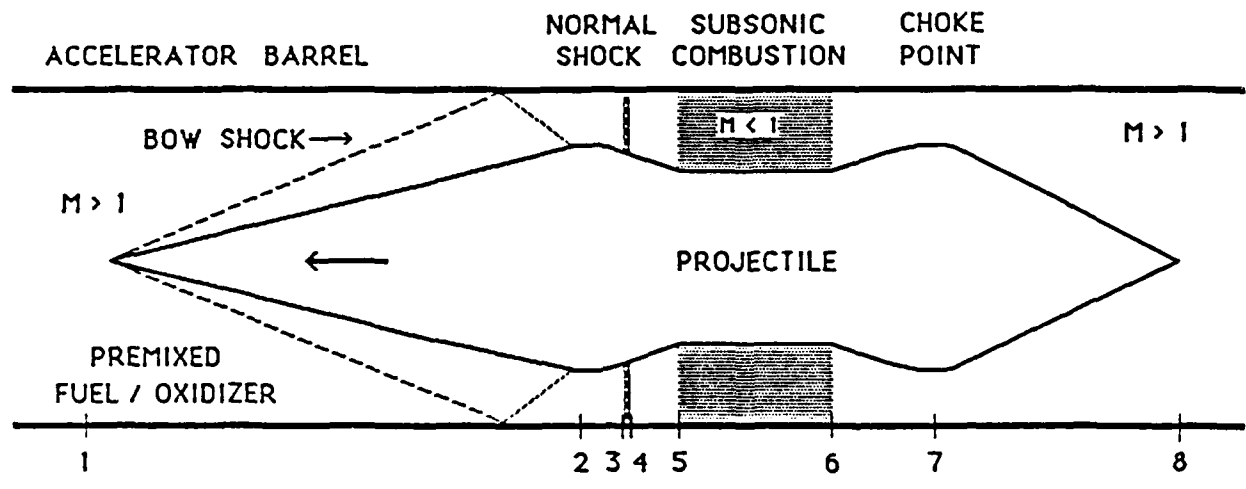
DETAILED 1-D ANALYSIS OF SUBSONIC COMBUSTION AND OVERDRIVEN DETONATION RAM ACCELERATOR MODES

1. INTRODUCTION

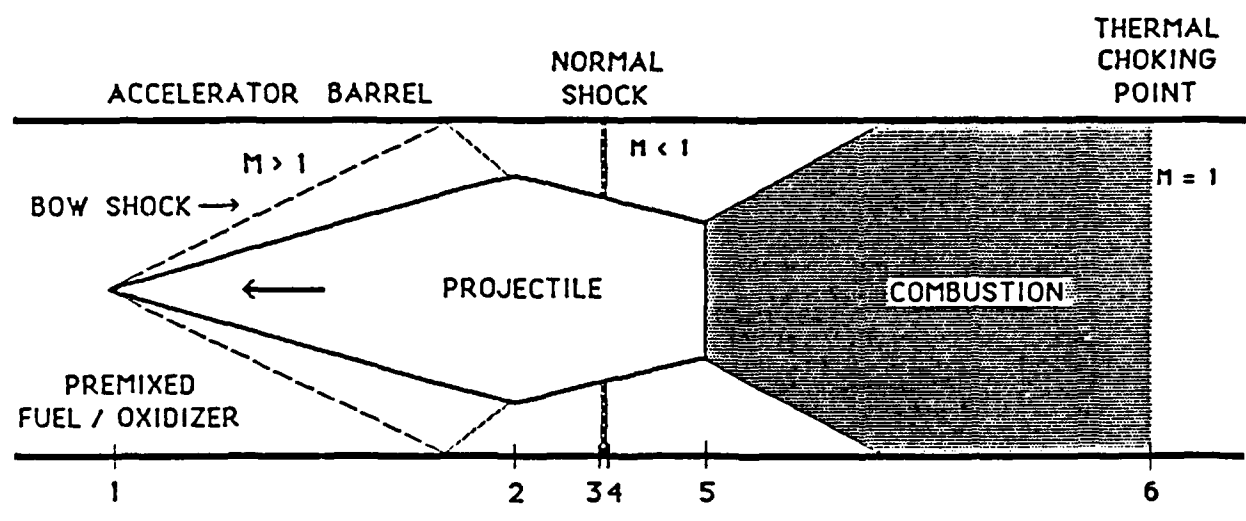
The detailed calculational procedures for both the subsonic combustion and overdriven detonation ram accelerator concepts are carried out using one-dimensional (1-D) steady-flow gasdynamic techniques (Reference B-1). In each case the flow field around the projectile in the launch tube is divided into several stations as shown in Figures B-1 and B-2. The fundamental difference between the two concepts is that in the subsonic combustion mode (which includes the special case of thermal choking) the combustion of the propellant gas occurs in a distributed zone between stations 5 and 6. In the overdriven detonation mode (Figure B-2) all the heat release occurs in a very thin layer immediately following the normal shock in the diffuser. In what follows, the computational method is described in detail for the subsonic combustion mode. The procedure for the overdriven detonation mode is similar, except for the location of the heat release zone. A few remarks regarding this mode are given in the last section of this summary.

2. DIFFUSER

The supersonic flow entering the diffuser gives rise to a series of weak incident and reflected conical shock waves in the converging portion of the diffuser. As noted in Section III of this report, this flow field cannot be computed directly using analytical methods and CFD methods need to be used to obtain a detailed description of the flow. For the purposes of the present approach the supersonic portion of the diffuser has been approximated by an equivalent 2-D wedge diffuser with one reflected shock. It can be shown that this simplifying assumption has no effect on the predicted performance of the device. The flow downstream of the throat up to the location of the normal shock wave is assumed to be isentropic.



a) Mechanically Choked Mode



b) Thermally Choked Mode

Figure B-1. Schematic of Subsonic Combustion Ram Accelerator Modes.

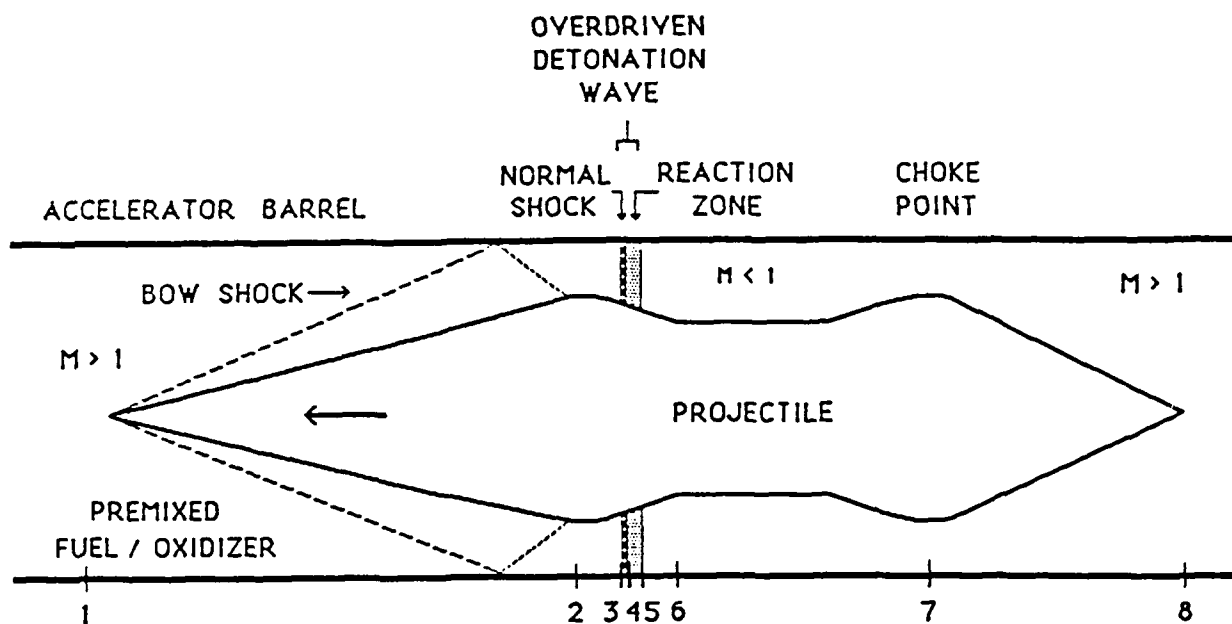


Figure B-2. Schematic of Overdriven Detonation Ram Accelerator Mode.

The first step is to select the projectile geometry, i.e., diffuser shoulder (throat) diameter and waist diameter. The nose angle, body length and tail angle can be chosen arbitrarily within reason, e.g., nose and tail half-angle should not exceed about 15° , etc. For those cases involving thermal choking there is no waist and no exhaust nozzle, i.e., the projectile is a double cone with a truncated rear, as shown in Figure B-1b. The projectile velocity, U_1 , and combustible gas mixture are specified next and the projectile flight Mach number, $M_1 = U_1/a_1$ is computed, where a_1 is the speed of sound in the unreacted gas. The Mach number, M_2 , at the diffuser throat (station 2) corresponding to the initial value of M_1 is then computed from the incident and reflected oblique shock relations. It should be noted that M_2 must be sufficiently greater than 1.0 to prevent any possibility of choking at the diffuser throat or disengagement of the normal shock as a result of small flow disturbances. The projectile to tube diameter ratio, nose angle and M_1 determine the value of M_2 and must be judiciously chosen.

The location of the normal shock behind the throat depends on several parameters, namely M_2 , the heat release from combustion and the area of the nozzle throat. In the case of thermally choked combustion there is no nozzle throat and consequently the location of the shock is uniquely determined by M_2 and the heat release. For stability, the shock must be in the diverging portion of the diffuser, sufficiently behind the throat to avoid disengagement as a result of small disturbances. Typically, the flow area at the shock should be at least 10% greater than at the throat. Once the location of the shock is determined (this is done by iteration), the Mach number, M_3 just prior to the shock (station 3) can be computed from the Mach number-area ratio relation between stations 2 and 3:

$$\frac{A_3}{A_2} = \frac{M_2}{M_3} \left[\frac{1 + \frac{\gamma_1 - 1}{2} M_3^2}{1 + \frac{\gamma_1 - 1}{2} M_2^2} \right] \frac{\gamma_1 + 1}{2(\gamma_1 - 1)} \quad (\text{B-1})$$

where A_2 and A_3 are the flow areas at stations 2 and 3, respectively, and γ_1 is the ratio of specific heats $(C_p/C_v)_1$ of the unreacted gas. It is assumed

that this value of γ remains constant up to the beginning of combustion. This equation for M_3 is an implicit one and must be solved by Newtonian iteration (Reference B-2).

The gas properties at Section 3 are computed from the standard isentropic flow relations:

$$T_{o3} = T_{o2} = T_{o1} \quad (B-2)$$

$$P_{o3} = P_{o2} \quad (B-3)$$

$$T_3 = \frac{T_{o3}}{1 + \frac{\gamma-1}{2} M_3^2} \quad (B-4)$$

$$P_3 = \frac{P_{o3}}{\left(1 + \frac{\gamma_1-1}{2} M_3^2\right)^{\frac{\gamma_1}{\gamma_1-1}}} \quad (B-5)$$

where

$$T_{o1} = T_1 \left(1 + \frac{\gamma_1-1}{2} M_1^2\right) \quad (B-6)$$

and where P_{o2} is obtained from the stagnation pressure ratio, $(P_{o2}/P_{o1})_{diff}$, across the incident and reflected oblique shocks in the diffuser. The reference stagnation pressure, P_{o1} , upstream of the diffuser is given by:

$$P_{o1} = P_1 \left(1 + \frac{\gamma_1 - 1}{2} M_1^2\right)^{\frac{\gamma_1}{\gamma_1 - 1}} \quad (\text{B-7})$$

The subscript "o" denotes stagnation conditions. P_1 and T_1 are the initial tube fill pressure and temperature, respectively. (For all calculations T_1 is assumed to be 300°K. The value of P_1 depends on the specific application being considered and typically ranges from 5 to 400 atm.) In the experiments the highest pressure used to date has been 25 atm. Implicit in all the above and what follows is the assumption that the unreacted propellant gas and the combustion products obey the ideal gas law:

$$P = \rho RT \quad (\text{B-8})$$

where ρ is the density and R is the gas constant for the particular gas composition.

The conditions across the normal shock (station 4) are computed from the standard normal shock relations:

$$M_4^2 = \frac{M_3^2 + \frac{2}{\gamma_1 - 1}}{\frac{2\gamma_1}{\gamma_1 - 1} M_3^2 - 1} \quad (\text{B-9})$$

$$T_{o4} = T_{o3} \quad (\text{B-10})$$

$$T_4 = \frac{T_3 \left(1 + \frac{\gamma_1 - 1}{2} M_3^2\right) \left(\frac{2\gamma_1}{\gamma_1 - 1} M_3^2 - 1\right)}{\frac{(\gamma_1 + 1)^2}{2(\gamma_1 - 1)} M_3^2} \quad (\text{B-11})$$

$$P_4 = P_3 \left[\frac{2\gamma_1}{\gamma_1 + 1} M_3^2 - \frac{\gamma_1 - 1}{\gamma_1 + 1} \right] \quad (\text{B-12})$$

$$P_{04} = P_{03} \frac{\left[\frac{\frac{\gamma_1 + 1}{2} M_3^2}{1 + \frac{\gamma_1 - 1}{2} M_3^2} \right]^{\frac{\gamma_1}{\gamma_1 - 1}}}{\left[\frac{2\gamma_1}{\gamma_1 + 1} M_3^2 - \frac{\gamma_1 - 1}{\gamma_1 + 1} \right]^{\frac{1}{\gamma_1 - 1}}} \quad (\text{B-13})$$

The flow between stations 4 and 5 is subsonic and isentropic. Because the flow area increases, the gas is further decelerated. Knowing the waist diameter, we can compute flow area A_5 and area ratio A_5/A_4 (note that $A_4 = A_3$). From this, M_5 , the Mach number at station 5 can be computed using a Mach number area ratio relation similar to Equation B-1. Using isentropic flow relations similar to Equations B-2 through B-5 the gas properties at station 5 are computed. In the case of thermally choked combustion (Figure B-1b) there is no waist. In this case it is assumed, for analytical simplicity, that combustion starts just behind the projectile base at the full tube area, i.e., $A_5 = A_1$.

3. COMBUSTION

Combustion occurs subsonically in the zone between stations 5 and 6. The heat release for a particular propellant mixture is computed by means of a constant-pressure adiabatic flame temperature routine. Mixtures of hydrogen, methane and oxygen, with diluents such as nitrogen, carbon dioxide, argon and helium can be used. Appendix A of this report describes the computational scheme. The combustion is characterized by a heat release,

Δq , which raises the enthalpy of the flow. The combustion routine also computes the molecular weight and specific heat ratio of the combustion products. The details of the combustion process, such as reaction kinetics, are not included in the current model. The effect of Δq on the flow is computed using standard one-dimensional analysis, generalized to include the changes in molecular weight and specific heat ratio resulting from combustion (Equations B-14 through B-20 below). Since heat addition to a flowing gas reduces the static pressure, i.e., $P_6 < P_5$, the combustion routine is repeated a second time, using P_6 instead of P_5 as the reference pressure. Because the chemical equilibrium is only weakly dependent on pressure and because the pressure is reduced by combustion by a factor of about 2, one iteration on the combustion routine is sufficient for convergence.

Because the flow is adiabatic up to station 5 the stagnation enthalpy remains constant at its value of h_{o1} up to that point, i.e., $h_{o5} = h_{o1}$. The energy equation across the combustion zone can thus be written as:

$$h_{o6} = h_{o1} + \Delta q \quad (B-14)$$

where h_{o6} is the stagnation enthalpy after combustion. Assuming that $C_{p1} = \text{const.}$ and $C_{p6} = \text{const.}$, the stagnation enthalpies can be written in the form $h_o = C_p T_o$. Thus,

$$C_{p6} T_{o6} = C_{p1} T_{o1} + \Delta q \quad (B-15)$$

and the stagnation temperature at station 6 is

$$T_{o6} = \left(\frac{C_{p1}}{C_{p6}} \right) T_{o1} + \frac{\Delta q}{C_{p6}} \quad (B-16)$$

The Mach number at Section 6 is obtained from the implicit relation:

$$\frac{T_{o6}}{T_{o1}} = \frac{M_6^2}{M_5^2} \cdot \frac{(1 + \gamma_1 M_5^2)^2}{(1 + \gamma_6 M_6^2)^2} \cdot \frac{(1 + \frac{\gamma_6 - 1}{2} M_6^2)}{(1 + \frac{\gamma_1 - 1}{2} M_5^2)} \cdot \frac{(\gamma_6 m_6)}{(\gamma_1 m_1)} \quad (B-17)$$

where $\gamma_6 = (C_p/C_v)_6$, $m_6 =$ molecular weight of the combustion products and $m_1 =$ molecular weight of the unreacted gas mixture.

In those cases involving thermal choking, M_6 is set equal to 1.0 and an iteration is carried out on the location of the normal shock which will result in appropriate conditions at station 5 to result in thermal choking at station 6 for the computed value of Δq .

Once M_6 is determined from Equation B-17 (or set to 1.0 for thermal choking), the other thermodynamic variables at station 6 are computed as follows:

$$P_6 = P_5 \left(\frac{1 + \gamma_1 M_5^2}{1 + \gamma_6 M_6^2} \right) \quad (B-18)$$

$$P_{o6} = P_{o5} \frac{P_6}{P_5} \frac{\left[1 + \frac{\gamma_6 - 1}{2} M_6^2 \right]^{\frac{\gamma_6}{\gamma_6 - 1}}}{\left[1 + \frac{\gamma_1 - 1}{2} M_5^2 \right]^{\frac{\gamma_1}{\gamma_1 - 1}}} \quad (B-19)$$

$$T_6 = T_5 \frac{M_6^2}{M_5^2} \frac{(1 + \gamma_1 M_5^2)^2 (\gamma_6 m_6)}{(1 + \gamma_6 M_6^2)^2 (\gamma_1 m_1)} \quad (B-20)$$

It should be noted that in the thermally choked case the combustion occurs behind the projectile in the full cross-sectional area of the launch tube, and therefore, in principle, there is no limit imposed on the length of the reaction zone.

4. EXHAUST NOZZLE

In those cases not involving thermal choking, a convergent-divergent supersonic exhaust nozzle is required. For simplicity, the flow through the exhaust nozzle (stations 6-8) is assumed to be isentropic and frozen, i.e., the composition, molecular weight and specific heat ratio of the combustion products are assumed to remain the same as at station 6. The validity of this assumption at high pressures has been verified in separate computations comparing equilibrium and frozen flow through a supersonic nozzle having the same inlet conditions. Because of the high pressures, there is very little difference between equilibrium and frozen flow.

The area ratio A_7/A_6 is computed from the choking condition at the nozzle throat, i.e., $M_7 = 1$. From this, and the previously calculated tube diameter, the diameter of the projectile at the nozzle throat is computed.

The area ratio A_8/A_7 is computed next (noting that $A_8 = A_1$) and the Mach number at station 8 is obtained from

$$\frac{A_8}{A_7} = \frac{1}{M_8} \left[\left(\frac{2}{\gamma_6 + 1} \right) \left(1 + \frac{\gamma_6 - 1}{2} M_8^2 \right) \right]^{\frac{\gamma_6 + 1}{2(\gamma_6 - 1)}} \quad (\text{B-21})$$

The gas properties are readily computed from the isentropic relations:

$$P_{08} = P_{06} \quad (\text{B-22})$$

$$T_{08} = T_{06} \quad (\text{B-23})$$

$$P_8 = \frac{P_{08}}{\left(1 + \frac{\gamma_6 - 1}{2} M_8^2 \right)^{\frac{\gamma_6}{\gamma_6 - 1}}} \quad (\text{B-24})$$

$$T_8 = \frac{T_{08}}{\left(1 + \frac{\gamma_6 - 1}{2} M_8^2\right)} \quad (\text{B-25})$$

5. THRUST AND DRAG

The thrust, F_t , of the ramjet cycle is calculated from the momentum equation applied between stations 1 and 8:

$$F_t = P_8 A_8 (1 + \gamma_6 M_8^2) - P_1 A_1 (1 + \gamma_1 M_1^2) \quad (\text{B-26})$$

For the thermally choked case ($M_6 = 1$, $A_6 = A_1$), this expression is modified to:

$$F_t = P_6 A_6 (1 + \gamma_6) - P_1 A_1 (1 + \gamma_1 M_1^2) \quad (\text{B-27})$$

The frictional drag on the vehicle is calculated from the relation

$$C_f = \frac{F_d}{\frac{1}{2} \rho u^2 S} = \frac{F_d}{\frac{1}{2} \gamma P M^2 S} \quad (\text{B-28})$$

where C_f is the skin friction coefficient, F_d is the frictional drag, ρ is the local gas density, P , the local static pressure, u the local velocity, M the local Mach number, γ the local specific heat ratio and S the "wetted" surface area. This relation is applied separately to each distinct surface element of the projectile, i.e., nose, body, nozzle, etc. For the subsonic sections of the flow $C_f = 0.003$ is assumed, while for the supersonic portions of the flow, this value is corrected for Mach number dependency (Reference B-3). Over each section of the projectile the average values of Mach number and gas properties are used. For most of the cases investigated

to date the frictional drag turns out to be less than 2% of the gross thrust.

6. EQUATION OF MOTION

The equation of motion of the projectile along the launch tube is simply:

$$\frac{dU_1}{dt} = \frac{F}{m} \quad (\text{B-29})$$

where m is the projectile mass and U_1 and $F = F_t - F_d$ are the instantaneous projectile velocity and net thrust, respectively. This relation is rewritten to obtain velocity as a function of distance, x , along the launch tube:

$$\frac{dU_1}{dx} = \frac{F}{mU_1} \quad (\text{B-30})$$

Since the thrust is a function of velocity, the equation of motion is integrated numerically, using the 4th order Runge-Kutta technique (Reference B-2).

7. OVERALL COMPUTATIONAL TECHNIQUE

The calculational procedure begins by computing the ramjet cycle parameters and resulting net thrust at the projectile injection conditions for the propellant gas composition of interest. The equation of motion is integrated through one incremental step, for the new set of inlet conditions, and so on. The normal shock moves away from the throat as the projectile velocity increases. Typically, for the range of projectile Mach numbers of interest the shock moves from approximately $0.95D_2$ to $0.65D_2$, where D_2 is the projectile diameter at the diffuser throat.

The cycle calculations and equation of motion are stepped forward until a predetermined projectile Mach number, velocity, peak cycle pressure, or tube length is reached. To keep the peak pressures from rising to excessive levels, the projectile should, ideally, be constrained to operate at a constant Mach number by having a continuously graded propellant composition in

the launch tube. The exact composition profile (ranging from a low speed of sound mixture at the entrance to a high speed of sound mixture at the muzzle) is a function of the projectile velocity profile, which in turn depends on the composition profile. The computational difficulties in determining the proper composition profile are at present circumvented by approximating such a profile as a series of tube segments having different propellant compositions and constraining the projectile to operate in a narrow Mach number range, approximately $2.5 < M_1 < 4.0$, in each segment. The projectile is injected into a low speed of sound mixture and progresses into successive segments having propellant mixtures with ever increasing acoustic speeds. The pressure and temperature are the same for all segments.

8. OVERDRIVEN DETONATION RAM ACCELERATOR

The configuration of the overdriven detonation ram accelerator is shown in Figure B-2. Note that this geometry is similar to the subsonic combustion geometry of Figure B-1a. The same general computational scheme described in the preceding sections of this appendix is used to analyze the overdriven detonation ram accelerator, except for the treatment of the heat release zone.* In the overdriven detonation mode the combustion occurs in a very thin layer adjacent to the normal shock. Figure B-2 shows the division of the flow field. From station 1 to station 4 the computation is identical to that for the subsonic combustion mode, except that the velocity and Mach number are higher. In the overdriven detonation mode, however, there is no change in flow area, Mach number or flow properties between the shock and reaction layer. Heat release occurs in a thin layer and the subsonic combustion products are then decelerated by the increase in flow area between station 5 and the waist (station 6). As in the case of the subsonic combustion mode of Figure B-1a, a waist is necessary to provide a region of increasing flow area behind the diffuser throat, where the shock can move in response to the increasing flow velocity as the projectile accelerates. The

* Note also that the numbering of the stations used in the cycle analysis is different.

flow following heat release is assumed to be frozen. The exhaust nozzle is computed in the manner previously described.

It should be noted that for optimum thrust and efficiency the flow Mach number immediately following the overdriven detonation wave (station 5) should be close to 1, i.e., nearly choked. However, the choking condition, $M_5 = 1$, corresponds to the Chapman-Jouguet (C-J) detonation wave, which is unstable in either a diverging or converging duct. Consequently, the operating parameters are chosen such that M_5 does not exceed a value of ~ 0.8 . The skin friction drag is somewhat higher than in the subsonic combustion case due to the higher projectile Mach numbers; however, the drag does not exceed 5% of the gross thrust, even in the worst case.

It should be noted that an overdriven detonation wave is highly stable and exhibits none of the characteristic spinning modes and cellular structures of C-J detonations (Reference B-4). The overdriven detonation wave behaves as an ideal "flame holder" with nearly instantaneous heat release.

REFERENCES

- B-1. A.H. Shapiro, The Dynamics and Thermodynamics of Compressible Fluid Flows, Vols. I and II, Ronald Press, NY, 1953, Chs. 4, 5, 7, 17, 1953.
- B-2. A. Ralston, A First Course in Numerical Analysis, McGraw-Hill, NY, 1965.
- B-3. H. Schlichting, Boundary Layer Theory, 7th Ed., McGraw-Hill, NY, 1979, pp. 715-718.
- B-4. R.A. Strehlow, Fundamentals of Combustion, R.E. Krieger Col., Malabar, FL, 1983, Ch. 9.

APPENDIX C

CFD NUMERICAL PROCEDURES FOR OBLIQUE DETONATION MODES

1. MULTIPLE ZONING

Both one- and two-dimensional codes have been constructed. The two-dimensional codes can be run in either planar or axisymmetric geometries. All of the codes can be divided in the y or radial direction into multiple zones containing different media. The grids can slide in the y direction to preserve the integrity of the media of the zones.

2. GOVERNING EQUATIONS

The two-dimensional Euler equations, written in conservation form are:

$$\frac{\partial U}{\partial t} + \frac{\partial F}{\partial x} + \frac{\partial G}{\partial y} = 0 \quad (C-1)$$

where the state vector U is given by

$$U = \begin{bmatrix} \rho \\ \rho u \\ \rho v \\ e_t \\ \rho m_1 \\ \rho m_2 \\ \cdot \\ \cdot \\ \cdot \end{bmatrix} \quad (C-2)$$

and the flux vectors F and G in the x and y directions are given by

$$F = \begin{bmatrix} \rho u \\ \rho u^2 + p \\ \rho uv \\ u(e_t + p) \\ \rho u m_1 \\ \rho u m_2 \\ \cdot \\ \cdot \\ \cdot \end{bmatrix} \quad G = \begin{bmatrix} \rho v \\ \rho v u \\ \rho v^2 + p \\ v(e_t + p) \\ \rho v m_1 \\ \rho v m_2 \\ \cdot \\ \cdot \\ \cdot \end{bmatrix} \quad (C-3)$$

where e_t denotes total energy per unit volume, u axial velocity, v radial or y-direction velocity, m_i the mass fraction of the i th component, and $e_t = \rho(e + u^2/2 + v^2/2)$. The speed of sound c , temperature and p are obtained from ρ and e using the EOS. The code uses the finite volume technique. The state variables are calculated at the center of each computational cell.

3. DETERMINATION OF CELL BOUNDARY VALUES

The fluxes at the cell boundaries are calculated from values of the primitive variables (ρ , u , v , e , m_i) on the two sides of the boundary. The cell boundary values are obtained by extrapolation and/or interpolation from the cell center values. Most of the calculations of internal cell boundary values are done with third order extrapolations/interpolations. The extrapolations/interpolations are not always simple third order (parabolic fits), however. If the three points being curve fit are so disposed to imply non-monotonic behavior over their range, the third order curve fits are replaced by second or first order fits. A smoothly blended transition is made between the third order fits (used when the three points are well behaved) and the lower order fits.

Referring to Figure C-1, at cell boundary 1, if first order were used, the cell boundary values at L1 and R1 would simply be the values at c and d , respectively. The final third order boundary value at each side of a cell boundary is taken to be $\zeta \times (\text{extrapolated value}) + (1-\zeta) \times (\text{interpolated value})$,

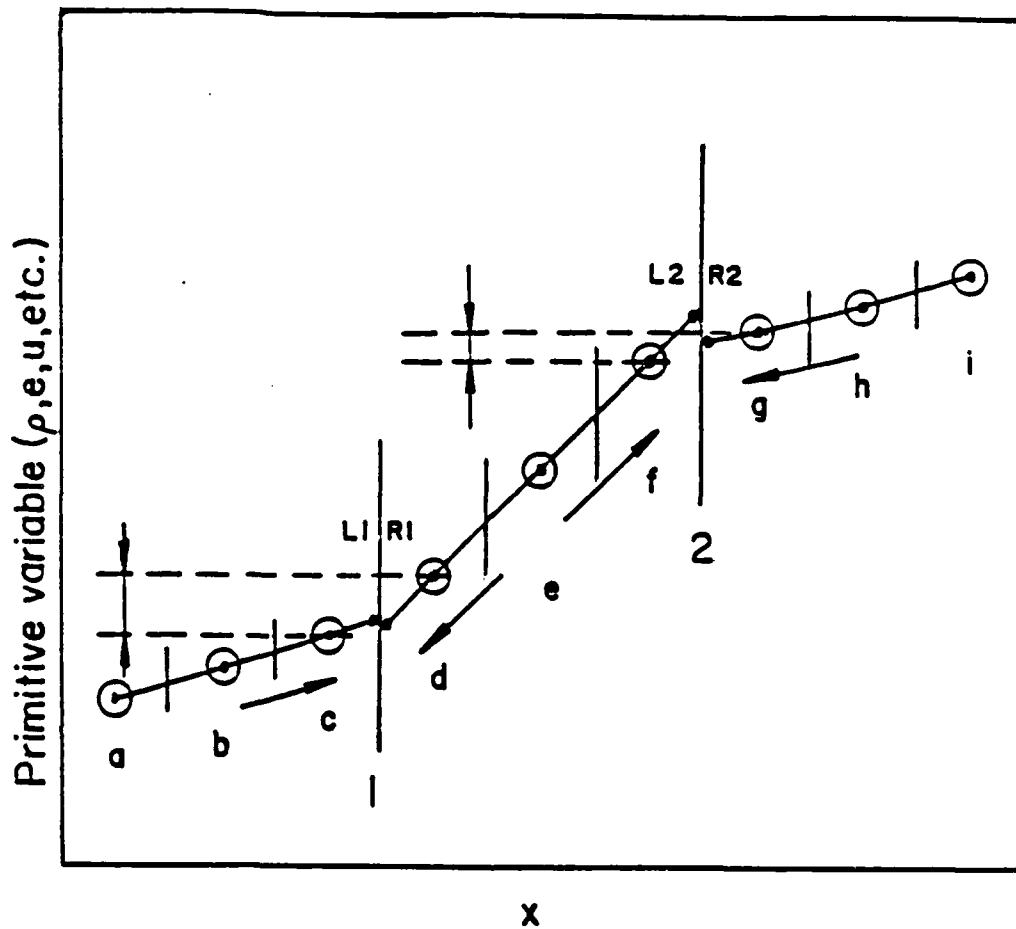


Figure C-1. Illustration of Extrapolation, Interpolation and Cell Boundary Value Correction Techniques. (Circles are cell center values and dots are extrapolated/interpolated cell boundary values. Arrows parallel to the primitive variable profile denote the direction of extrapolation/interpolation. Vertical arrow pairs denote range of acceptable cell boundary values.)

where ζ is a constant. Generally, for internal cell boundaries, third order procedures with $\zeta = 0.5$ give the best results.

In Figure C-1, the blended extrapolated/interpolated cell boundary values at the left and right sides of boundary 2 are indicated by L2 and R2.

An essential limiting procedure that must be applied is that no extrapolated/interpolated value can lie outside the range of the two adjoining cell center values. At boundary 1 in Figure C-1, both of the basic extrapolated/interpolated values are acceptable, while at boundary 2, the value of L2 is not. The simplest way of replacing such unacceptable extrapolated/interpolated values is by the cell center value from the extrapolation/interpolation side. This technique is very stable, but is unnecessarily diffusive. The numerical diffusion can be reduced by, instead, replacing the unacceptable extrapolated/interpolated value by whichever of the two cell center values is closest to the unacceptable value. This procedure, while greatly reducing diffusion, tends to reintroduce some solution oscillation problems. The best compromise procedure we have found to date is as follows. If the extrapolated/interpolated value is beyond the cell center value on the extrapolation/interpolation side of the boundary, that cell center value is used instead. In what follows, we shall refer to the extrapolation/interpolation side of the boundary as the "near" side and the opposite side as the "far" side. What is done is that a certain value for the primitive variable is chosen which is $n = \xi \times (\text{far side value}) + (1 - \xi) \times (\text{near side value})$, where ξ is a constant. When the extrapolation/interpolation value is beyond n in the direction of the "far" side, it is replaced by n . Our best results have been obtained with $\xi \approx 0.5$.

For very high velocity flows (above ~ 30 km/sec), to avoid wiggles in the neighborhood of strong wave systems, we have usually found it necessary to apply the following "strong wave limiting" (SWL) technique. In the direction normal to the cell boundary in question the following quantities are calculated between all adjacent pairs of cells within the extrapolation/interpolation range.

$$\beta_{1i} = u_{i,\perp} - u_{i+1,\perp} / [\min(c_i, c_{i+1})] \quad (C-4)$$

$$\beta_{2i} = p_i - p_{i+1} / [\min(\rho_i c_i^2, \rho_{i+1} c_{i+1}^2)] \quad (C-5)$$

$$\beta_{3i} = \rho_i c_i - \rho_{i+1} c_{i+1} / [\min(\rho_i c_i, \rho_{i+1} c_{i+1})] \quad (C-6)$$

The subscripts i and $i+1$ denote any two adjacent cells within the extrapolation/interpolation range. $u_{i,\perp}$ and $u_{i+1,\perp}$ denote velocities normal to the boundary in question. Equation C-4 compares normal velocity differences with speeds of sound, Equation C-5 compares pressure differences with the elastic modulus of the media, ρc^2 , and Equation C-6 compares differences in the acoustic impedance, ρc , with the acoustic impedances themselves. For any cell boundary all three β values are examined over the range of the extrapolation/interpolation. The maximum β value, β_m , is found. First order, higher order or a blend of first order and higher order extrapolations are used according to the value of β_m , as shown in Table C-1.

TABLE C-1. SELECTION OF FIRST OR HIGHER ORDER EXTRAPOLATIONS/INTERPOLATIONS DEPENDING ON β_m .

β_m Range	Extrapolation/Interpolation Technique
$\beta_m > \alpha_1$	First order
$\alpha_1 > \beta_m > \alpha_2$	$\zeta \times (\text{first order}) + (1-\zeta) \times (\text{higher order})$
$\alpha_2 > \beta_m$	Higher order

α_1 and α_2 are critical values and $\zeta = (\beta_m - \alpha_2) / (\alpha_1 - \alpha_2)$. Abrupt switching between first and higher order produced poor results so a smooth blend was used as shown in Table C-1 for $\alpha_1 > \beta_m > \alpha_2$. Most of our results at velocities above ~ 30 km/sec were obtained using strong wave limiting techniques with α_1 between 1.4 and 4.0 and α_2 between 0.7 and 2.0. Especially with the higher values of α_1 and α_2 , the strong wave limiting is

not used in most of the flow field, but only in the neighborhood of very strong wave systems.

4. FLUX CALCULATION PROCEDURE

The first order Godunov procedure is briefly described here. All Godunov procedures are done in rotated co-ordinate systems so that the new (rotated) x and y co-ordinates are normal and parallel to the cell boundary, respectively. A vertical cell boundary with state 1 to the left and state 5 to the right is considered. In general, solution of the one-dimensional Riemann problem will produce two new zones, 2 and 4 (the ordering of the zones is 1 to 5, left to right), two waves, 12 and 45, propagating to the left and right relative to the media, respectively, and a contact surface 24 dividing zones 2 and 4. Applying the characteristic equations

$$dp = -\rho c du \quad (C-7)$$

and

$$dp = \rho c du \quad (C-8)$$

across waves 12 and 45 allows $p_2 = p_4$ and $u_2 = u_4$ to be determined. Using the u characteristic equation

$$de = p \frac{d\rho}{\rho^2} \quad (C-9)$$

and the EOS between states 1 and 2 and 4 and 5 allows ρ_2 , ρ_4 , e_2 and e_4 to be determined. From the velocities of the waves 12 and 45 and the contact surface 24, the zone in which the cell boundary will reside during the current timestep can be determined and the fluxes determined from the primitive variables in that zone. The v velocities and the mass fractions at the cell boundary are taken as those in states 1 or 5, accordingly, as the con-

tact surface 24 lies to the right or left of the cell boundary, respectively.

It is necessary to limit the Godunov predictions of p , ρ and e to positive values or for p , to the tensile or spall strength of the media. Also, under severe expansion conditions, it may be necessary to include a void zone 3 between zones 2 and 4. The calculation of wave velocities requires some care. For example, assume that 45 is an expansion wave. In this case, the wave velocity can safely be taken to be $((u_4 + c_4) + (u_5 + c_5))/2$. If the wave is a compression wave, this value cannot always be used, since it may become smaller than the contact surface velocity, u_4 , producing an inconsistent solution. A satisfactory first order wave velocity in this case is, rather, $u_4 + c_5$. The same care must be taken with the speed of wave 12, of course.

The second order Godunov procedure used here is very similar to the first order procedure outlined above, except that Equations C-7 and C-8 are replaced with quadratic relations between $p_2(= p_4)$ and $u_2(= u_4)$ which can be solved for p_2 and u_2 . Second order accurate integrations of Equations C-7 to C-9 are used to obtain ρ_2 , ρ_4 , e_2 and e_4 . Different integrations are used for expansion and compression waves; for the latter, shock wave relationships are used extensively. No iterative procedures are required.

The decision of whether to use first or second order Godunov procedures at a given cell boundary is handled as follows. Let the subscripts l and r indicate conditions on the two sides of the cell boundary in question. The following parameters are calculated

$$\beta_{1g} = u_{1l} - u_{r1} / [\min(c_l, c_r)] \quad (C-10)$$

and

$$\beta_{2g} = p_l - p_r / [\min(\rho_l c_l^2, \rho_r c_r^2)]. \quad (C-11)$$

β_{1g} and β_{2g} give two measures of the strength of the waves which will be produced at the cell boundary on the solution of the Riemann problem. β_{mg}

is the greater of β_{1g} and β_{2g} . Two critical values α_{1g} and α_{2g} are chosen. The fluxes are calculated according to the relative values of β_{mg} , α_{1g} and α_{2g} as shown in Table C-2.

TABLE C-2. SELECTION OF FIRST OR SECOND ORDER GODUNOV CALCULATIONS DEPENDING ON β_{mg}

β_{mg} Range	Godunov Calculation Technique
$\beta_{mg} > \alpha_{1g}$	Second order
$\alpha_{1g} > \beta_{mg} > \alpha_{2g}$	$\zeta_g \times (\text{second order}) + (1 - \zeta_g) \times (\text{first order})$
$\alpha_{2g} > \beta_{mg}$	First order

ζ_g is equal to $(\beta_{mg} - \alpha_{2g}) / (\alpha_{1g} - \alpha_{2g})$. Most of our results have been obtained with $\alpha_{1g} = 0.7$ and $\alpha_{2g} = 1.4$. These values are such that the second order Godunov technique is only used at a small percentage of the cell boundaries, in the neighborhood of strong wave systems. This is desirable, since the second order Godunov procedure is more expensive computationally than the first order. The smooth blending between first and second order Godunov procedures was found to be necessary to obtain the best quality solutions. An abrupt switch between these two procedures had a tendency to produce oscillations in the solutions. At this point it is well to point out that no added artificial smoothing or damping was used in the codes.

5. EQUATIONS OF STATE

The EOS options currently available in the codes are (a) perfect gas, both volumetrically and calorically; (b) perfect gas volumetrically with $e = \int C_v dT$ taken from the JANAF tables (Reference C-1); (c) Zel'dovich and Raizer's three term EOS (Reference C-2) with the third term neglected; (d) an EOS for gases of the form $p(v-b) = RT$ where the "molecular volume" is taken to be compressible in accord with Zel'dovich and Raizer's cold compression $p-v$ expression (Reference C-2) and (e) the SESAME EOS data

(Reference C-3) from the Los Alamos Scientific Laboratory. (The latter data is in the tabular form $p = p(\rho, e)$, $T = T(\rho, e)$). In the above discussion, C_v denotes specific heat at constant volume, T , temperature, v , volume, b , molecular volume and R , the gas constant of the gas.

6. BOUNDARY CONDITIONS

Consider a one or two-dimensional solution geometry which is multi-zoned in the up-and-down (y or radial) direction. The two-dimensional geometries may be either planar or axisymmetric. For the two-dimensional geometries, we consider the flow to be entering on the left side and leaving on the right side. One of the following boundary conditions is imposed at each zone boundary (excluding the in- and outflow boundaries for the two-dimensional cases).

- (a) Normal velocity specified (e.g., zero normal velocity at a stationary boundary).
- (b) Pressure specified (e.g., zero pressure at a free surface).
- (c) Normal velocity and pressure matched across zone boundary (e.g., at a media interface).

To obtain values for the primitive variables at the zone boundaries (to be used as input in Godunov procedures), extrapolations and limiting procedures are used which are very similar to those used for the cell boundary calculations. There are some differences, however, because of the unavailability of certain cell center data on the "far" side of the zone boundary in question. With the primitive variables extrapolated to the zone boundary, first and second order Godunov procedures are used to find whichever (or both) of the variables, pressure and normal velocity, is required at the zone boundary.

For internal cell boundaries one cell removed from zone boundaries, excluding left and right side inflow and outflow zone boundaries, two additional "virtual" cells are created by "reflecting" the two cells nearest the zone boundary about the boundary. Using these "virtual" cells, extrapolations/interpolations in both directions can be made to obtain the primitive variables on the two sides of the cell boundary in question and then the

fluxes. Third order extrapolations/interpolations involving the "reflected" cells were found to produce erratic results, so second order extrapolations/interpolations were used instead.

For two-dimensional calculations, at the left side, where the flow enters, the flow is supersonic and the boundary conditions are held at prescribed values. At the right side, where the flow exits, the boundary condition values are set equal to those one cell upstream of the boundary. This is correct for supersonic exiting flow and is equivalent to non-reflecting boundary conditions (Reference C-4) for subsonic exiting flow.

7. ADVANCEMENT OF CODE IN TIME

The code employs an explicit MacCormack predictor-corrector differencing scheme (Reference C-5) which is second-order accurate in time. The solution to Equation (C-1) is advanced in time for the predictor and corrector steps as follows (including only the F flux for simplicity):

$$\overline{U^{n+1}V^{n+1}} = U^n V^n + \Sigma F_p A \Delta t \quad (C-12)$$

$$U^{n+1} V^{n+1} = \frac{1}{2} (U^n V^n + \overline{U^{n+1}V^{n+1}} + \Sigma F_c A \Delta t) \quad (C-13)$$

where U is the state vector, V is cell volume, A is the cell wall area, F_p and F_c are fluxes, Δt is the timestep and n , $\overline{n+1}$, $n+1$ denote conditions at the beginning of the timestep and at the end of the predictor and corrector timesteps, respectively. When the computational grid slides, $V^n \neq V^{\overline{n+1}} \neq V^{n+1}$ and the areas must be carefully averaged values. Otherwise, spurious source terms can be generated. If cell center e or ρ values calculated from Equations C-12 and C-13 are less than zero, they are reset to a fraction, typically 0.2, times the value at the beginning of the timestep. This safety device is invoked only very rarely, when very strong shock waves are present. Since the method is explicit, the von Neumann stability criterion that the CFL number be less than one must be applied. Most of our results were obtained with a CFL number of 0.6 (Reference C-6).

8. COMBUSTION MODELING

Gas combustion is modeled with a single global Arrhenius expression for reactants \rightarrow products. The products include all major mass fraction species with fixed mass fractions determined from separate equilibrium combustion calculations. The Arrhenius constants were determined for the hydrogen-oxygen combustion results presented here, by adjusting them to fit the experimental data of Reference C-7. To avoid non-physical propagation of detonation waves against a strong convection velocity across the grid structure, it is necessary to permit the consumption of 15%, at most, of the reactant mass originally present in a cell, per timestep. Each computational timestep consists of an Euler solver step with frozen chemistry, followed by a chemical reaction step in isolated cells without flow interaction. Each of these steps is second order accurate in time.

9. CONVERGENCE; CODE ACCELERATION TECHNIQUES

When steady-state solutions are sought, the convergence of the solution is judged using a density residue. This residue is a root mean square average, over all the computational cells, of the fractional density change per timestep. In typical converged solutions, this residue is 10^{-3} to 10^{-4} . Convergence is accelerated by as much as a factor of 2 or 3 by using two or three grids of successively finer mesh size. The solution is converged in the coarsest grid, which is then subdivided by a factor of 2 or 3 in each direction. Starting with coarse grid solution, a fine grid solution can then be converged relatively rapidly. This process may then be repeated.

REFERENCES

- C-1. D.R. Stull and M. Prophet, project directors, JANAF Thermochemical Tables, U.S. Government Printing Office, June 1971.
- C-2. Ya.B. Zel'dovich and Yu.P. Raizer, Physics of Shock Waves and High-Temperature Hydrodynamic Phenomena, Vol. II, Academic Press, New York, 1967, pp. 704-705 and p. 710.
- C-3. N.G. Cooper, ed., "An Invitation to Participate in the LASL Equation of State Library," Los Alamos Scientific Laboratory Report LASL-79-62, 1979.
- C-4. D.H. Rudy and J.C. Strikwerda, "A Nonreflecting Boundary Condition for Subsonic Navier-Stokes Calculations," Journal of Computational Physics, Vol. 36, No. 1, June 1980, pp. 55-70.
- C-5. R.W. MacCormack, "Current Status of Numerical Solutions of the Navier-Stokes Equations," Paper AIAA 85-0032, presented at the AIAA 23rd Aerospace Sciences Meeting, Reno, Nevada, January 14 - 17, 1985, p. 4.
- C-6. D.A. Anderson, J.C. Tannehill, and R.H. Pletcher, Computational Fluid Mechanics and Heat Transfer, McGraw-Hill, New York, 1984, p. 482-484.

BIBLIOGRAPHY

Bogdanoff, D.W. and Brackett, D.C., "A Computational Fluid Dynamics Code for the Investigation of Ramjet-in-Tube Concepts," AIAA Paper No. 87-1978, AIAA/SAE/ASME/ASEE 23rd Joint Propulsion Conference, San Diego, June 29 - July 2, 1987.

Brackett, D.C. and Bogdanoff, D.W., "Computational Investigation of Oblique Detonation Ramjet-in-Tube Concepts," accepted for publication in J. Propulsion & Power.

Bruckner, A.P., Bogdanoff, D.W., Knowlen, C., and Hertzberg, A., "Investigation of Gasdynamic Phenomena Associated with the Ram Accelerator Concept," AIAA Paper 87-1327, AIAA 19th Fluid Dynamics, Plasma Dynamics and Lasers Conference, Honolulu, Hawaii, June 8 - 10, 1987.

Bruckner, A.P. and Hertzberg, A., "Development of the Ram Accelerator Hyper-Velocity Launcher," 38th Meeting of the Aeroballistic Range Association, Tokyo, Japan, October 6 - 9, 1987.

Bruckner, A.P. and Hertzberg, A., "Ram Accelerator Direct Launch System for Space Cargo," Paper No. IAF-87-211, 38th Congress of the International Astronautical Federation, Brighton, England, October 10 - 17, 1987.

Bruckner, A.P., Knowlen, C., Scott, K.A., and Hertzberg, A., "High Velocity Modes of the Thermally Choked Ram Accelerator," AIAA Paper No. 88-2925, AIAA/ASME/SAE/ASEE 24th Joint Propulsion Conference, Boston, Massachusetts, July 11 - 14, 1988.

Bruckner, A.P., Knowlen, C., Bogdanoff, D.W., Hertzberg, A., and Scott, K.A., "Operational Characteristics of the Thermally Choked Ram Accelerator," accepted for publication in J. Propulsion & Power.

Hertzberg, A., Bruckner, A.P., and Bogdanoff, D.W., "The Ram Accelerator: A New Chemical Method of Achieving Ultrahigh Velocities," 37th Meeting of the Aeroballistic Range Association, Quebec, Canada, September 9 - 12, 1986.

BIBLIOGRAPHY (CONCLUDED)

Hertzberg, A., Bruckner, A.P., Bogdanoff, D.W., and Knowlen, C., "The Ram Accelerator and Its Applications: A New Chemical Approach for Reaching Ultrahigh Velocities," Invited Paper, Proceedings of the 16th International Symposium on Shock Tubes and Waves, Aachen, West Germany, July 26 - 30, 1987, pp. 117-128.

Hertzberg, A., Bruckner, A.P., and Bogdanoff, D.W., "Ram Accelerator: A New Chemical Method for Accelerating Projectiles to Ultrahigh Velocities," AIAA Journal 26, 1988, pp. 195-203.

Kaloupis, P., and Bruckner, A.P., "The Ram Accelerator: A Chemically Driven Mass Launcher," AIAA Paper No. 88-2968, AIAA/ASME/SAE/ASEE 24th Joint Propulsion Conference, Boston, Massachusetts, July 11 - 14, 1988.

Knowlen, C., Bruckner, A.P., Bogdanoff, D.W., and Hertzberg, A., "Performance Capabilities of the Ram Accelerator," AIAA Paper 87-2152, AIAA/SAE/ASME/ASEE 23rd Joint Propulsion Conference, San Diego, California, June 29 - July 2, 1987.